NONLINEAR ANALYSIS OF A LAMINATED GLASS PLATE WITH MIXED BOUNDARY CONDITIONS USING THE FINITE DIFFERENCE METHOD

A THESIS SUBMITTED TO
THE GRADUATE SCHOOL OF NATURAL AND APPLIED SCIENCES
OF
MIDDLE EAST TECHNICAL UNIVERSITY

BY

DENİZ CAN ELÇİ

IN PARTIAL FULFILLMENT OF THE REQUIREMENTS
FOR
THE DEGREE OF MASTER OF SCIENCE
IN
ENGINEERING SCIENCES

AUGUST 2025

Approval of the thesis:

NONLINEAR ANALYSIS OF A LAMINATED GLASS PLATE WITH MIXED BOUNDARY CONDITIONS USING THE FINITE DIFFERENCE METHOD

submitted by **DENIZ CAN ELCI** in partial fulfillment of the requirements for the degree of **Master of Science in Engineering Sciences, Middle East Technical University** by,

Prof. Dr. Naci Emre Altun
Dean, Graduate School of **Natural and Applied Sciences**

Prof. Dr. Murat Dicleli
Head of the Department, **Engineering Sciences**

Prof. Dr. Mehmet Zülfü Aşık
Supervisor, **Engineering Sciences, METU**

Prof. Dr. Ebru Dural
Co-supervisor, **Civil Engineering, Adnan Menderes University**

Examining Committee Members:

Prof. Dr. Işık Hakan Tarman (Head of Examining Committee)
Mechanical Engineering, METU

Prof. Dr. Mehmet Zülfü Aşık
Engineering Sciences, METU

Prof. Dr. Utku Kânoğlu
Aerospace Engineering, Dokuz Eylül University

Date: 12.08.2025

I hereby declare that all information in this document has been obtained and presented in accordance with academic rules and ethical conduct. I also declare that, as required by these rules and conduct, I have fully cited and referenced all material and results that are not original to this work.

Name Last name: Deniz Can Elçi

Signature:

ABSTRACT

NONLINEAR ANALYSIS OF A LAMINATED GLASS PLATE WITH MIXED BOUNDARY CONDITIONS USING THE FINITE DIFFERENCE METHOD

Elçi, Deniz Can
Master of Science, Engineering Sciences
Supervisor: Prof. Dr. Mehmet Zülfü Aşık
Co-Supervisor: Prof. Dr. Ebru Dural

August 2025, 123 pages

The Finite Difference Method (FDM) is widely used to solve partial differential equations in various physical problems, including solid mechanics. In the analysis of laminated composite structures, FDM enables meshless solutions. Laminated glasses can be mathematically modeled as alternating layers of two hard materials with soft interlayers. Previous studies have primarily focused on laminated glasses with symmetric boundary conditions. In this study, the solution method is extended to address unsymmetrical mixed boundary conditions, and the results are validated by comparison with finite element method (FEM) simulations.

Keywords: Non-linear Analysis, Solid Mechanics, Laminated Glass Plate, Finite Difference Method, Computational Mechanics

ÖZ

KARIŞIK SINIR KOŞULLARINA SAHIP LAMINE CAM PLAKANIN SONLU FARKLAR YÖNTEMİ İLE DOĞRUSAL OLMAYAN ANALİZİ

Elçi, Deniz Can
Yüksek Lisans, Mühendislik Bilimleri
Tez Yöneticisi: Prof. Dr. Mehmet Zülfü Aşık
Ortak Tez Yöneticisi:Prof. . Dr. Ebru Dural

Ağustos 2025, 123 sayfa

Sonlu Farklar Yöntemi (FDM), kısmi diferansiyel denklemlerin çeşitli fiziksel problemlerde çözümünde yaygın olarak kullanılmaktadır; bunlar arasında katı mekaniği de yer almaktadır. Lamineli kompozit yapıların analizinde FDM, ağsız (meshless) çözümler elde edilmesine olanak sağlar. Lamineli camlar, iki sert malzeme ile aradaki yumuşak katmanlar şeklinde matematiksel olarak modellenebilir. Önceki çalışmalar, öncelikle simetrik sınır koşullarına sahip lamineli camları incelemiştir. Bu çalışmada, çözüm yöntemi, simetrik olmayan karışık sınır koşullarını ele alacak şekilde geliştirilmiş ve elde edilen sonuçlar Sonlu Elemanlar Yöntemi (FEM) simülasyonlarıyla karşılaştırılarak doğrulanmıştır.

Anahtar Kelimeler: Doğrusal Olmayan Analiz, Katı Mekaniği, Lamine Cam Plaka, Sonlu Farklar Yöntemi, Hesaplamalı Mekanik

Dedicated

to my mother,

my wife,

my family,

and to the future of humanity.

ACKNOWLEDGMENTS

I would like to express my deepest gratitude to my supervisor, Prof. Dr. Mehmet Zülfü Aşık, and my co-supervisor, Prof. Dr. Ebru Dural, for their continuous support and guidance throughout all stages of this thesis. I would also like to extend my sincere thanks to the members of my examining committee, Prof. Dr. Işık Hakan Tarman and Prof. Dr. Utku Kânoğlu, for their valuable feedback and encouragement.

TABLE OF CONTENTS

LIST OF TABLES

TABLES

LIST OF FIGURES

FIGURES

LIST OF ABBREVIATIONS

ABBREVIATIONS

mm: milimeter

kPa: Kilo Pascal

kN: Kilo Newton

FDM: Finite Difference Method

MPa: Mega Pascal

GPa: Giga Pascal

LCD: Liquid Crystal Display

S.S. / SS: Simply supported

LIST OF SYMBOLS

SYMBOLS

w	Lateral displacement in z direction
u	In-plane displacement in x direction.
v	In-plane displacement in y direction.
u_1, u1	The upper layer u displacement.
u_2, u2	The lower layer u displacement.
v_1, v1	The upper layer v displacement.
v_2, v2	The lower layer v displacement.
wo	Lateral displacement in z direction for previous load step

CHAPTER 1

INTRODUCTION

Laminated glass plates are increasingly used in critical applications across aerospace, automotive, architecture, and electronics — industries where structural integrity under varied boundary conditions is vital. To ensure the proposed model is relevant to such diverse applications, this thesis begins by detailing the industrial use cases and mechanical motivation. A laminated glass plate typically consists of two or more isotropic glass layers bonded with a soft, viscoelastic interlayer such as polyvinyl butyral (PVB). This interlayer has significantly lower stiffness than the glass layers, resulting in a composite system with mechanical properties that differ markedly from homogeneous materials.

In this study, a robust and efficient finite difference method (FDM) model is developed to simplify and generalize laminated glass analysis, incorporating non-symmetrical boundary conditions and implemented in Python to replace earlier Fortran-based codes. Since laminated glass is widely used in applications such as structural glazing, aircraft windows, automobile windshields, train windows, and electronic displays, a more accessible and versatile analysis approach can significantly support the development of these products.

This composite structure exhibits unique mechanical behavior due to the significant stiffness difference between the glass layers (Young's modulus ~68.95 GPa) and the much softer PVB interlayer (100-3000 kPa). The interlayer's low shear stiffness allows relative sliding between glass layers, introducing geometric nonlinearity that becomes particularly significant in slender plate configurations.

PVB has become the industry standard interlayer material due to its excellent optical clarity, strong adhesion properties, and ability to absorb energy during impact. In structural modeling, the interlayer's thickness is typically small compared to the plate's in-plane dimensions, and its contribution to strain energy is often considered to be dominated by shear deformation while normal strains are neglected

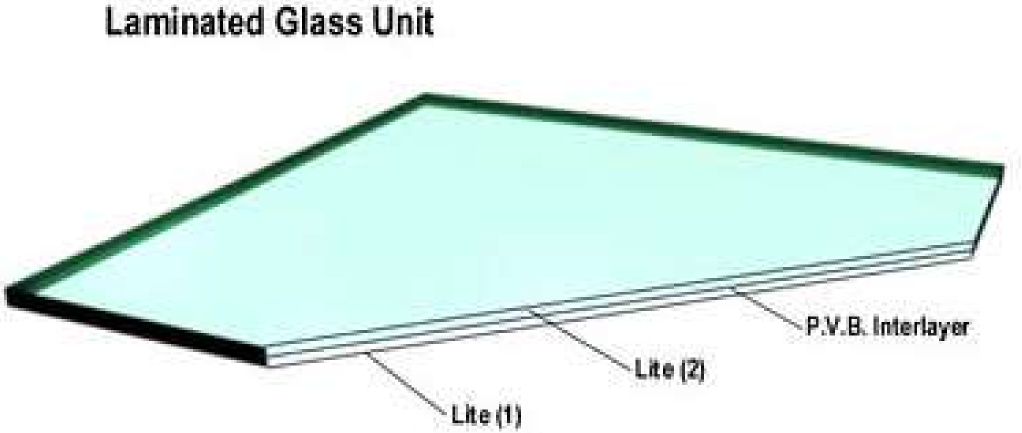

Figure 1.1 Schematic View of Laminated Glass Plate Components [1]

Laminated glass plates have higher safety than other glasses on fracture case. The interlayer holds the broken pieces of glass together and prevents harm to the environment. Due to this property, laminated glass parts are widely used in many areas. These areas include, but not limited to, aerospace, civil applications, trains, and so on. A two-ply laminated glass configuration is illustrated in Figure 1.1.

The two glasses can slide over each other due to lower stiffness of the PVB interlayer material. This attribute increases the nonlinear behavior along with the parts becoming slenderer. A photograph of a laminated glass can be observed in Figure 1.2.

Figure 1.2 Photograph of a Laminated Glass Plate [2]

Previous research has extensively applied the Finite Difference Method (FDM) to analyze laminated glass plates, but these studies have predominantly focused on symmetrical boundary conditions such as fully clamped or simply supported edges. Real-world applications, however, frequently involve asymmetrical or mixed boundary conditions where different edges may have varying support types or localized restraints. This thesis addresses this gap in the literature by investigating the mechanical response of laminated glass plates subjected to asymmetrical boundary conditions using FDM. The findings will contribute to more accurate numerical modeling of laminated glass structures in practical engineering scenarios where symmetrical boundary conditions cannot be assumed.

1.1 The Laminated Glass Part

The model considered in this study consists of a flat laminated plate composed of two glass layers with a soft adhesive interlayer in between. While the model can be extended to include additional layers, such configurations are beyond the scope of this thesis. The glass layers are made of standard float glass, a brittle material commonly used for its optical properties in everyday applications.

Annealed Glass
Breaks easily, producing long, sharp splinters

Tempered Glass
Shatters completely under higher levels of impact energy, and few pieces remain in the frame

Laminated Glass
May crack under pressure, but tends to remain integral, adhering to the plastic vinyl interlayer

Figure 1.3 The Comparison of Glass Types. [3]

Figure 1.3 illustrates three primary types of structural glass with distinct fracture characteristics. Annealed glass, the conventional float glass variety, poses significant safety concerns as it fractures into large, dangerous shards with sharp edges. In contrast, tempered glass undergoes specialized thermal processing that causes it to break into small, relatively harmless granular pieces when failed. The safest option, laminated glass, incorporates a durable interlayer that maintains glass cohesion even when fractured, preventing dangerous fragmentation while preserving structural integrity.

Figure 1.4 shows a side view of a two-layered laminated glass and the thickness symbols used in the analyses. The soft interlayer serves to prevent complete shattering in the event of fracture in one of the glass layers. If one layer fails, the other remains intact due to the presence of the interlayer. This layer is made of polyvinyl butyral (PVB), a material that also offers favorable optical properties, as typically required in laminated glass applications.

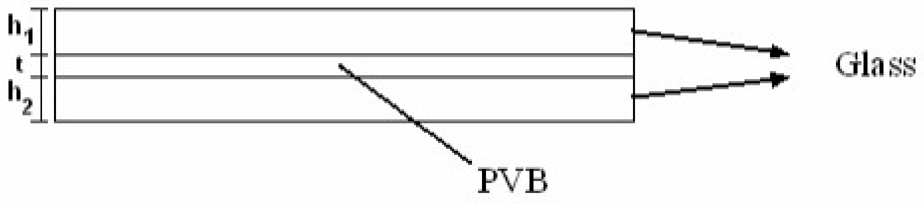

Figure 1.4 Thickness Convention and Material Layers in the Laminated Glass Diagram [4]

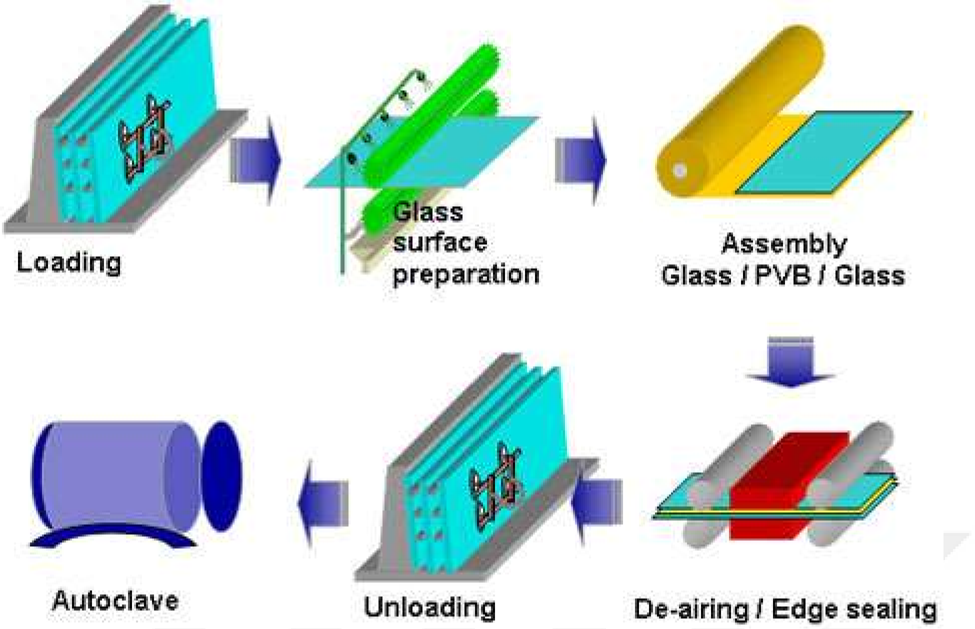

Figure 1.5 Fabrication Process of Laminated Glass Parts [1]

Figure 1.5 illustrates the principal steps involved in the production of two-layer laminated glass. The material properties are defined as input parameters within the model, allowing for adjustment to represent alternative glass types. By modifying these inputs, the model remains flexible and can be applied to a broader range of laminated glass configurations with varying material characteristics.

Given the slenderness of laminated plates and compliance of the interlayer, geometric nonlinearity is non-negligible — a fact handled by von Kármán-based modeling in this work.

1.2 Motivation and Applications

1.2.1 Aviation Glasses

Aircraft windshield design involves a range of stringent requirements, as the performance and safety of the structure depend heavily on the chosen glass material. The type of glass used varies significantly between light aircraft and high-speed aircraft, reflecting differences in operational conditions and safety standards. In particular, wind loads exerted during flight play a crucial role in determining the material selection and structural configuration of the windshield system. Figure 1.6, shows the cockpit windshield of a civil aircraft, which is constructed as laminated glazing.

Figure 1.6 Photograph of Aircraft Glass Window [5]

Aircraft cockpit windshields are generally constructed as laminated structures consisting of multiple glass plies bonded with polymer interlayers such as polyvinyl butyral (PVB) or polyurethane, with typical total thicknesses on the order of several millimeters to withstand bird strike and pressurization loads. The choice between flat or curved glass helps to reduce mounting strains that could potentially cause cracking. Additionally, this design allows for mechanical mounting, often featuring extended plastic edges with metal reinforcing strips. These extended edges enable screws to be securely fastened to the windshield frame, ensuring a positive mounting without inducing strain on the glass.

The mechanical analysis of the plate provides insight into how the plate deforms under varying boundary conditions, while also yielding its stress and strain distribution throughout the deformation process.

Laminated glass structures play a vital role in critical engineering applications where structural integrity under extreme conditions is essential. In aerospace, for instance, aircraft windshields are subjected to aerodynamic loads and potential high-velocity impacts such as bird strikes. The ability to accurately model deformation and stress in these components is crucial for ensuring safety and durability. Similarly, in defense and security applications, transparent armor systems demand advanced modeling of delamination behavior and energy absorption in polymer interlayers. The nonlinear numerical framework developed in this study addresses these needs by providing a reliable basis for virtual safety assessments and optimized laminated glass design, particularly under mixed and asymmetric boundary conditions commonly found in real-world scenarios.

1.2.2 Automobile and Train Glasses

Figure 1.7 Photograph of Rectangular and Curved Train Windows [7]

Laminated glass is widely used in the automotive industry, particularly for windshields, due to its superior safety and durability. Composed of two layers of glass bonded with a polyvinyl butyral (PVB) interlayer, it prevents the glass from shattering into sharp fragments upon impact, significantly reducing the risk of injury in accidents. This design is a critical safety feature in vehicles. In addition to its impact resistance, laminated glass offers excellent sound insulation, reducing road and wind noise for a quieter ride. It also blocks most of harmful UV rays, protecting passengers and preventing interior fading. Its strength makes it resilient against debris, rocks, and extreme weather, ensuring long-lasting performance and safety on the road. An example of a train window is shown in Figure 1.7.

1.2.3 LCD Glasses

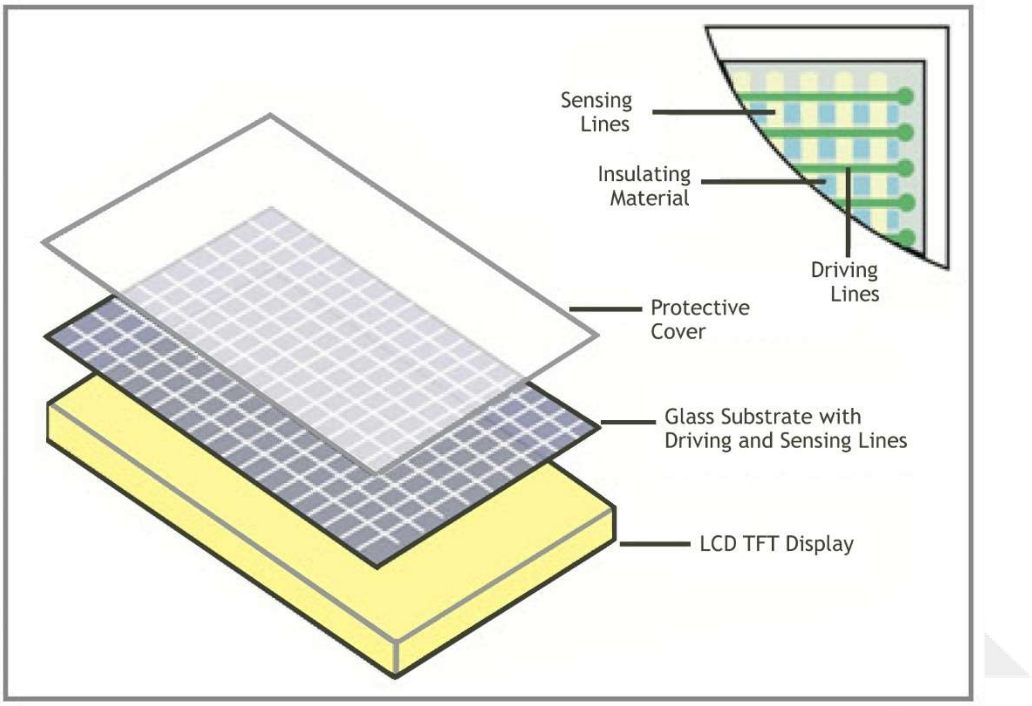

Figure 1.8 Drawing Showing Laminated Glass Plate Application in LCD [8].

LCD glass products are widely used in both private homes and offices. Electrically operated LCD specialist glass is a laminate that consists of at least two sheets of clear glass with an LCD film sandwiched between two or more plastic interlayers. This design combines the structural properties of laminated glass with the functionality of the LCD film, offering a versatile solution for various applications. An example of LCD glass is shown in Figure 1.8.

1.2.4 Solar Panel Glasses

Figure 1.9 Solar Panel Glass Structure [9]

Solar panels also feature a layered construction, with two thick outer layers—typically glass—that are significantly stiffer than the central interlayer, usually made of a thin and compliant material like ethylene-vinyl acetate (EVA). Figure 1.9 illustrates a solar panel glass. Solar panels, also known as photovoltaic (PV) panels, consist of multiple layers designed to efficiently convert sunlight into electricity. The front layer is made of tempered glass with an anti-reflective coating to maximize light absorption while protecting the panel from environmental factors like hail, dust, and UV radiation. Through this carefully engineered structure, solar panels harness sunlight to produce clean, renewable energy. Given the similarity in structure, the modeling approach developed in this study is well-suited for analyzing the mechanical behavior of solar panel glass, particularly in thin designs where the panel thickness is much smaller than its in-plane dimensions.

CHAPTER 2

LITERATURE REVIEW

2.1 Introduction to Energy Methods

Energy methods have revolutionized the analysis and design of physical systems by leveraging scalar energy quantities—such as potential, kinetic, and strain energy—to simplify complex problems in mechanics, thermodynamics, and materials science. Unlike traditional vector-based approaches, which rely on force and moment equilibria, energy methods provide a unified framework to derive governing equations, predict system behavior, and optimize performance through variational principles. Their inherent ability to bypass intricate force diagrams and boundary condition complexities has made them indispensable in modern engineering, particularly in fields like structural dynamics, renewable energy systems, and multi-physics simulations.

The theoretical foundations of energy methods trace back to the 18th and 19th centuries, with seminal contributions from Lagrange (Lagrangian mechanics), Hamilton (Hamilton's principle), and Rayleigh (Rayleigh's energy dissipation). These principles have since evolved into computational tools such as the finite difference method (FDM), finite element method (FEM), and dynamic system modeling techniques. However, contemporary challenges—such as modeling nonlinear material behavior, integrating dissipative forces into non-conservative systems, and optimizing sustainable energy infrastructure—demand extensions to classical energy formulations.

2.2 Plate Theories

Plate theory is an essential concept in structural mechanics that describes the behavior of thin, flat structural elements subjected to various loads. Plates are widely used in engineering applications such as aircraft wings, bridge decks, and building floors, where they function as primary load-bearing components. The theory provides mathematical models to analyze deformation, stress distribution, and structural stability under different boundary conditions and loading scenarios.

The formulation of plate bending problems originates from elasticity theory and is primarily governed by two major approaches: the Kirchhoff-Love theory for thin plates and the Mindlin-Reissner theory for moderately thick plates. The Kirchhoff-Love theory assumes that plane sections remain perpendicular to the mid-surface after deformation, making it suitable for thin plates where shear deformation is insignificant. On the other hand, the Mindlin-Reissner theory incorporates transverse shear effects, offering a more accurate representation for thicker plates.

Mathematically, plate bending is often modeled using the biharmonic equation, a fourth-order partial differential equation that links the transverse displacement of the plate to external loads and material properties. Due to the complexity of obtaining analytical solutions, numerical techniques such as the Finite Difference Method (FDM) are frequently employed to approximate solutions for practical engineering problems.

Boundary conditions play a crucial role in plate analysis, as they define how the edges of the plate are constrained. Common conditions include clamped, simply supported, and mixed boundary condition edges, each imposing different restrictions on displacement and rotation. Properly incorporating these constraints into numerical models is essential for accurately predicting the structural response of plates under real-world conditions.

Given the mathematical challenges involved in solving plate bending equations, numerical methods like FDM provide an efficient approach to obtaining approximate solutions. By discretizing the governing equations and applying suitable boundary conditions, FDM enables engineers to analyze plate behavior with precision, making it a valuable tool in computational structural mechanics.

2.2.1 Von Karman Plate Theory

The analysis of laminated glass plates subjected to various loading conditions often requires a theoretical framework that can accurately capture nonlinear effects, particularly when dealing with large deflections. One of the most widely used models in this regard is the von Kármán plate theory, which extends classical plate theory by incorporating geometric nonlinearity.

Von Kármán’s equations account for the coupling between in-plane and transverse displacements, making them particularly suitable for problems where deformations are significant but remain within the limits of moderate rotations. Unlike linear plate theories, which assume infinitesimal strains and small deflections, von Kármán’s formulation considers nonlinear strain-displacement relations while maintaining the assumptions of thin plate theory. This makes it applicable to a wide range of engineering problems, including laminated glass structures subjected to various boundary constraints.

In the context of the finite difference method (FDM), solving von Kármán’s nonlinear equations requires discretization techniques that effectively capture both in-plane membrane forces and out-of-plane bending effects. The complexity of these equations often necessitates iterative numerical schemes to achieve convergence, particularly when handling mixed boundary conditions. By employing FDM for this nonlinear analysis, it becomes possible to obtain an approximate yet sufficiently accurate representation of the structural response of laminated glass plates under complex loading scenarios.

This study utilizes von Kármán’s theory to model and analyze the nonlinear behavior of laminated glass plates with various boundary conditions. The goal is to gain insight into the influence of geometric nonlinearity on stress distributions and deformation patterns, contributing valuable knowledge to structural design and safety assessments in engineering applications. This is achieved by employing the assumptions in Section 3.2.1 and using the Von Karman plate theory strain definition in Equation (3.7).

This study employs von Kármán nonlinear strain theory without invoking the classical thin plate assumption. Since interlayer shear strains are explicitly accounted for, the assumption that plane sections remain perpendicular to the mid-surface does not hold. Therefore, the appropriate theoretical framework is more accurately described as the Nonlinear Mindlin-Reissner Plate Theory or First-Order Shear Deformation Theory (FSDT) with von Kármán-type geometric nonlinearity. A detailed discussion of the modeling assumptions and their implications is presented in Section 3.2.1 .

2.3 Finite Difference Method

As previously seen in works of Vallabhan and Aşık [10] [11], FDM has proven effective in laminated plate modeling. This section elaborates on the underlying formulation before its application to the current problem.

The Finite Difference Method (FDM) is a numerical approach used to approximate solutions to differential equations, making it a valuable tool in structural mechanics, fluid dynamics, and heat transfer. It works by discretizing a continuous domain into a grid and replacing derivatives with algebraic expressions to transform differential equations into solvable linear systems.

In structural elasticity problems, FDM is applied to equations like the Navier equations or the biharmonic equation, which describe the relationship between stress and strain in elastic structures. By substituting differential operators with finite difference approximations, these equations are converted into a system of algebraic equations that can be solved numerically.

The accuracy of the method depends on the type of finite difference approximations used, with common approaches including forward, backward, and central differences. Central difference schemes are generally preferred for their higher accuracy. Proper treatment of boundary conditions, such as Dirichlet, Neumann, or mixed conditions, is crucial in structural problems to ensure solution stability and correctness.

Compared to methods like the Finite Element Method (FEM) or the Finite Volume Method (FVM), FDM is easier to implement and computationally efficient on structured grids. However, it is less suited for complex geometries and irregular domains. Despite this, FDM remains a powerful technique for solving elasticity problems, especially when structured grids are applicable.

2.4 Previous Studies

Based on previous research, two categories can be formed regarding the strength and behavior of monolithic and laminated glass units: theoretical and experimental stress analysis, and failure testing. In 1910, Von Kármán developed the theory of nonlinear plate bending, which was further explored by Fung (1965) [12]. The nonlinear behavior of plates was examined by researchers such as Szilard (1974) [13], Timoshenko and Voinovsky (1965) [14], and others.

The applicability of von Kármán plate theory for large deformations in thin plates was rigorously established through analytical studies by Chia (1980) [15] and numerical validations by Reddy (2007) [16]. For laminated glass plates, early experimental work by Hooper (1973) [17] on laminated glass beams demonstrated the interlayer's shear-dependent coupling behavior, while Vallabhan (1983) [19] and Aşık (2003) [20] later developed analytical models capturing these effects. Vallabhan and his colleagues (Vallabhan et al., (1993) [10]; Vallabhan and Chou, (1986) [18]) developed pioneering analytical and numerical models for laminated glass plates subjected to uniform loads, treating the polyvinyl butyral (PVB) interlayer as a linear viscoelastic material capable of shear transfer. Their governing equations accounted for shear coupling between glass plies, demonstrating that the interlayer’s shear modulus significantly reduces plate deflection and peak stresses compared to monolithic glass. By solving these equations using finite difference methods (FDM) and validating results experimentally, they established a framework for optimizing laminated glass design under static and dynamic loads. Their work remains influential in standards for architectural glazing.

Several researchers have developed analytical models for laminated glass plates, treating the PVB interlayer as an elastic core that transfers shear between glass layers (Galuppi and Royer-Carfagni, 2012 [21]; Vallabhan, Aşık et al. [10]). Their work derived closed-form solutions for deflection and stress, highlighting the interlayer's role in enhancing stiffness and reducing peak stresses compared to monolithic glass. Other studies have investigated temperature and load-rate effects on PVB behavior, providing key insights into viscoelastic effects in laminated glass (Knight et al., 2024 [22]; Förch, 2020 [23]).

Aşık ((1993) [10], (1997) [11] and (2005) [24]) developed analytical and finite element models for laminated glass plates, focusing on the nonlinear behavior of PVB interlayers under large deformations. His work emphasized the hyperelastic and viscoelastic properties of interlayers, providing refined stress-strain relationships for laminated glass under static and dynamic loads. Aşık also proposed simplified design methods for engineers, bridging theoretical models with practical applications (Aşık, (2003) [20]). His contributions advanced the understanding of energy absorption and failure mechanisms in laminated glass structures.

Dural's recent research [25] [26], (2022-2023) focuses on the delamination behavior and nonlinear response of laminated glass structures, combining advanced computational modeling with experimental validation. In those studies [25] [26], she developed mathematical models for laminated glass beams and plates with initial delamination, incorporating nonlinear field equations and iterative solution procedures to analyze the effects of boundary conditions, delamination size, and location on structural performance. Her work demonstrated that PVB interlayer properties and geometric nonlinearity significantly influence stress distribution and deflection patterns for beams and plates, with findings validated through finite element analysis (FEA) and laboratory tests. Dural also compared the delamination resistance of laminated glass plates with different interlayers (PVB, EVA, and SentryGlas Plus), highlighting how interlayer type affects adhesion strength and failure thresholds under uniform pressure loads [27] [28].

Her studies further optimized multi-layer laminated glass configurations for blast-resistant applications, emphasizing the role of interlayer thickness and boundary conditions in enhancing safety for aerospace and architectural uses [28] [29] [30] . These contributions provide critical insights for designing laminated glass in safety-critical environments, bridging gaps between theoretical models and practical engineering solutions

2.5 Scope of This Study

Previous studies on this subject typically assumed symmetric boundary conditions along the plate edges and, consequently, employed symmetric stiffness matrices. These assumptions allowed the analysis to be restricted to a single quadrant of the plate, thereby reducing computational complexity through symmetry exploitation. In contrast, the present study introduces a new solution algorithm that models the entire plate domain without relying on symmetry assumptions. This full-domain approach enables the investigation of more general and realistic boundary conditions, including asymmetric and mixed types, thereby enhancing the applicability and robustness of the analysis.

To achieve this, a new model for the unsymmetrical and mixed boundary conditions is aimed to be derived, using energy methods and variational techniques. After the model equations are obtained, the model is transferred to script codes and input /output files are determined. The results from the output of the code have been taken and plots are needed to summarize the results.
Additionally, numerical experiments are conducted to investigate the influence of various parameters, including mesh discretization density, incremental load steps, and different thickness configurations for both glass and interlayer materials. The accuracy and reliability of the developed model will be validated through comparison with a Finite Element Model (FEM) implemented in Abaqus software.

CHAPTER 3

MODEL

3.1 Geometric Nonlinearity

In laminated glass structures, the combined effects of plate geometry and interlayer mechanical response introduce significant nonlinearities that must be considered in the analysis. To accurately capture these behaviors, the solution formulation incorporates geometric nonlinearity by employing nonlinear strain-displacement relationships within the energy-based framework of the model. This allows the simulation to account for large deformations and the coupling between in-plane and transverse responses, which are especially prominent in thin, layered systems under substantial loading.

When the plate displacements become comparable to its thickness, the assumption of linear midplane strains no longer holds. Instead, nonlinear strain terms emerge, resulting in significant coupling between bending and membrane (in-plane) effects. This coupling becomes critical in predicting accurate deformation patterns and internal stresses, particularly in laminated configurations. Moreover, the choice of boundary conditions—whether the plate edges are constrained or allowed to undergo in-plane displacements—has a profound influence on both the magnitude and distribution of deflections and stresses.

A key consequence of geometric nonlinearity is the emergence of tensile stresses along the deformed midplane, which act to counterbalance the applied transverse loads. This phenomenon—commonly referred to as membrane action—supplements the plate’s flexural rigidity and contributes to an overall increase in load-carrying capacity. In cases involving very thin plates or large deflections, the structural response may shift predominantly to in-plane stretching, causing the plate to behave more like a membrane than a bending-dominated structure.

3.2 Analytical Model

The finite difference model developed in this study involves five unknown field variables. The in-plane displacements are denoted as u1, v1, u2, and v2, where u1 and v1 correspond to the upper glass layer, and u2 and v2 correspond to the bottom glass layer. The symbols for the displacements are given in Table 3.1. The transverse (out-of-plane) displacement is represented by w and is assumed to remain constant through the plate's thickness. This assumption is based on the neglect of transverse normal stresses and strains, meaning that through-thickness compression and tension are considered negligible in the present formulation. A schematic of the model is presented in Figure 3.1.

Table 3.1 The symbols for displacements.

	Layer 1	Layer 2
Displacement in x-direction	u_1	u_2
Displacement in y-direction	v_1	v_2
Displacement in z-direction*	w	w

* The assumptions in section 3.2.1, numbers 4 and 5.

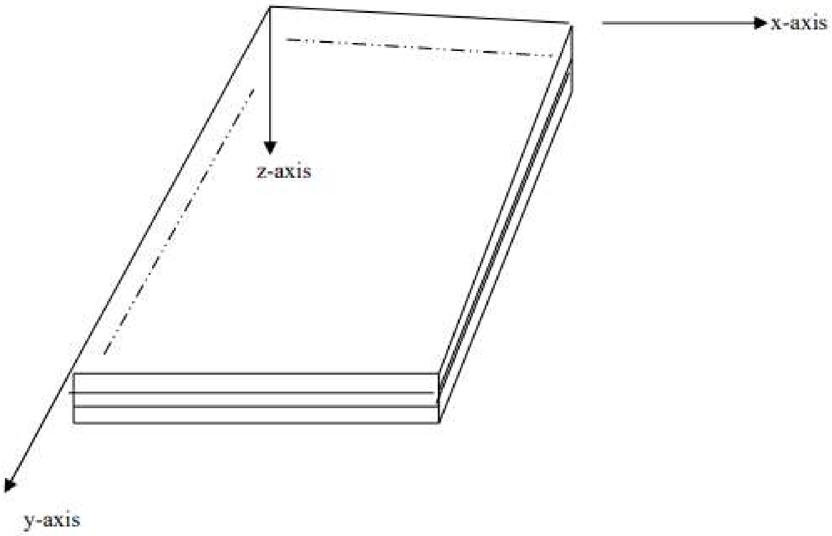

Figure 3.1 Sketch of Analysis Model

3.2.1 Assumptions Used in the Model

The assumptions underpinning the analytical formulation are outlined below:

1- Linear Elastic Behavior: All materials in the model are assumed to behave elastically according to Hooke's Law:

$$\sigma = E * \varepsilon \tag{3.1}$$

2- Material Properties: The glass panels and the interlayer are each considered isotropic and homogeneous.

3- Thin Plate Assumption: The structure is modeled as a thin plate since its width-to-thickness ratios (a/t and b/t) exceed 10, consistent with criteria from Ventsel and Krauthammer (2001) [31].

4- Neglect of Transverse Normal Stresses and Strains: As is standard for thin plates, transverse normal stress and strain are assumed negligible [32]:

$$\sigma_z = e_z \approx 0 \tag{3.2}$$

5- No Interfacial Separation: There is no relative displacement between the contact surfaces of the glass layers and the interlayer. Hence, vertical displacements are continuous across the interface:

$$w_1 = w_2 \tag{3.3}$$

6- Unified Transverse Displacement: The lateral (z-direction) displacement of the upper and lower glass layers is assumed to be the same. This is justified by the very small thickness of the interlayer (typically PVB), which undergoes negligible compression compared to the deflection of the glass layers.

7- Negligible Through-Thickness Normal Strain Energy: Based on Assumption 6, the contribution of normal strain energy in the z-direction is neglected for both the glass and interlayer components.

8- Kirchhoff Hypothesis (straight normals): The normal lines to the mid-surface of each glass plate remain straight and perpendicular to the mid-surface during deformation.

9- Interlayer Carries Only In-Plane Shear: The interlayer is assumed to resist only in-plane shear stresses, not normal or bending stresses.

3.2.2 Formulation and Derivation of Equations

The derivation begins by expressing the total potential energy V of the laminated plate as the sum of the internal strain energies stored in the glass layers and the interlayer, along with the potential energy due to external loads. The expression is written as:

$$V = \overline{U}_m^{(1)} + \overline{U}_b^{(1)} + \overline{U}_m^{(2)} + \overline{U}_b^{(2)} + \overline{U}_{xz}^{(I)} + \overline{U}_{yz}^{(I)} + \overline{\Omega} \tag{3.4}$$

Table 3.2 Strain energy terms symbols and potential energy for external work symbol

$\overline{U}_m^{(i)}$	Membrane strain energy for layer (i); i=1,2 for the top and bottom layers
$\overline{U}_b^{(i)}$	Bending strain energy for layer (i)
$\overline{U}_{xz}^{(I)}, \overline{U}_{yz}^{(I)}$	Integrated shear strain energy of the interlayer shear strains $\gamma_{xz}\ andand\ \gamma_{yz}$.
$\overline{\Omega}$	Potential energy for the external loads.

Table 3.2 explains the strain energy terms in Equation (3.4). The geometrical and material parameters used in this study are defined as follows: The dimensions of the plate are denoted by a and b, representing its lengths in the x- and y-directions, respectively. The thickness of each layer "i" is indicated by "h_i". The material properties of the glass are characterized by the elastic modulus E and Poisson's ratio μ.

The bending strain energy formula (Langhaar (1962) [33]) is given as:

$$\overline{U}_b^{(i)} = \int_{-b}^{b}\int_{-a}^{a} U_b^{(i)} dx\,dy$$
$$= \int_{-b}^{b}\int_{-a}^{a} \frac{E * h_i^3}{24(1-\mu^2)}\left[\left(\frac{\partial^2 w}{\partial x^2}\right)^2 + \left(\frac{\partial^2 w}{\partial y^2}\right)^2 + 2\mu\left(\frac{\partial^2 w}{\partial x^2}\right)\left(\frac{\partial^2 w}{\partial y^2}\right)\right.$$
$$\left. + 2(1-\mu)\left(\frac{\partial^2 w}{\partial x \partial y}\right)^2\right] dx\,dy$$

(3.5)

The membrane strain energy function, Langhaar (1962) [33], can be expressed as;

$$\overline{U}_m^{(i)} = \int_{-b}^{b}\int_{-a}^{a} U_m^{(i)} dx\,dy$$
$$= \int_{-b}^{b}\int_{-a}^{a} \frac{E * h_i}{2(1-\mu^2)}\left[{e_{ix}}^2 + {e_{iy}}^2 + 2\mu e_{ix} e_{iy} + \frac{1}{2}(1\right.$$
$$\left. - \mu){e_{ixy}}^2\right] dx\,dy$$

(3.6)

Large strains invalidate the commonly used "infinitesimal strain" assumption, necessitating the use of Green-Lagrange strains instead. In geometric nonlinear problems, where large deformations occur, these strain equations become essential for accurately capturing the system’s response. The Green-Lagrange strain formulation accounts for significant displacement gradients and rotational effects, providing a more accurate representation of material behavior under large strains.

Below is the general description of Green-Lagrange strains (in Einstein’s notation):

$$E_{ij} = \frac{1}{2}\left(\frac{\partial u_i}{\partial x_j} + \frac{\partial u_j}{\partial x_i} + \frac{\partial u_k}{\partial x_i}\frac{\partial u_k}{\partial x_i}\right)$$

(3.7)

The nonlinear strains used in this problem are derived from Green-Lagrange strains and given as follows:

$$e_{ix} = \frac{\partial u_i}{\partial x} + \frac{1}{2}\left(\frac{\partial w}{\partial x}\right)^2 \tag{3.8}$$

$$e_{iy} = \frac{\partial v_i}{\partial y} + \frac{1}{2}\left(\frac{\partial w}{\partial y}\right)^2 \tag{3.9}$$

$$e_{ixy} = \frac{\partial u_i}{\partial y} + \frac{\partial v_i}{\partial x} + \left(\frac{\partial w}{\partial x}\right)\left(\frac{\partial w}{\partial y}\right) \tag{3.10}$$

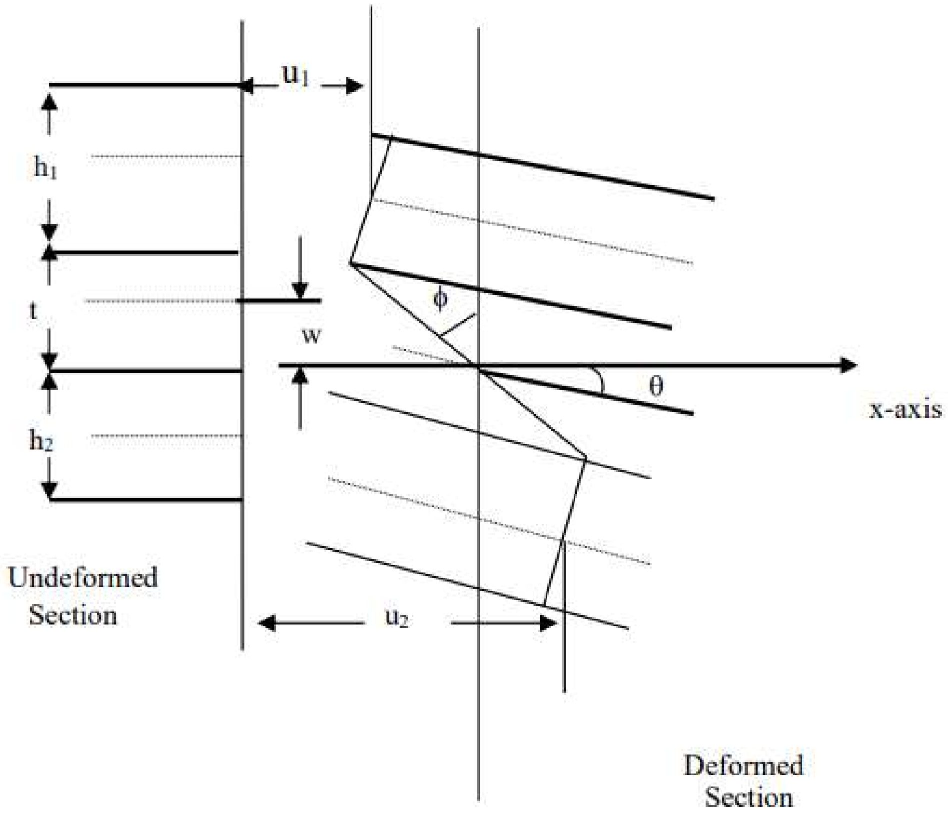

Figure 3.2 Deformation of Laminated Glass in the Thickness Cross Section

In Figure 3.2, θ_x is the overall slope of the laminate with respect to its centerline, such that

$$\theta_x = -\frac{\partial w}{\partial x} \tag{3.11}$$

ϕ_x is the deformation slope of the interlayer, describing the slope along the x-direction.

$$\phi_x = \frac{\partial u}{\partial z} \tag{3.12}$$

Using those slopes (ϕ_x, θ_x), the average transverse shear strains, γ_{xz} and γ_{yz}., are given as below:

$$\gamma_{xz} = \phi_x + \theta_x = -\frac{\partial w}{\partial x} + \frac{\partial u}{\partial z} = -\frac{\partial w}{\partial x} + \frac{\left[u_1 - u_2 - \frac{\partial w}{\partial x}\left(\frac{h_1}{2} + \frac{h_2}{2}\right)\right]}{t}$$
$$= \frac{\left[u_1 - u_2 - \frac{\partial w}{\partial x}\left(\frac{h_1}{2} + \frac{h_2}{2} + t\right)\right]}{t} \tag{3.13}$$

$$\gamma_{yz} = \phi_y + \theta_y = -\frac{\partial w}{\partial y} + \frac{\partial v}{\partial z} = -\frac{\partial w}{\partial y} + \frac{\left[v_1 - v_2 - \frac{\partial w}{\partial y}\left(\frac{h_1}{2} + \frac{h_2}{2}\right)\right]}{t}$$
$$= \frac{\left[v_1 - v_2 - \frac{\partial w}{\partial y}\left(\frac{h_1}{2} + \frac{h_2}{2} + t\right)\right]}{t} \tag{3.14}$$

The integrated shear strain energies across the plate are obtained by integrating the shear strain energy density over the two dimensions of the plate, as shown below:

$$\begin{aligned}\overline{U}_{xz}^{(I)} &= \int_{-b}^{b}\int_{-a}^{a} U_{xz}^{(I)} dx\, dy \\ &= \int_{0}^{t}\int_{-b}^{b}\int_{-a}^{a} \frac{1}{2} G_I\, \gamma_{xz}^2\, dV \\ &= \int_{-b}^{b}\int_{-a}^{a} \frac{G_I}{2t}\left[(u_1 - u_2) - \frac{\partial w}{\partial x}\left(\frac{h_1}{2} + \frac{h_2}{2} + t\right)\right]^2 dx\, dy\end{aligned}$$

(3.15)

$$\begin{aligned}\overline{U}_{yz}^{(I)} &= \int_{-b}^{b}\int_{-a}^{a} U_{yz}^{(I)} dx\, dy \\ &= \int_{0}^{t}\int_{-b}^{b}\int_{-a}^{a} \frac{1}{2} G_I\, \gamma_{yz}^2\, dV \\ &= \int_{-b}^{b}\int_{-a}^{a} \frac{G_I}{2t}\left[(v_1 - v_2) - \frac{\partial w}{\partial y}\left(\frac{h_1}{2} + \frac{h_2}{2} + t\right)\right]^2 dx\, dy\end{aligned}$$

(3.16)

In Equation (3.17), the force potential (external work) is expressed for the entire plate. The loading is a uniformly distributed pressure applied to the top face of the laminate.

$$\overline{\Omega} = \int_{-b/2}^{b/2}\int_{-a/2}^{a/2} \Omega \, dx\, dy = \int_{-b}^{b}\int_{-a}^{a} -\mathrm{qw}\, dx\, dy$$

(3.17)

$$\begin{aligned} V = & \int_{-b}^{b}\int_{-a}^{a}\left[U_m^{(1)} + U_b^{(1)} + U_m^{(2)} + U_b^{(2)} + \overline{U}_{xz}^{(I)} + \overline{U}_{yz}^{(I)} + \Omega\right] dx\, dy \\ & = \int_{-b}^{b}\int_{-a}^{a} F\, dx\, dy \end{aligned}$$

(3.18)

$$\begin{aligned} F = & \frac{E\, h_1}{2\,(1-\mu^2)}\left[{e_{1x}}^2 + {e_{1y}}^2 + 2\mu e_{1x} e_{1y} + \frac{1}{2}(1-\mu){e_{1xy}}^2\right] \\ & + \frac{E\, h_2}{2\,(1-\mu^2)}\left[{e_{2x}}^2 + {e_{2y}}^2 + 2\mu e_{2x} e_{2y} + \frac{1}{2}(1-\mu){e_{2xy}}^2\right] \\ & + \frac{E(h_1^3 + h_2^3)}{24(1-\mu^2)}\left[\left(\frac{\partial^2 w}{\partial x^2}\right)^2 + \left(\frac{\partial^2 w}{\partial y^2}\right)^2 + 2\mu\left(\frac{\partial^2 w}{\partial x^2}\right)\left(\frac{\partial^2 w}{\partial y^2}\right)\right. \\ & \left. + 2(1-\mu)\left(\frac{\partial^2 w}{\partial x \partial y}\right)^2\right] + \frac{G_I}{2t}\left[u_1 - u_2 - \frac{\partial w}{\partial x}\left(\frac{h_1}{2} + \frac{h_2}{2} + t\right)\right]^2 \\ & + \frac{G_I}{2t}\left[v_1 - v_2 - \frac{\partial w}{\partial y}\left(\frac{h_1}{2} + \frac{h_2}{2} + t\right)\right]^2 - q * w \end{aligned}$$

(3.19)

By applying a variational approach to the total potential energy, the following Euler Equation, Equation (3.20) is derived. The Euler equation for the system is presented in Langhaar (1962, p. 96) [33] similarly.

$$\frac{\partial F}{\partial u_i}-\frac{\partial}{\partial x}\left(\frac{\partial F}{\partial u_{i,x}}\right)-\frac{\partial}{\partial y}\left(\frac{\partial F}{\partial u_{i,y}}\right)+\frac{\partial^2}{\partial x^2}\left(\frac{\partial F}{\partial u_{i,xx}}\right)+\frac{\partial^2}{\partial x\partial y}\left(\frac{\partial F}{\partial u_{i,xy}}\right)+\frac{\partial^2}{\partial y^2}\left(\frac{\partial F}{\partial u_{i,yy}}\right)=0 \tag{3.20}$$

The Laplace Operator is given in Equation (3.21).

$$\nabla^2=\frac{\partial^2}{\partial x^2}+\frac{\partial^2}{\partial y^2} \tag{3.21}$$

The 4th order gradient operator is given in Equation (3.22

$$\nabla^4=\frac{\partial^4}{\partial x^4}+2\frac{\partial^4}{\partial x^2\partial y^2}+\frac{\partial^4}{\partial y^4} \tag{3.22}$$

The governing equations of the problem are derived by first substituting the expression for “F” from equation (3.19), into equation (3.20). Next, the required partial derivatives are taken as in equation (3.20) for each of the five independent displacement fields (w, u1, v1, u2, v2). This procedure results in five coupled nonlinear equations, which are presented in Equations (3.23) - (3.27).

$$
\begin{aligned}
&\left[(D_1 + D_2) * \nabla^4 - \frac{G_I}{t}\left(\frac{h_1}{2} + \frac{h_2}{2} + t\right)^2 * \nabla^2\right] w \\
&\qquad = q \\
&\qquad + \frac{Eh_1}{1-\mu^2}\left[\left(e_{1x} + \mu e_{1y}\right)\frac{\partial^2 w}{\partial x^2} + \left(e_{1y} + \mu e_{1x}\right)\frac{\partial^2 w}{\partial y^2} + (1 - \mu)e_{1xy}\frac{\partial^2 w}{\partial x \partial y}\right] \\
&\qquad + \frac{Eh_2}{1-\mu^2}\left[\left(e_{2x} + \mu e_{2y}\right)\frac{\partial^2 w}{\partial x^2} + \left(e_{2y} + \mu e_{2x}\right)\frac{\partial^2 w}{\partial y^2} + (1 - \mu)e_{2xy}\frac{\partial^2 w}{\partial x \partial y}\right] - \frac{G_I}{t}\left(\frac{h_1}{2} + \frac{h_2}{2} + t\right)\left(\frac{\partial u_1}{\partial x} - \frac{\partial u_2}{\partial x} + \frac{\partial v_1}{\partial y} - \frac{\partial v_2}{\partial y}\right)
\end{aligned}
\tag{3.23}
$$

$$
\begin{aligned}
&\left[\frac{\partial^2}{\partial x^2} + \frac{(1-\mu)}{2}\frac{\partial^2}{\partial y^2} - \frac{G_I(1-\mu)}{2Gh_1 t}\right] u_1 \\
&\qquad = -\left[\frac{1+\mu}{2}\frac{\partial^2}{\partial x \partial y}\right] v_1 - \left[\frac{G_I(1-\mu)}{2Gh_1}\right] u_2 - \frac{\partial w}{\partial x}\left[\frac{\partial^2 w}{\partial x^2} + \frac{(1-\mu)}{2}\frac{\partial^2 w}{\partial y^2}\right] \\
&\qquad - \frac{1+\mu}{2}\frac{\partial^2 w}{\partial x \partial y}\frac{\partial w}{\partial y} - \frac{G_I(1-\mu)}{2Gh_1 t}\left(\frac{h_1}{2} + \frac{h_2}{2} + t\right)\frac{\partial w}{\partial x}
\end{aligned}
\tag{3.24}
$$

$$\begin{aligned}\left[\frac{\partial^2}{\partial y^2}+\frac{(1-\mu)}{2}\frac{\partial^2}{\partial x^2}-\frac{G_I(1-\mu)}{2Gh_1t}\right]v_1 \\ =-\left[\frac{1+\mu}{2}\frac{\partial^2}{\partial x\partial y}\right]u_1-\left[\frac{G_I(1-\mu)}{2Gh_1t}\right]v_2-\frac{\partial w}{\partial y}\left[\frac{\partial^2 w}{\partial y^2}+\frac{(1-\mu)}{2}\frac{\partial^2 w}{\partial x^2}\right] \\ -\frac{1+\mu}{2}\frac{\partial^2 w}{\partial x\partial y}\frac{\partial w}{\partial x}-\frac{G_I(1-\mu)}{2Gh_1t}\left(\frac{h_1}{2}+\frac{h_2}{2}+t\right)\frac{\partial w}{\partial y}\end{aligned}$$

(3.25)

$$\begin{aligned}\left[\frac{\partial^2}{\partial x^2}+\frac{(1-\mu)}{2}\frac{\partial^2}{\partial y^2}-\frac{G_I(1-\mu)}{2Gh_2t}\right]u_2 \\ =-\left[\frac{1+\mu}{2}\frac{\partial^2}{\partial x\partial y}\right]v_2-\left[\frac{G_I(1-\mu)}{2Gh_2t}\right]u_1-\frac{\partial w}{\partial x}\left[\frac{\partial^2 w}{\partial x^2}+\frac{(1-\mu)}{2}\frac{\partial^2 w}{\partial y^2}\right] \\ -\frac{1+\mu}{2}\frac{\partial^2 w}{\partial x\partial y}\frac{\partial w}{\partial y}+\frac{G_I(1-\mu)}{2Gh_2t}\left(\frac{h_1}{2}+\frac{h_2}{2}+t\right)\frac{\partial w}{\partial x}\end{aligned}$$

(3.26)

$$\begin{aligned}\left[\frac{\partial^2}{\partial y^2}+\frac{(1-\mu)}{2}\frac{\partial^2}{\partial x^2}-\frac{G_I(1-\mu)}{2Gh_2t}\right]v_2 \\ =-\left[\frac{1+\mu}{2}\frac{\partial^2}{\partial x\partial y}\right]u_2-\left[\frac{G_I(1-\mu)}{2Gh_1t}\right]v_1-\frac{\partial w}{\partial y}\left[\frac{\partial^2 w}{\partial y^2}+\frac{(1-\mu)}{2}\frac{\partial^2 w}{\partial x^2}\right] \\ -\frac{1+\mu}{2}\frac{\partial^2 w}{\partial x\partial y}\frac{\partial w}{\partial x}-\frac{G_I(1-\mu)}{2Gh_2t}\left(\frac{h_1}{2}+\frac{h_2}{2}+t\right)\frac{\partial w}{\partial y}\end{aligned}$$

(3.27)

The flexural rigidity values for the upper and lower layers are given in Equations (3.28) and (3.29).

$$D_1 = \frac{E * h_1}{12 * (1 - \mu^2)}$$

(3.28)

$$D_2 = \frac{E * h_2}{12 * (1 - \mu^2)}$$

(3.29)

The shear modulus formula is given in Equation (3.30).

$$G = \frac{E}{2(1 + \mu)}$$

(3.30)

3.2.2.1 Boundary Conditions

For the plate; edge boundary conditions can be determined as any combination of clamped (fixed) and simply supported (hinged) boundary conditions, symmetrical or unsymmetrical. Both clamped and simply supported boundary conditions are Dirichlet type boundary conditions.

For simply supported (hinged) edges, rotation is permitted only about one axis, whereas both the transverse displacement and the rotation about the orthogonal axis are constrained. The corresponding boundary condition equations are summarized below.

For simply supported boundary conditions at x=0 or x=a (a: Plate width in x-direction);

$$e_{1y}+\mu e_{1x} = 0 \tag{3.31}$$

$$e_{1xy} = 0 \tag{3.32}$$

$$e_{2y}+\mu e_{2x} = 0 \tag{3.33}$$

$$e_{2xy} = 0 \tag{3.34}$$

$$w = 0 \tag{3.35}$$

$$\frac{\partial^2 w}{\partial x^2} = 0 \tag{3.36}$$

For simply supported edge boundary conditions at y=0 or y=b (b: Plate width in y-direction);

$$e_{1y}+\mu e_{1x} = 0 \tag{3.37}$$

$$e_{1xy} = 0 \tag{3.38}$$

$$e_{2y}+\mu e_{2x}=0$$

(3.39)

$$e_{2xy}=0$$

(3.40)

$$w=0$$

(3.41)

$$\frac{\partial^2 w}{\partial y^2}=0$$

(3.42)

For clamped (fixed) edges, all rotations and displacements along the edge are fully restrained. The associated boundary condition equations are summarized below.

For clamped edge boundary conditions at x=0 or x=a (a: Plate width in x-direction);

$$u=v=w=0$$

(3.43)

$$\frac{\partial w}{\partial x}=0$$

(3.44)

For clamped edge boundary conditions at y=0 or y=b (b: Plate width in x-direction);

$$u = v = w = 0 \tag{3.45}$$

$$\frac{\partial w}{\partial y} = 0 \tag{3.46}$$

3.3 Laminated Glass Specifications

The laminated glass material properties are given in section 1.1 (Also see Appendix 1).

A two layered laminated glass plate is taken for the analyses:

Glass elastic modulus usually changes between 60 - 80 GPa and in the analyses it’s taken as 70 GPa.

The PVB (polyvinyl butyral) interlayer typically exhibits a shear modulus in the range of 100 to 3000 kPa; a representative value of 1000 kPa was selected for the analyses conducted in this study.

Interlayer thicknesses are given as 0.76 millimeters for the analyses.

Glass layers thicknesses are taken as 5 millimeters.

The square plate has a width of 1 meter, making it 1 m x 1 m in plan view.

A uniform pressure load of 0.2 kPa is used in the analyses, except in cases where variable pressure loading is specifically considered.

3.4 Employment of Finite Difference Method

The Finite Difference Method (FDM), a widely used numerical technique, is employed to discretize the governing differential equations into algebraic form and to derive matrix representations for both lateral and in-plane displacements. Five solution matrices are constructed corresponding to the five displacement fields—w, u1, v1, u2, and v2. These matrices are inherently nonlinear and coupled, reflecting the effects of large deformations and the interaction between different displacement fields across the layered structure.

Unlike previous studies, this work models the full plate, allowing all edges to represent the actual physical boundary conditions of the problem. The five field equations are nonlinear with the function of the lateral displacement, w, even though all of the differential operators in u1, v1, u2, and v2 are linear. Nonlinearity of the problem necessitates the employment of an iterative numerical technique for the solution.

$$[A]\{w\} = \left\{q + \{f1(w, u_1, v_1, u_2, v_2)\}\right\} \tag{3.47}$$

where q is the lateral loading vector.

Equation (3.47) represents the lateral displacement (w) solution matrix system, where “f1” includes the nonlinear terms and thus it is grouped to the right-hand side.

$$
\begin{aligned}
Cw_{(i,j)} &+ Bw_{(i+1,j)} + Bw_{(i-1,j)} + Hw_{(i+2,j)} + Hw_{(i-2,j)} + Jw_{(i,j+1)} + Jw_{(i,j-1)} \\
&+ Gw_{(i,j+2)} + Gw_{(i,j-2)} + Fw_{(i+1,j+1)} + Fw_{(i+1,j-1)} + Fw_{(i-1,j+1)} \\
&+ Fw_{(i-1,j-1)} = \{RHS\}_{(i,j)}
\end{aligned}
\tag{3.48}
$$

In Equation (3.48), the discretized general form for the “w” solution is provided. The coefficients are labeled as C, B, H, F, J, and G for better readability.

$$
\begin{aligned}
\{RHS\}_{(i,j)} = \Bigg\{ q \\
&+ \frac{Eh_1}{2(1-\mu^2)}\left[\left(e_{1x}+e_{1y}\right)\frac{\partial^2 w}{\partial x^2} + \left(e_{1y}+e_{1x}\right)\frac{\partial^2 w}{\partial y^2}\right. \\
&\left. + (1-\mu)e_{1xy}\frac{\partial^2 w}{\partial x \partial y}\right] \\
&+ \frac{Eh_2}{2(1-\mu^2)}\left[\left(e_{2x}+e_{2y}\right)\frac{\partial^2 w}{\partial x^2} + \left(e_{2y}+e_{2x}\right)\frac{\partial^2 w}{\partial y^2}\right. \\
&\left. + (1-\mu)e_{2xy}\frac{\partial^2 w}{\partial x \partial y}\right] \\
&- \frac{G_I}{t}\left(\frac{h_1}{2}+\frac{h_2}{2}+t\right)\left(\frac{\partial u_1}{\partial x}-\frac{\partial u_2}{\partial x}+\frac{\partial v_1}{\partial y}-\frac{\partial v_2}{\partial y}\right)\Bigg\}_{(i,j)}
\end{aligned}
\tag{3.49}
$$

The right-hand side in Equation (3.48), is expanded in Equation (3.49) above. The nonlinear terms are grouped in this “RHS” term.

$$C = (D_1 + D_2)\left(\frac{6}{h_x^4} + \frac{6}{h_y^4} + \frac{8}{h_x^4}\right) + \frac{G_I}{t}\left(\frac{h_1}{2} + \frac{h_2}{2} + t\right)^2 \left(\frac{2}{h_x^2} + \frac{2}{h_y^2}\right) \tag{3.50}$$

$$B = (D_1 + D_2)\left(\frac{-4}{h_x^4} + \frac{-4}{h_x^2 h_y^2}\right) + \frac{G_I}{t}\left(\frac{h_1}{2} + \frac{h_2}{2} + t\right)^2 \left(\frac{-1}{h_x^2}\right) \tag{3.51}$$

$$H = (D_1 + D_2)\left(\frac{1}{h_x^4}\right) \tag{3.52}$$

$$F = (D_1 + D_2)\left(\frac{2}{h_x^2 h_y^2}\right) \tag{3.53}$$

$$J = (D_1 + D_2)\left(\frac{-4}{h_y^4} + \frac{-4}{h_x^2 h_y^2}\right) + \frac{G_I}{t}\left(\frac{h_1}{2} + \frac{h_2}{2} + t\right)^2 \left(\frac{-1}{h_y^2}\right) \tag{3.54}$$

$$G = (D_1 + D_2)\left(\frac{1}{h_y^4}\right) \tag{3.55}$$

The coefficients C, B, H, F, J, and G in Equation (3.48) are detailed in Equations (3.50) through (3.55). The Modified Strongly Implicit (MSI) method, originally developed by Schneider and Zedan (1981) [34], is employed to solve for the in-plane displacements u1, v1, u2, and v2. In this approach, only five difference-equation coefficients are stored, reducing both memory requirements and computational cost. These coefficients vary depending on the applied boundary conditions. Following a similar strategy to that used in Aşık's study (1997) [35], the coefficient structure is adopted to facilitate efficient in-plane displacement solutions.

$$Apu(i,j) * u_1(i,j) = Awu(i,j) * u_1(i-1,j) + Aeu(i,j) * u_1(i+1,j) + Asu(i,j) * u_1(i,j-1) + Anu(i,j) * u_1(i,j+1) - Fu_1(i,j) \tag{3.56}$$

$$\begin{aligned} Apu(i,j) * u_2(i,j) &= Awu(i,j) * u_2(i-1,j) + Aeu(i,j) * u_2(i+1,j) + Asu(i,j) \\ &* u_2(i,j-1) + Anu(i,j) * u_2(i,j+1) - Fu_2(i,j) \end{aligned} \tag{3.57}$$

$$\begin{aligned} Apv(i,j) * v_1(i,j) &= Awv(i,j) * v_1(i-1,j) + Aev(i,j) * v_1(i+1,j) + Asv(i,j) \\ &* v_1(i,j-1) + Anv(i,j) * v_1(i,j+1) - Fv_1(i,j) \end{aligned} \tag{3.58}$$

$$\begin{aligned} Apv(i,j) * v_2(i,j) &= Awv(i,j) * v_2(i-1,j) + Aev(i,j) * v_2(i+1,j) + Asv(i,j) \\ &* v_2(i,j-1) + Anv(i,j) * v_2(i,j+1) - Fv_2(i,j) \end{aligned} \tag{3.59}$$

Equations (3.56) to (3.59) present the governing equations for the displacement components u1, v1, u2, and v2, respectively. In each of these equations, the left-hand side contains the unknown variables to be solved, while the right-hand side consists of the corresponding nonlinear terms. For improved clarity and readability, the equations are expressed using the derived coefficients Apu, Awu, Asu, Aeu, Anu, Apv, Awv, Asv, Aev, and Anv.

$$Apu(i,j) = \frac{2}{h_x^2} + \frac{(1-\mu)}{h_y^2} + G_I \tag{3.60}$$

$$Awu(i,j) = Aeu(i,j) = \frac{1}{h_x^2} \tag{3.61}$$

$$Asu(i,j) = Anu(i,j) = \frac{(1-\mu)}{2h_y^2} \tag{3.62}$$

$$Apv(i,j) = \frac{2}{h_y^2} + \frac{(1-\mu)}{h_x^2} + G_I \tag{3.63}$$

$$Awv(i,j) = Aev(i,j) = \frac{(1-\mu)}{2h_x^2} \tag{3.64}$$

$$Asv(i,j) = Anv(i,j) = \frac{1}{h_y^2} \tag{3.65}$$

For Equations (3.60) through (3.65), the coefficient formulas for in-plane solutions are given which are used in Equations (3.56) to (3.59). The interlayer shear modulus is denoted by GI, and hx and hy represent the spatial step sizes in the x- and y-directions, respectively. At each discrete point (i,j), the right-hand side parts given in Equations (3.56) to (3.59), are represented as Fu1(i,j), Fu2(i,j), Fv1(i,j), and Fv2(i,j).

3.4.1 Analysis Steps

The analysis steps for the iterative solution method are given below.

1. The stiffness matrix is obtained.
2. The right-hand side of the w equation which includes non-linear terms is calculated. (refer to Equations (3.47) and (3.49))
3. Solve for the w(i,j) displacement matrix using Equation (3.48). The solution of w is calculated using LU decomposition of stiffness matrix. LU decomposition can be seen as a better way to implement Gauss elimination. This enables us to solve the matrix in a more advantageous way.
4. Check convergence: if the relative error is below the defined tolerance, then exit the inner iteration loop.

5. The stiffness matrices for the in-plane displacements are obtained. . The results of w displacement are used for the right-hand side of in-plane displacements calculation.
6. Compute the right-hand side for u1 and calculate u1 using Equation (3.56).
7. Compute the right-hand side for u2 and calculate u2 using Equation (3.57).
8. Compute the right-hand side for v1 and calculate v1 using Equation (3.58).
9. Compute the right-hand side for v2 and calculate v2 using Equation (3.59).
10. Return to Step 2 and repeat the process.

3.4.2 Matrix Solution Methods

For lateral (transverse, out-of-plane) displacements, a direct matrix solution approach is employed. In this method, the right-hand side vector is multiplied by the inverse of the matrix corresponding to the transverse displacement system. Meanwhile, for the in-plane displacements, the Modified Strongly Implicit (MSI) method is utilized. Originally proposed by Schneider and Zedan (1981) [34], this method applies an Incomplete LU decomposition (ILU decomposition) as the matrix solution technique, offering improved efficiency and convergence for large, sparse systems.

3.4.3 Relaxation Parameters

To address convergence issues, successive under-relaxation (SUR) parameter, denoted by alpha (α), is employed for to the transverse variable w. A non-dimensional maximum displacement parameter, defined as 2*w(1,1)/(h1+h2), obtained from numerical experiments, is used to adjust the under-relaxation parameter dynamically. The previous step lateral displacement is denoted by wo(i, j). Initially the value of α is set to 0.5. As the solution progresses and convergence improves, α is gradually increased up to a maximum of 1, thereby accelerating convergence in later iterations. The updated displacement w is calculated using a weighted interpolation as in Equation (3.66).

$$w(i,j) = \alpha * w(i,j) + (1-\alpha) * wo(i,j) \tag{3.66}$$

Similarly, for the convergence of in-plane deflection calculation is done using beta parameter of under-relaxation employing successive over-relaxation (SOR). For the in-plane displacements, a constant over-relaxation factor of 1.4 was found to be appropriate after a series of numerical trials.

$$u(i,j) = \beta * u(i,j) + (1-\beta) * uo(i,j) \tag{3.67}$$

$$v(i,j) = \beta * v(i,j) + (1-\beta) * vo(i,j) \tag{3.68}$$

3.4.4 Stress Calculation

The stress values in the mathematical model (FDM model) are obtained by combining membrane and bending stresses for each layer, considering their respective directions (tensile or compressive). Since both glass layers rotate in the same direction under bending, the combination of membrane and bending stresses varies depending only on whether the point of interest lies on the upper or lower surface of a given layer.

Table 3.3 Summation of bending stresses in the corresponding function of the code.

	Top Plate	Bottom Plate
Tension Side	(+)	(+)
Compression Side	(-)	(-)

The membrane stresses and bending stresses are summed with respect to Table 3.3. The rotations are separate for both layers. Thus, assuming positive bending moment; top parts of each layer is tensile (positive signed stress) while the bottom part of each layer is compressive (negative signed stress).

The shear and axial stresses at the top and bottom surfaces of each layer are utilized to calculate the principal stresses using the Mohr's Circle method. This results in the determination of the first principal stress (σ_1) and the second principal stress (σ_2). While the first principal stress typically has a larger magnitude, it is important to note that the second principal stress may prove to be more critical, especially when considering the potential for compressive failure modes.

Additionally, the interlayer shear deformation mode is considered, leading to the incorporation of interlayer shear failure mode into the analysis. As a result, the relevant stresses are calculated, taking into account the deformation values of the laminated glass. In total, six stresses are determined;

- First principal stress for the upper layer
- Second principal stress for the upper layer
- First principal stress for the lower layer
- Second principal stress for the lower layer
- Interlayer shear stress in the xz direction
- Interlayer shear stress in the yz direction

The symbols for principal stresses used in the following sections are summarized in Table 3.4.

Table 3.4 Symbols for Principal Stresses

Principal Stress	Symbols
First Principal Stress	σ_1
Second Principal Stress	σ_2

CHAPTER 4

RESULTS

4.1 Model and Solution Implementation

The developed mathematical model is converted into code using the Python programming language version 3.11.4.

Data inputs are taken for variables below to run the model code.

- Length in x-direction (in meters),
- Length in y-direction (in meters),
- Glass layers thicknesses (in meters),
- Interlayer thickness (in meters),
- Number of divisions in x-direction,
- Number of divisions in y-direction,
- Elastic modulus for glass layer (in kPa),
- Shear modulus for the interlayer (in kPa),
- Poisson’s ratio for glass layers,
- Loading magnitude (in kPa).

In Figure 4.1, a 3D visualization of the laminated glass plate model is presented, along with the corresponding orthogonal coordinate system. The z-direction represents the transverse direction, while the x and y directions define the in-plane directions.

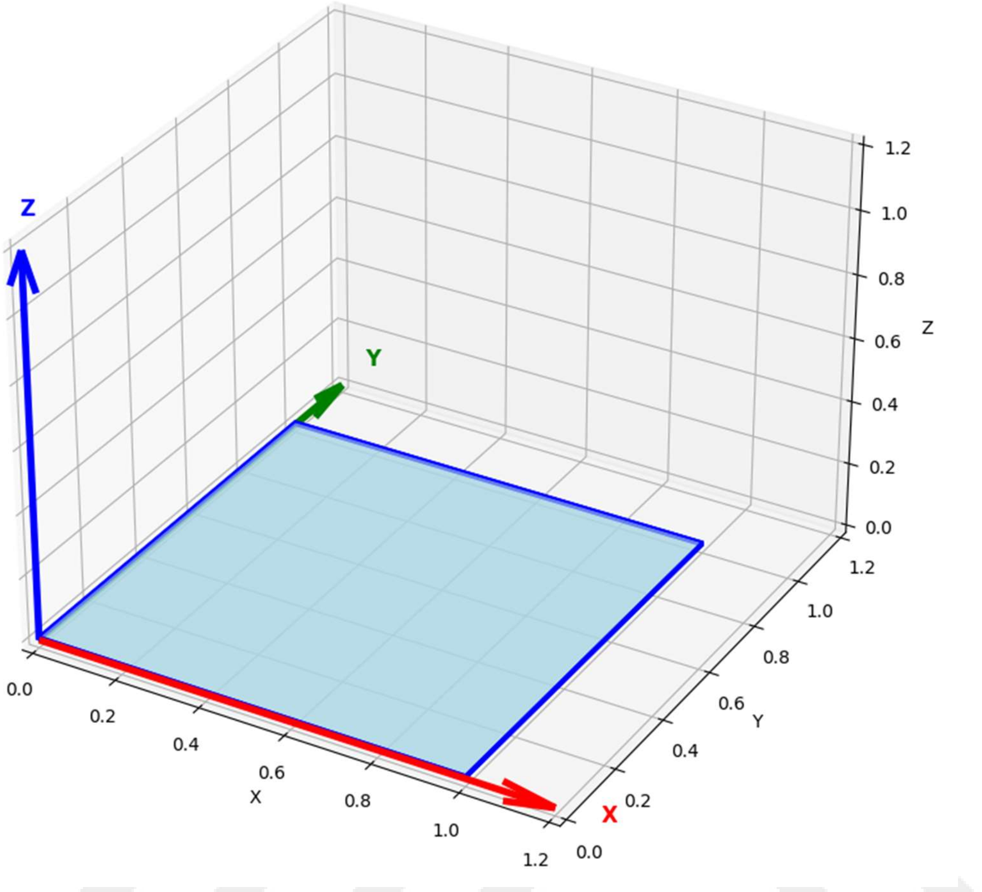

Figure 4.1 3D View of the laminated glass plate model and coordinate system

The loading for the plate is uniform pressure applied downwards on top surface (+z surface in Figure 4.1).

To validate and compare the FDM model results, an FEM model for laminated glass was developed and evaluated in terms of result accuracy and computational performance. Constructing this model required rigorous effort due to the inclusion of extremely thin interlayer elements modeled as solids, which were connected to the upper and lower glass layers. Given the aspect ratio constraints of solid elements, a high mesh density was necessary to ensure accurate results. The finite element model is constructed using C3D20 elements within the Abaqus software, which are 20-node quadratic brick elements suitable for capturing complex 3D stress states. The applied loading condition—transverse pressure—was kept consistent with the FDM model for direct comparison. The loading configuration for the FEM analysis is illustrated in Figure 4.2 below. The results are obtained from our developed mathematical FDM model unless explicitly stated as FEM results.

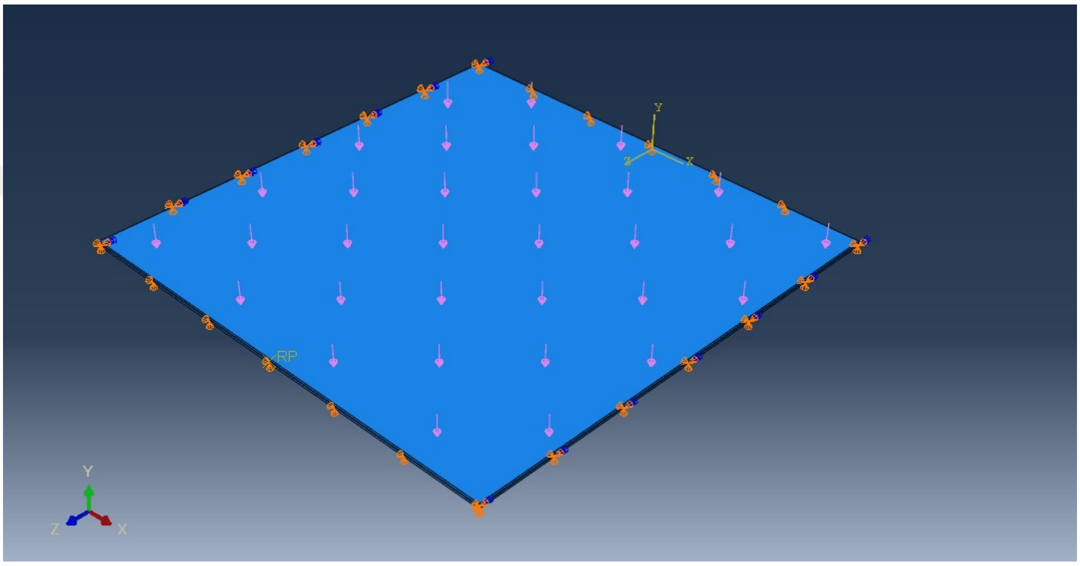

Figure 4.2 Abaqus FEM model under pressure load

4.2 Case 1: Symmetrical S.S.-Clamped- S.S. -Clamped (Benchmark)

The first case is symmetrical and is calculated as a benchmark for the unsymmetrical boundary condition cases. It has already been extensively studied in previous work and will therefore not be discussed in detail here. Its primary purpose is to serve as a reference for the unsymmetrical cases, which are presented in the following sections.

In Figure 4.3, the left and right edges are clamped (u,v,w = 0, ∂θ/∂n = 0) while top and bottom edges are simply supported edges (∂θ/∂n ≠ 0).

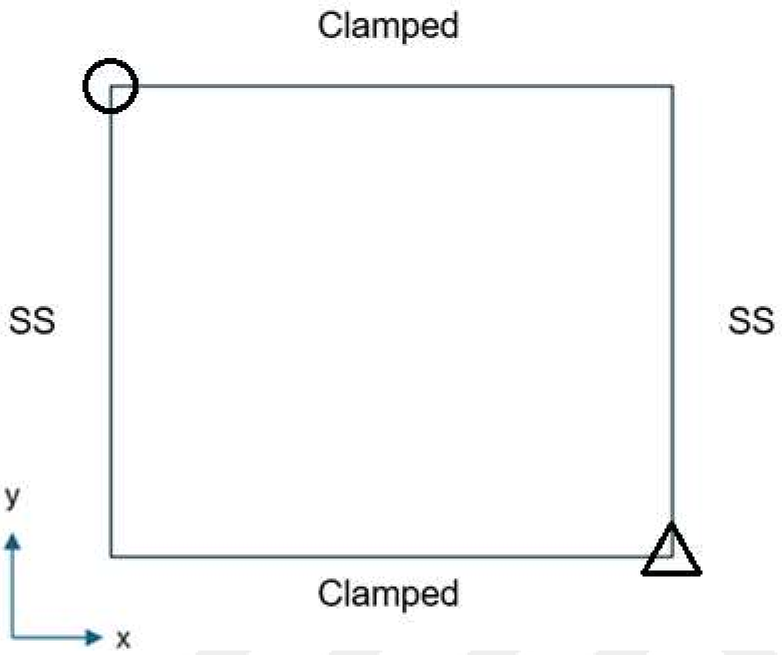

Figure 4.3 Case 1 Boundary conditions for the plate

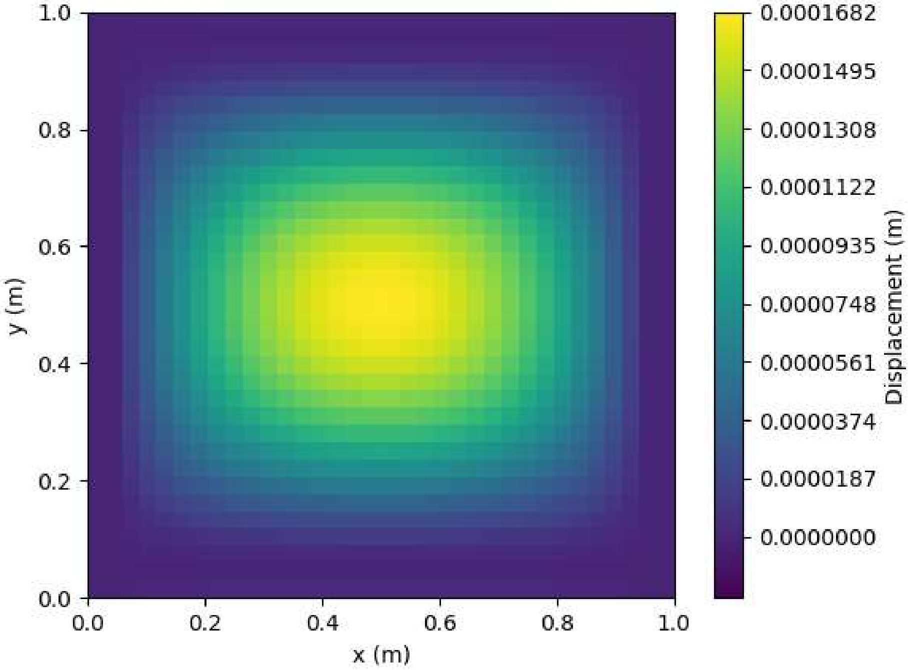

Figure 4.4 Transverse displacement of the plate

The displacement contour in the middle is an ellipse rather than circle, which can be observed in Figure 4.4. That pattern is expected due to the different boundary conditions in x and y directions. The simply supported boundaries are less stiff, and the transverse displacement leans toward these edges.

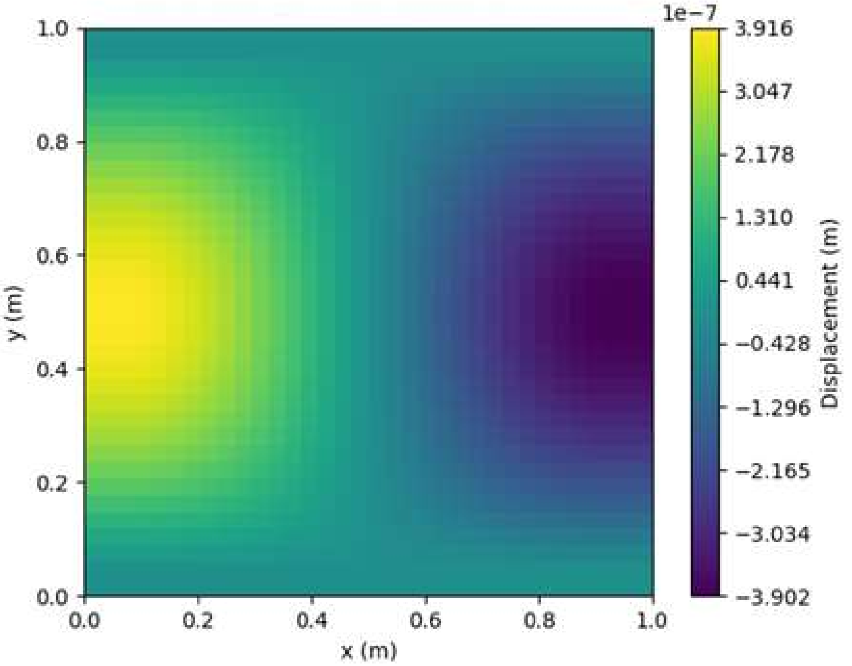

Figure 4.5 Axial displacement in x direction of upper plate (u1)

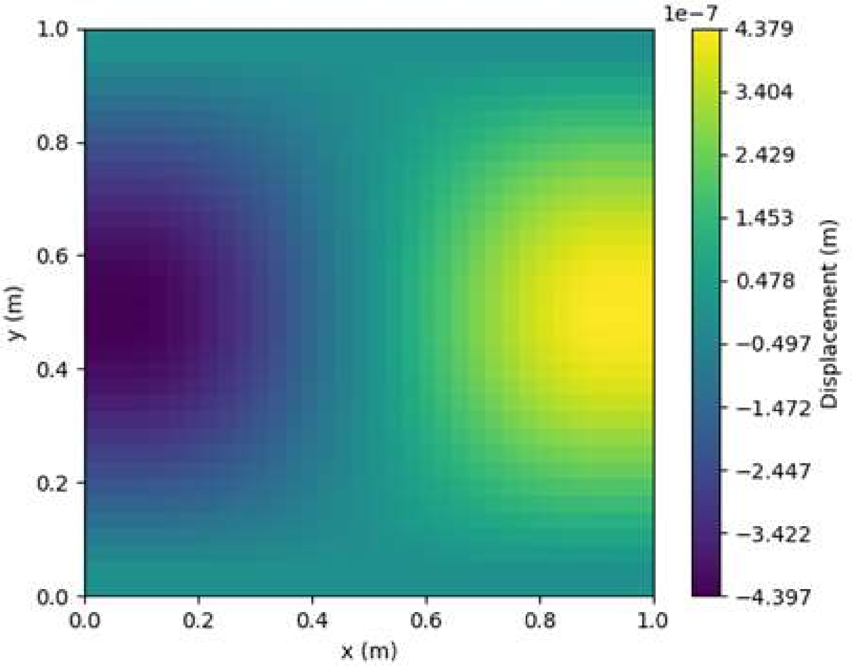

Figure 4.6 Axial displacement in x direction of lower plate (u2)

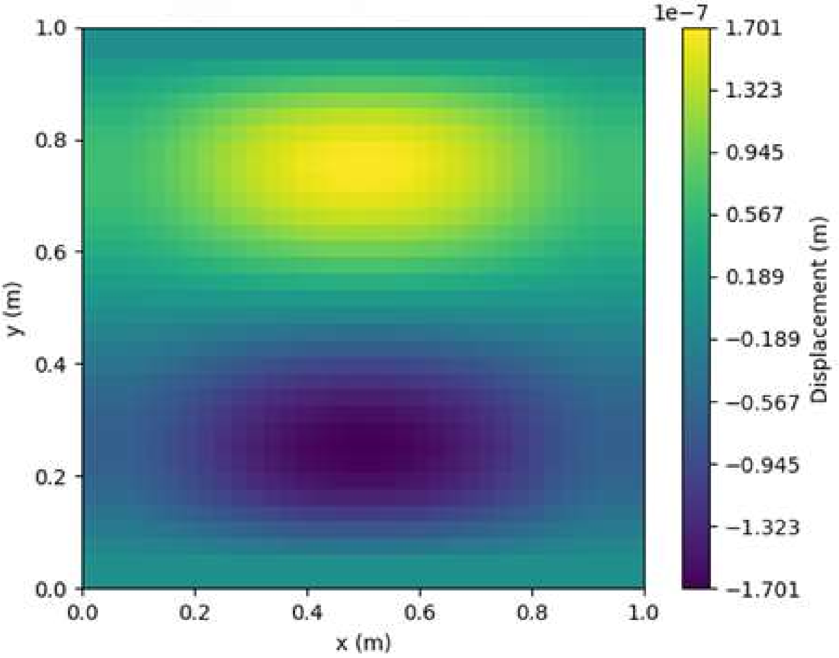

Figure 4.7 Axial displacement in y direction of upper plate (v1)

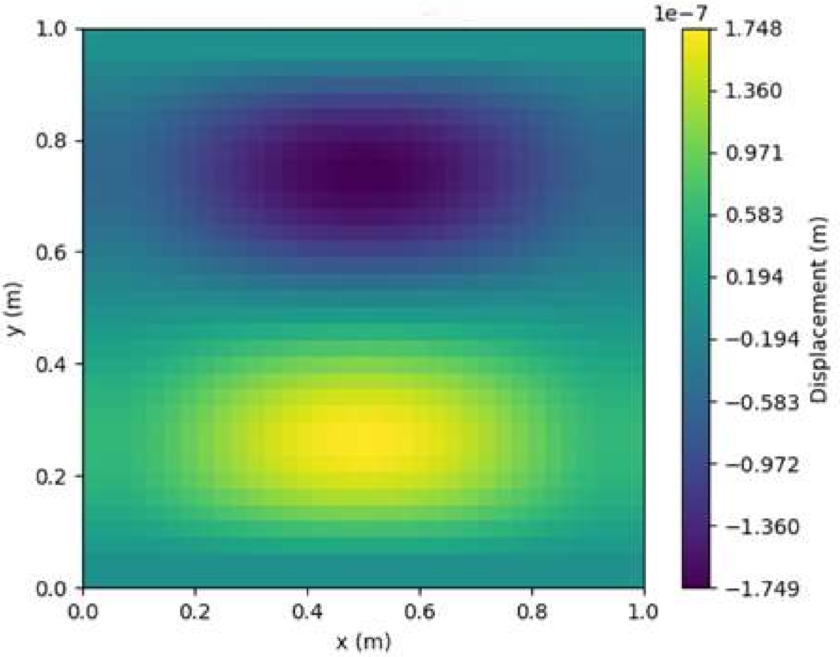

Figure 4.8 Axial displacement in y direction of lower plate (v2)

When analyzing the in-plane x-displacements (u1, u2) and y-displacements (v1, v2) , it is apparent that their spatial distributions are oriented orthogonally within the plane as in Figure 4.5, Figure 4.6, Figure 4.7 and Figure 4.8. The u-displacements, representing in-plane motion along the x-axis, show a distribution parallel to the x-direction, while the v-displacements, corresponding to in-plane motion along the y-axis, are primarily distributed parallel to the y-direction. As expected, non-zero negative in-plane displacements are observed along the simply supported edges, whereas clamped edges exhibit zero in-plane displacements.

4.3 Case 2: Unsymmetrical Clamped - Clamped - S.S. - S.S. Edges

In this case, the rectangular plate is subjected to a specific configuration of boundary conditions in which two adjacent edges are assigned simply supported (SS) conditions, while the remaining two adjacent edges are constrained with clamped boundary conditions. To elaborate further, the simply supported boundary conditions—applied to two adjoining edges of the plate—allow all types of translation and rotational displacements except transverse displacement normal to the plate. Conversely, the clamped boundary conditions imposed on the other two adjoining edges enforce a fully fixed support, preventing both translational displacements and rotations along the edge, thereby simulating a rigid and immovable connection.

This arrangement of mixed boundary conditions —clamped on the top and left edges, and simply supported on the bottom and right edges— is explicitly illustrated in Figure 4.9.

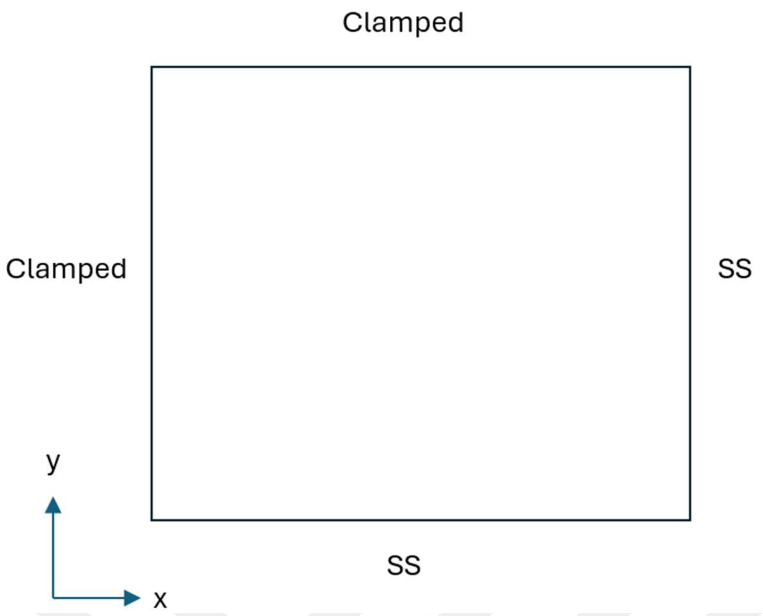

Figure 4.9 Case 2 Boundary conditions for the plate

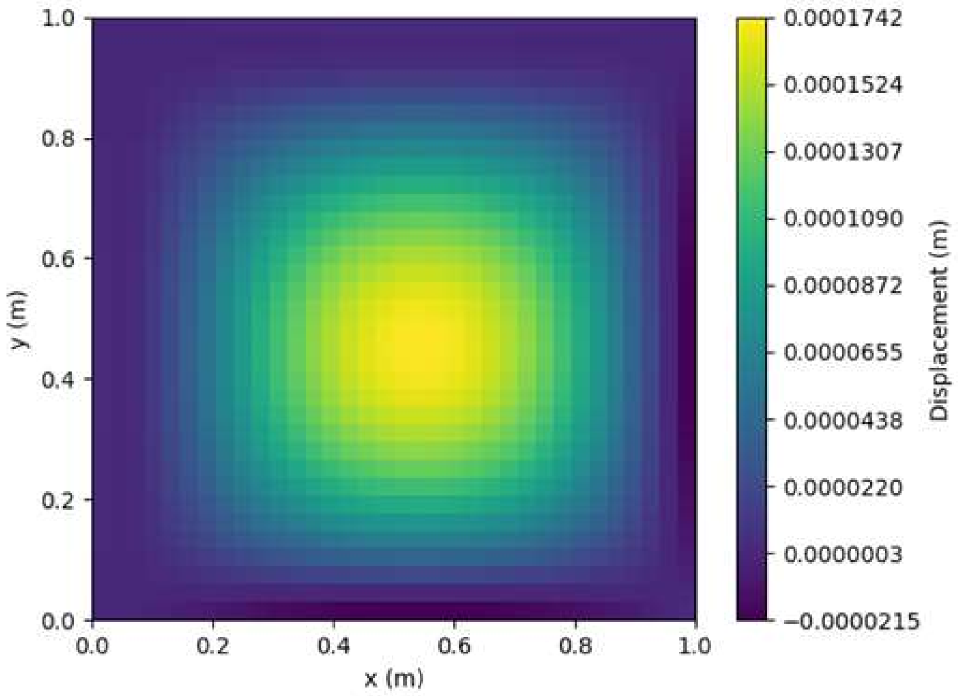

Figure 4.10 Transverse displacement of the plate

The transverse displacements are the dominant displacements for transverse pressure loading. Thus, the emphasis is put on those displacements and compared with the equivalent FEM model results. In the FEM model below, the boundary conditions and displacement extraction path are specified. Also, the deformation shape can be observed.

Both Case 1 and Case 2 have the same number of clamped and simply supported edges. The only difference is that the boundary condition in Case 1 is symmetric, while in Case 2 it is not. Case 2 results in a higher maximum displacement compared to Case 1, indicating that the asymmetry leads to a less stiff structural response. From an engineering perspective, asymmetry typically results in reduced stiffness, so this outcome is consistent with expectations.

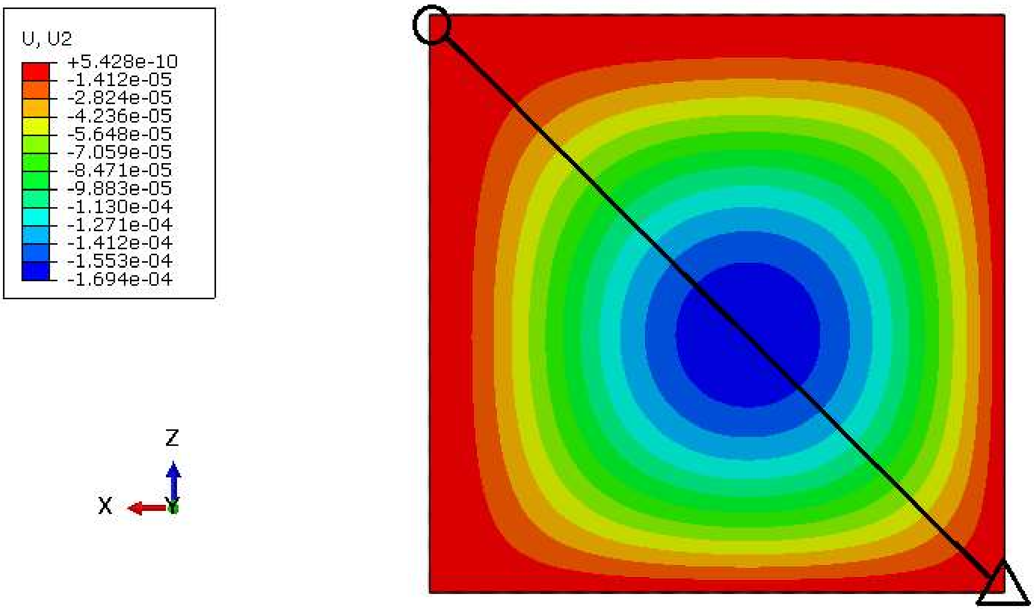

Figure 4.11 Transverse displacement results of FEM analysis

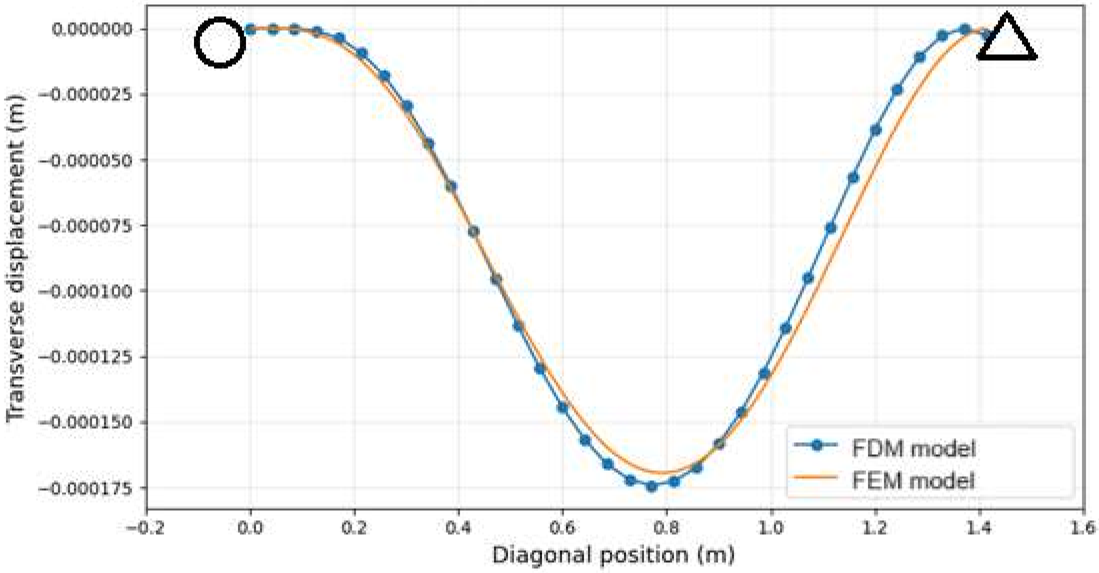

Figure 4.12 Case-2 Transverse displacements from mathematical model and FEM analysis

In Figure 4.12, the FEM displacements are extracted along the diagonal in Figure 4.11, starting at the clamped-clamped edge (marked with a circle) and ending at the S.S.-S.S. edge (marked with a triangle). And the Finite Difference Method (FDM) model displacements are extracted along top-left and bottom-right corners of Figure 4.10, starting at top-left corner. The circle and triangle symbols in Figure 4.12 correspond to the same points denoted by these symbols in Figure 4.11.

The computational results obtained from both the Finite Difference Method (FDM) and Finite Element Method (FEM) models demonstrate strong agreement, with nearly indistinguishable deformation profiles and closely matching quantitative values. Specifically, the spatial distribution of displacements, as well as the magnitude of local strain concentrations, exhibit a high degree of correlation between the two numerical approaches.

A key observation is the systematic shift of the maximum transverse displacement’s lowest points toward the S.S.- S.S. edge region compared to the symmetrical solution, which has a maximum displacement point in the middle of the plate. This trend arises due to the inherent mechanical contrast between boundary conditions: simply supported edges, which allow rotational freedom, exhibit significantly greater compliance than clamped edges, which fully restrain both rotations and translations. Consequently, deformation localizes preferentially near the less constrained simply supported edge—a behavior well-documented in plate mechanics literature [14]. The consistency between FDM and FEM predictions not only reinforces confidence in the FDM implementation but also aligns with first-principles expectations for thin-plate deformation under mixed boundary conditions.

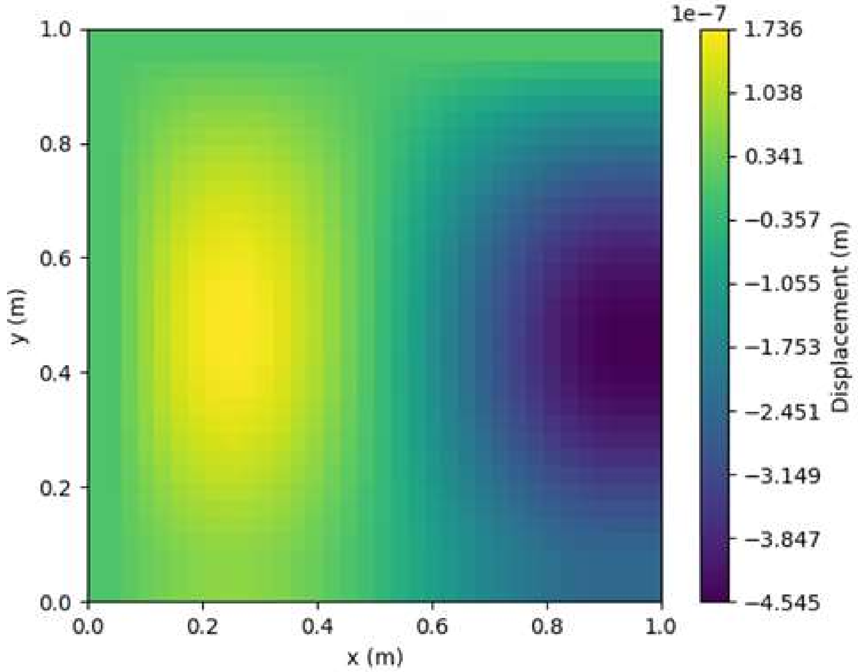

Figure 4.13 Axial displacement in x direction of upper plate (u1)

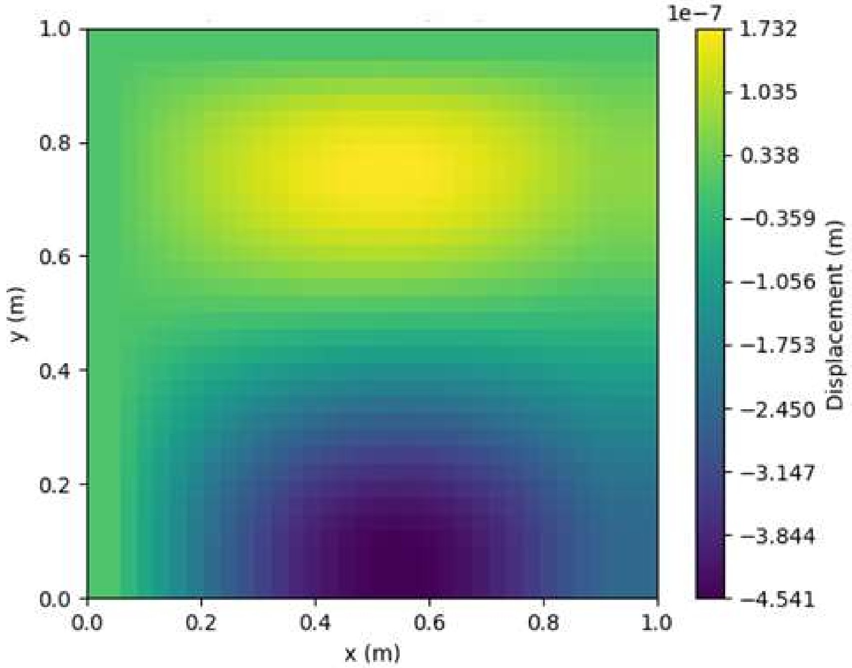

Figure 4.14 Axial displacement in y direction of upper plate (v1)

When analyzing the in-plane x-displacements (u1) and y-displacements (v1) for the upper glass layer in Figure 4.13 and Figure 4.14, it is apparent that their spatial distributions are oriented orthogonally within the plane. The u-displacements, representing in-plane motion along the x-axis, show a distribution parallel to the x-direction, while the v-displacements, corresponding to in-plane motion along the y-axis, are primarily distributed parallel to the y-direction. As expected, non-zero negative in-plane displacements are observed along the simply supported edges, whereas clamped edges exhibit zero in-plane displacements.

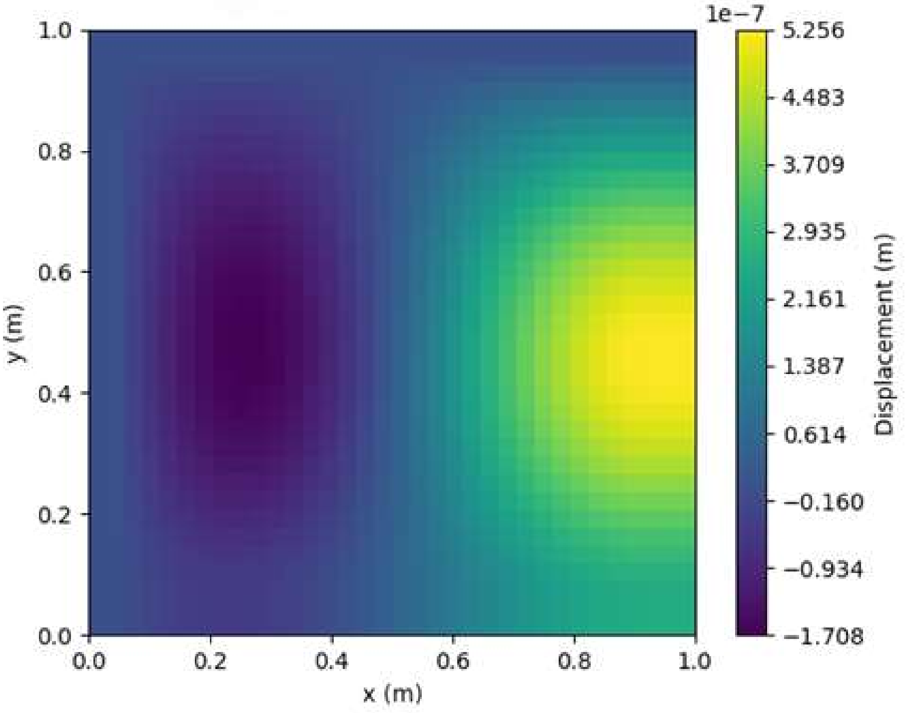

Figure 4.15 Axial displacement in x direction of lower plate (u2)

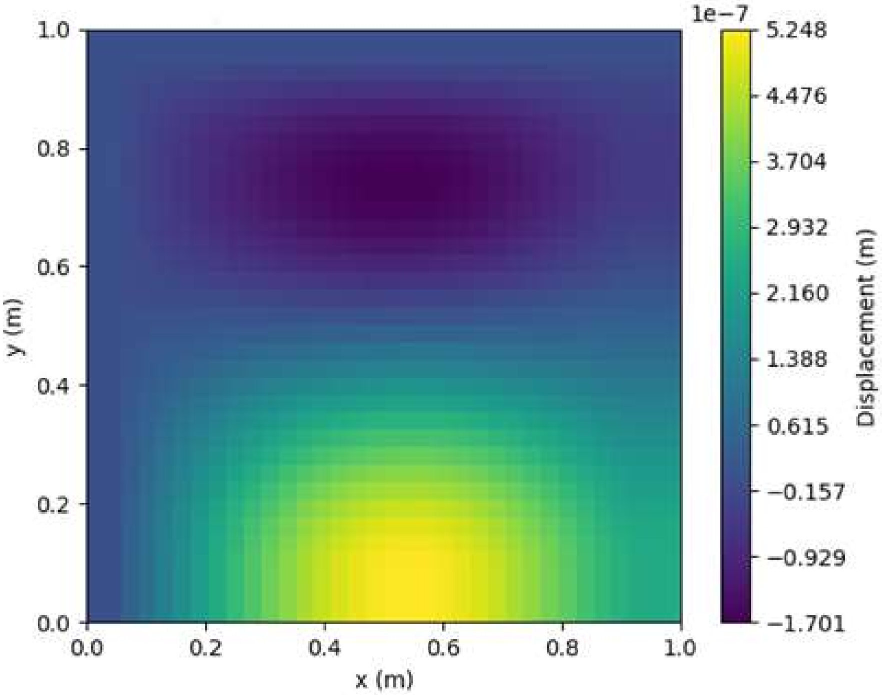

Figure 4.16 Axial displacement in y direction of lower plate (v2)

In Figure 4.15 and Figure 4.16, the x-displacements (u2) and y-displacements (v2) observed in the lower glass layer exhibit a spatial distribution pattern similar to that of the upper glass layer. Specifically, the u2 displacements are predominantly aligned along the x-direction, while the v2 displacements are primarily distributed along the y-direction. Similar to the results observed in the upper layer, the lower layer also exhibits non-zero negative in-plane displacements along the simply supported edges. Conversely, the clamped edges maintain zero in-plane displacements, consistent with the expected boundary conditions.

A clear symmetry is observed in the displacement distributions of the upper and lower glass layers with respect to the interlayer plane (i.e., the z-plane, whose normal corresponds to the transverse direction). At a corresponding point on the 2D plane, the in-plane displacements of the two layers exhibit similar magnitudes but opposite directions, indicating mirrored deformation behavior across the laminate.

For all in-plane displacement components—including u1, v1 (upper layer) and u2, v2 (lower layer)—their magnitudes are negligible when compared to the transverse (out-of-plane) displacements observed under the same loading conditions. That aligns with established findings in prior studies [20], where transverse deformations consistently dominate the structural response of similar laminated glass systems. The minimal in-plane displacements can be attributed to the high in-plane stiffness of the glass layers, which restricts deformation along the x- and y-axes, while the comparatively lower out-of-plane stiffness allows for more pronounced deflections in the z-direction. Furthermore, the clamped boundary conditions, which typically constrain in-plane motion at the edges, further suppress u and v displacements, reinforcing the expected deformation hierarchy where transverse displacements govern the overall mechanical behavior.

4.3.1 Comparison with Theoretical Limits (Monolithic/Layered)

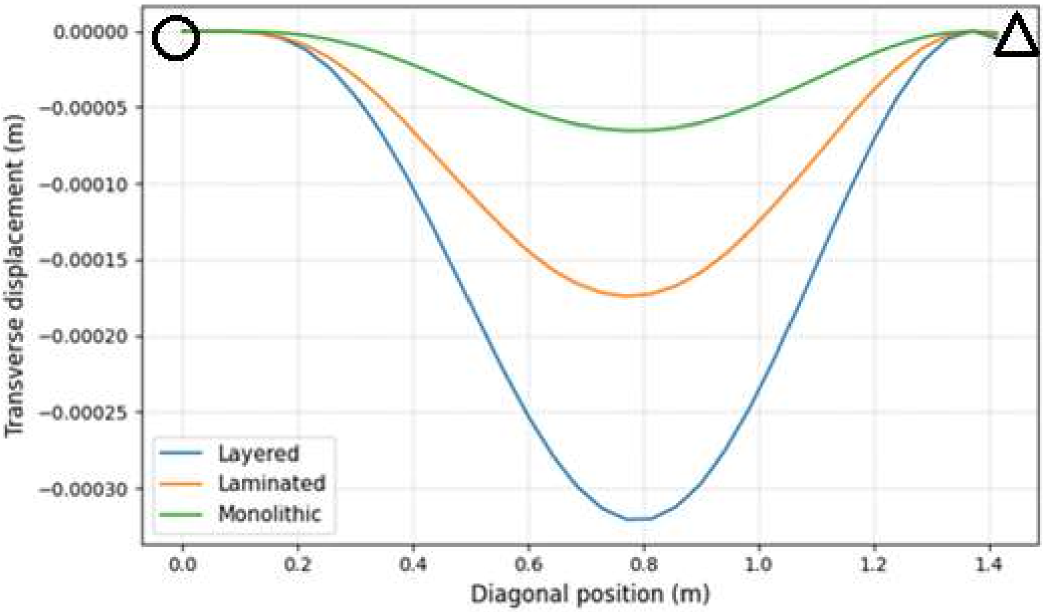

Figure 4.17 Comparison of transverse displacements along diagonal line with theoretical limits

The theoretical limits for laminated glass plate behavior were established in prior work by Mohareb [36]. The first limit corresponds to monolithic glass, defined as a single-layer glass plate of full thickness without any interlayer adhesive. The second limit represents layered glass, which consists of multiple glass layers identical to those in laminated glass but with zero shear stiffness in the interlayer. In this layered limit, the glass layers are free to slide relative to one another without shear resistance. Laminated glass, in theory, exhibits behavior intermediate between these two extremes. Its specific response—whether closer to the monolithic or layered limit—depends on the shear stiffness of the polymer interlayer material.

In the present analysis (Figure 4.17), the deformation of laminated glass falls between these two theoretical limits. The circle and triangle symbols in Figure 4.17 correspond to the same points denoted by these symbols in Figure 4.11. While all cases (monolithic, layered, and laminated) exhibit qualitatively similar transverse displacement shapes, the magnitudes differ significantly due to their distinct stiffness characteristics. These results align with theoretical expectations: laminated glass, by virtue of its finite interlayer shear stiffness, demonstrates greater rigidity than the layered limit but remains less stiff than the monolithic case, as the polymer interlayer cannot match the shear stiffness.

4.3.2 Stress Results

Principal in-plane stresses for both glass layers and transverse shear stress for adhesive interlayer are derived from the displacement results. The naming conventions used here correspond to those listed in Table 3.4.

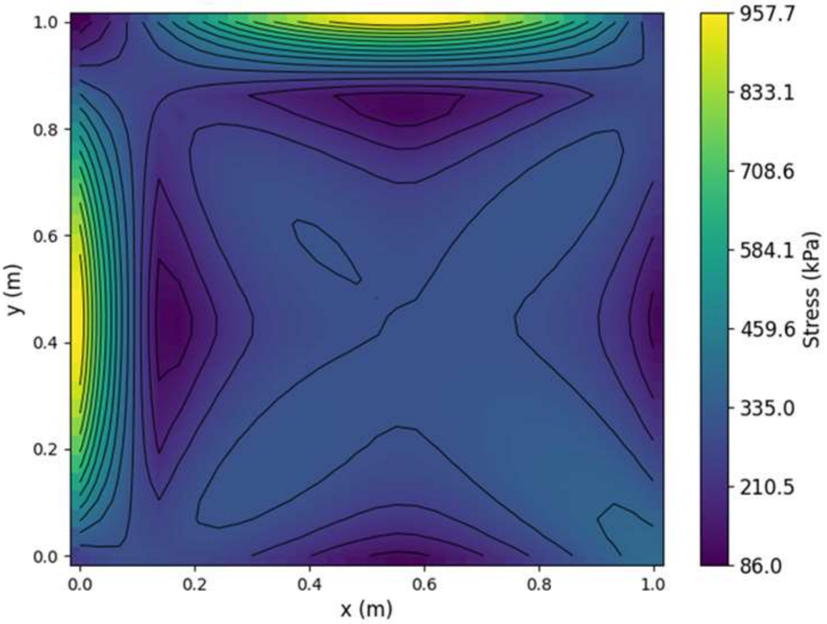

Figure 4.18 First principal stress (σ1) in upper layer

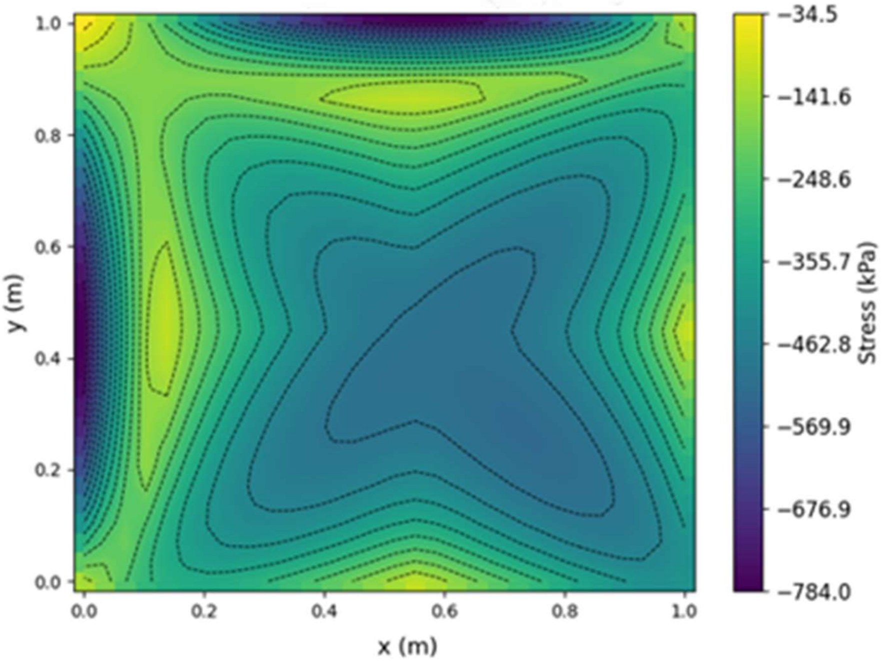

Figure 4.19 Second principal stress (σ2) in upper layer

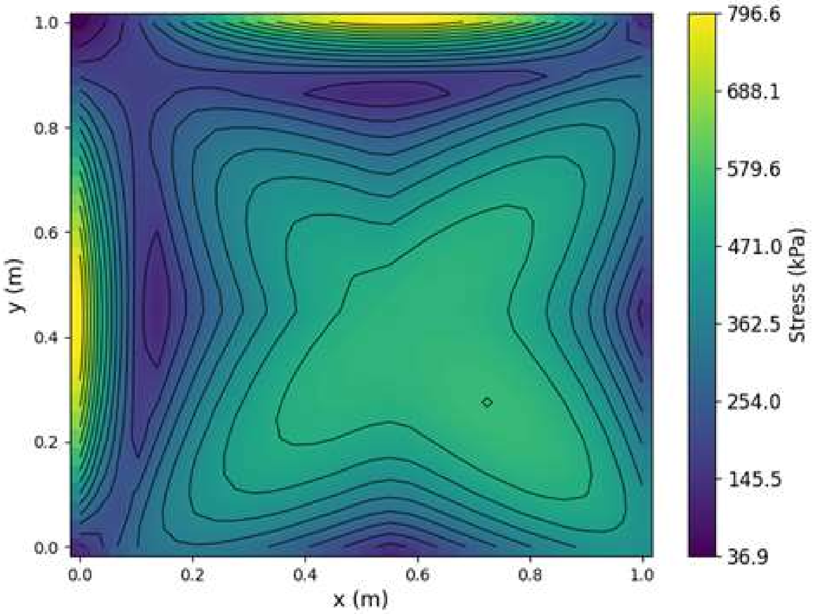

Figure 4.20 First principal stress (σ1 in lower layer

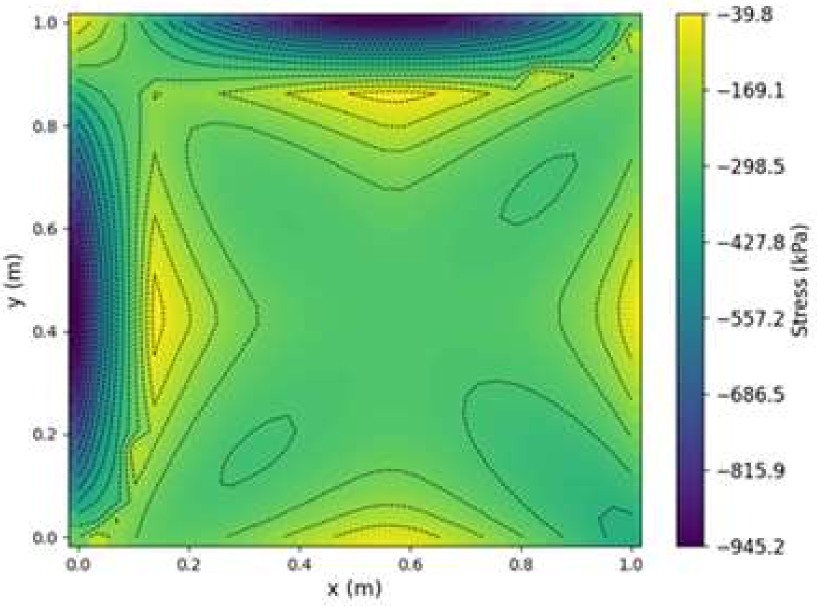

Figure 4.21 Second principal stress (σ2) in lower layer

Figure 4.18, Figure 4.19, Figure 4.20, and Figure 4.21 illustrate the first and second principal stresses for Case 2, shown separately for the upper and lower glass layers. In both layers, the principal stresses reach their maximum values near the clamped edges. This aligns with theoretical expectations, as clamped edges impose stricter displacement constraints, leading to higher local stiffness compared to simply supported edges. The points of minimum absolute principal stresses typically occur slightly inward from the clamped boundaries, in close proximity to the regions of maximum absolute stress. For Case 2, the sign of a given principal stress remains consistent throughout each individual layer, indicating no sign reversal within the layer.

The principal stress distributions between the upper and lower layers are not perfectly symmetric. This asymmetry arises because the principal stresses are influenced by the combined effect of membrane and bending stresses. If bending were the sole contributor, the stress distributions would be symmetric with respect to the interlayer plane.

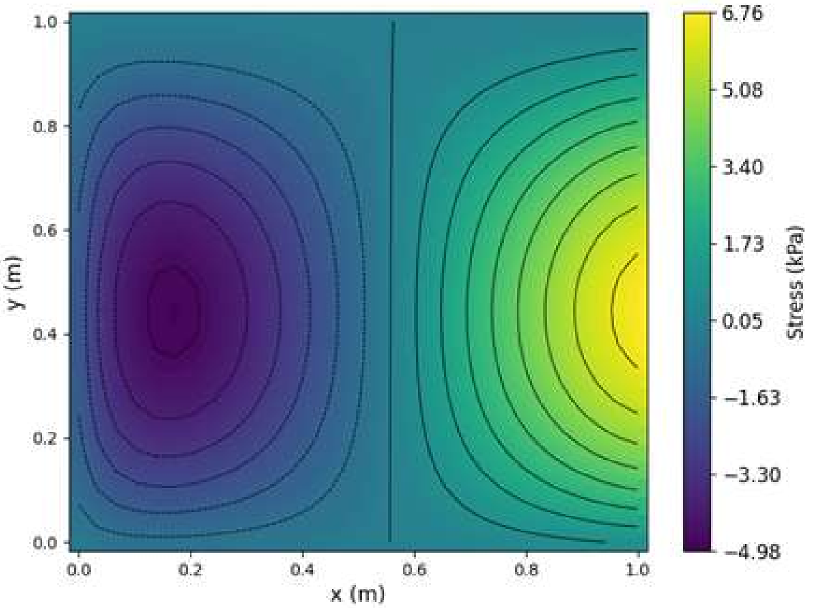

Figure 4.22 Distribution of transverse shear stress τ_{xz} in the interlayer

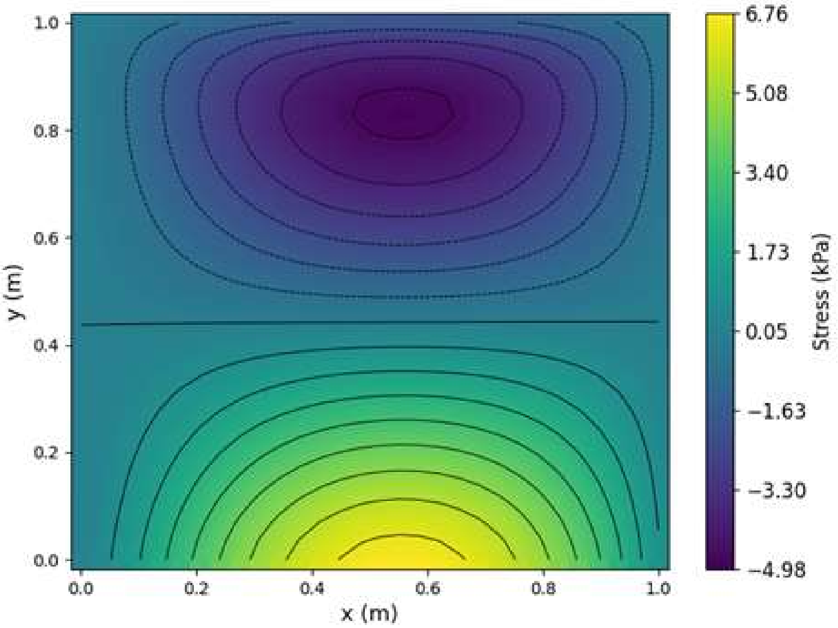

Figure 4.23 Distribution of transverse shear stress τ_{yz} in the interlayer

The transverse shear stress distributions within the interlayer are presented in Figure 4.22 and Figure 4.23. The shear stress on the xz-plane (τ_{xz}) primarily varies along the x-direction, whereas the shear stress on the yz-plane (τ_{yz}) exhibits stronger variation along the y-direction compared to the x-direction. Unlike the principal stresses in the glass layers—which are highest near the clamped edges in Case 2—the interlayer shear stresses are more pronounced near the simply supported edges. Notably, for both τ_{xz} and τ_{yz} , the shear stress values drop to zero at the mid-plane of the interlayer when viewed in the out-of-plane (z) direction.

4.3.3 Convergence of transverse displacement for interlayer thickness

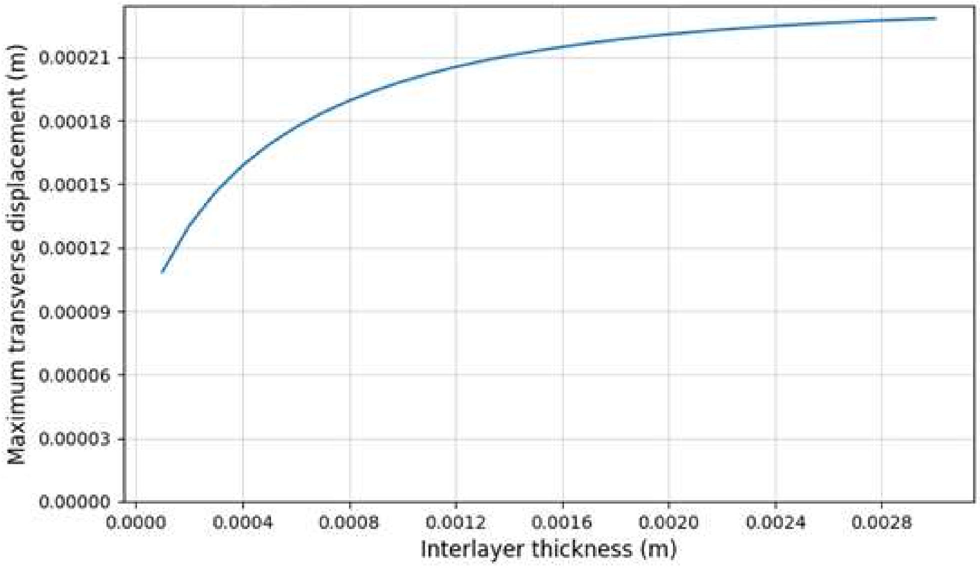

Figure 4.24 Case-2 interlayer thickness versus maximum transverse displacement

Increasing the glass layer thickness has a direct positive effect on the overall stiffness of the laminated plate, which aligns with the physical nature of the problem. However, increasing the interlayer adhesive thickness while keeping other parameters constant reduces stiffness and increases the transverse displacement of the plate. To explore this phenomenon, the interlayer thickness is varied over a wide range. The results show that as the interlayer thickness increases, the maximum transverse displacement also increases, eventually converging after a certain point as shown in Figure 4.24.

4.4 Case 3: Unsymmetrical Clamped-Clamped-Clamped-S.S. Edges

In Case 3, the square plate is constrained with clamped conditions on the top, left, and right edges, providing full fixity. Only the bottom edge in Figure 4.25 has a simply supported condition, allowing rotation while restricting transverse displacement. This setup creates asymmetric stiffness over the plate. The square geometry implies equal edge lengths, making corner transitions (where clamped edge meets simply supported edge) critical for stress analysis.

Figure 4.25 Case 3 Boundary conditions for the plate

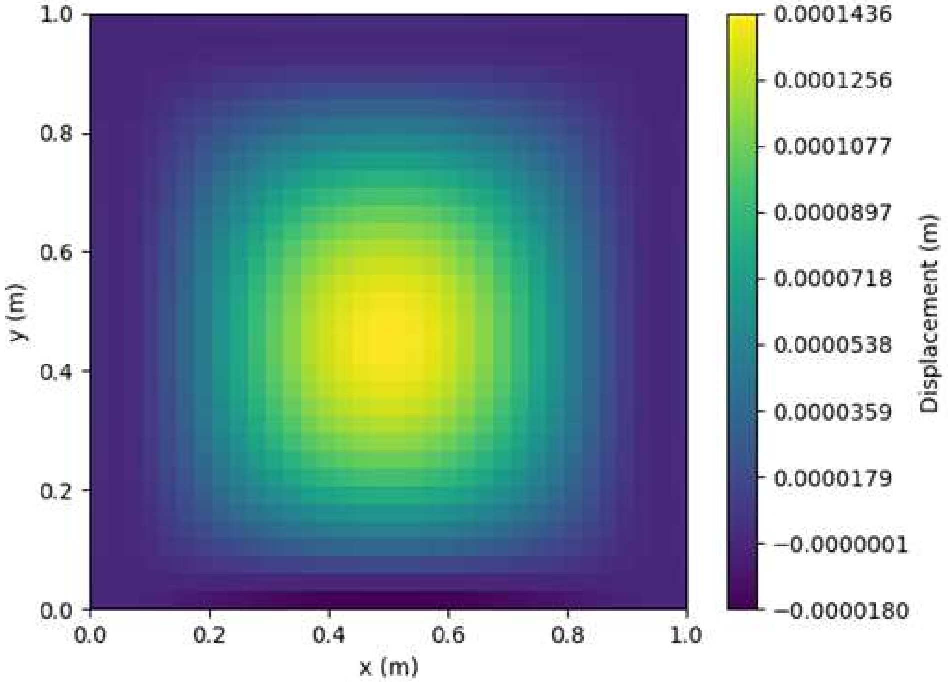

Figure 4.26 Transverse displacement of the plate

Like in Case 3, the transverse displacements are the dominant displacements for transverse pressure loading. Thus again, those displacements are compared with the equivalent FEM model results. In the FEM model below, the boundary conditions and displacement extraction path are similarly specified. Also, the deformation shapes can be observed.

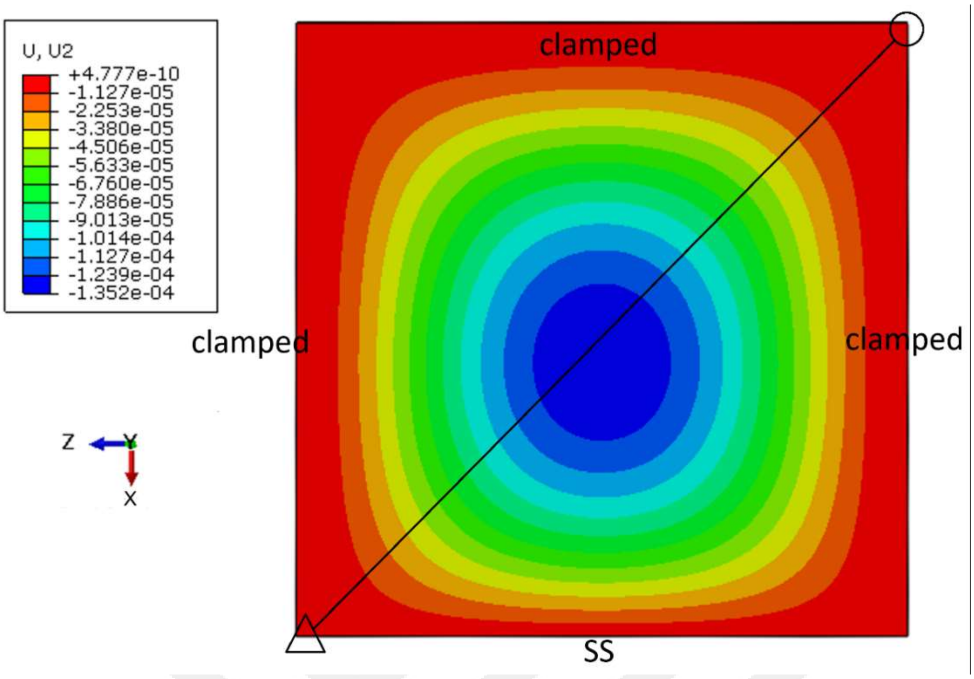

Figure 4.27 Transverse displacement results of FEM analysis

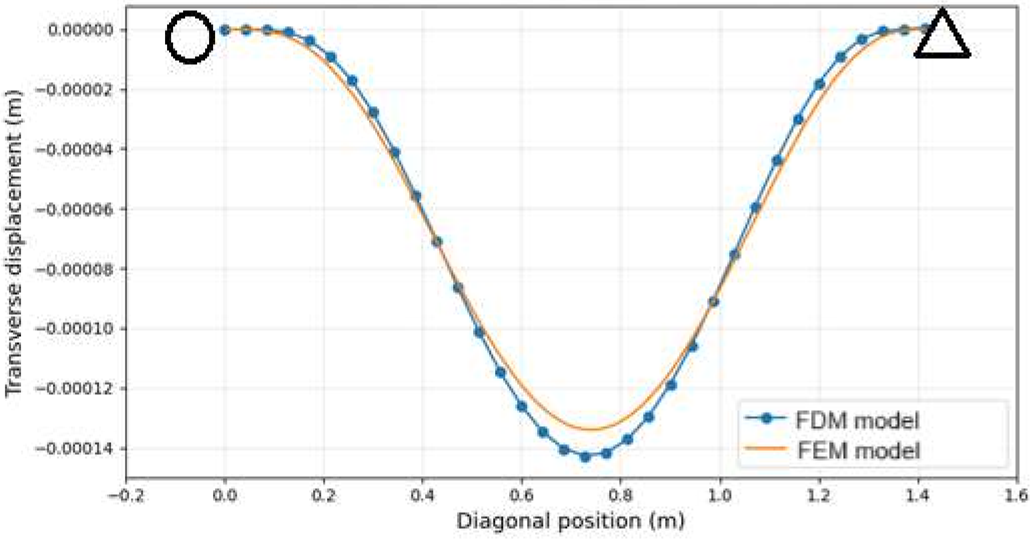

Figure 4.28 Case-3 Transverse displacements from mathematical model and FEM analysis

In Figure 4.28, the FEM displacements are extracted along the diagonal in Figure 4.27, starting at the clamped-clamped edge (marked with a circle) and ending at the clamped-S.S. edge (marked with a triangle), and the Finite Difference Method (FDM) model displacements are extracted along top-left and bottom-right corners of Figure 4.26, starting at top-left corner. The circle and triangle symbols in Figure 4.28 correspond to the same points denoted by these symbols in Figure 4.27.

The computational results obtained from both the Finite Difference Method (FDM) and Finite Element Method (FEM) models again demonstrate strong agreement, with nearly indistinguishable deformation profiles and closely matching quantitative values. Specifically, the spatial distribution of displacements, as well as the magnitude of local strain concentrations, exhibit a high degree of correlation between the two numerical approaches.

A key observation is the systematic shift of the maximum transverse displacement's lowest points toward the simply supported edge region compared to the symmetrical solution, which has a maximum displacement point in the middle of the plate. This trend arises due to the inherent mechanical contrast between boundary conditions: simple supports, which allow rotational freedom, exhibit significantly greater compliance than clamped edges, which fully restrain both rotations and translations. Consequently, deformation localizes preferentially near the less constrained (simply supported) edge—a behavior consistent with Case 3 and again in agreement with classical plate theory literature [14]. The consistency between FDM and FEM predictions not only reinforces confidence in the FDM implementation but also aligns with first-principles expectations for thin-plate deformation under mixed boundary conditions.

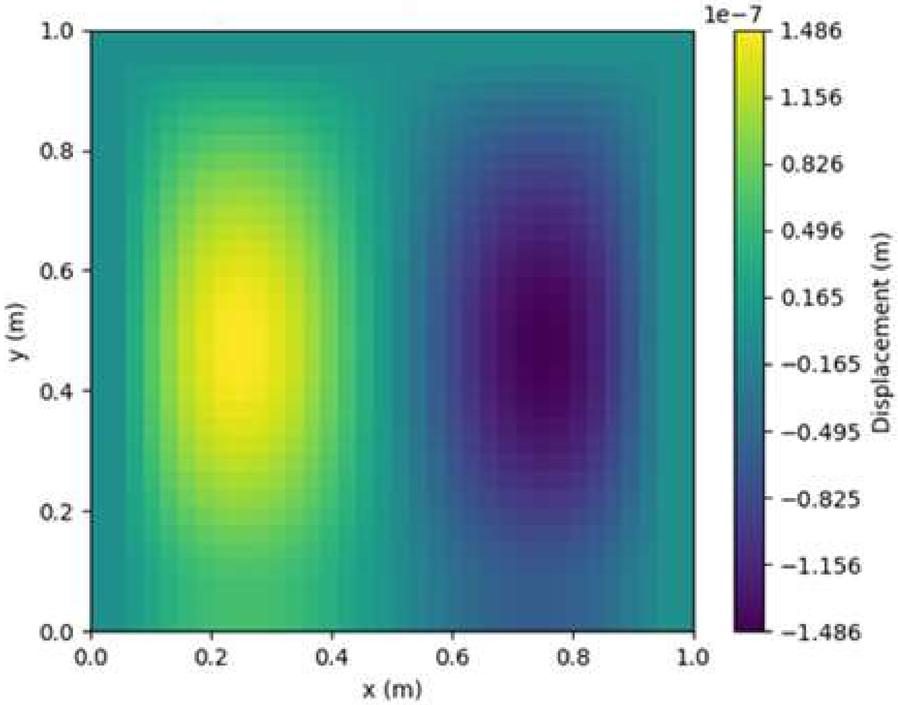

Figure 4.29 Axial displacement in x direction of upper plate (u1)

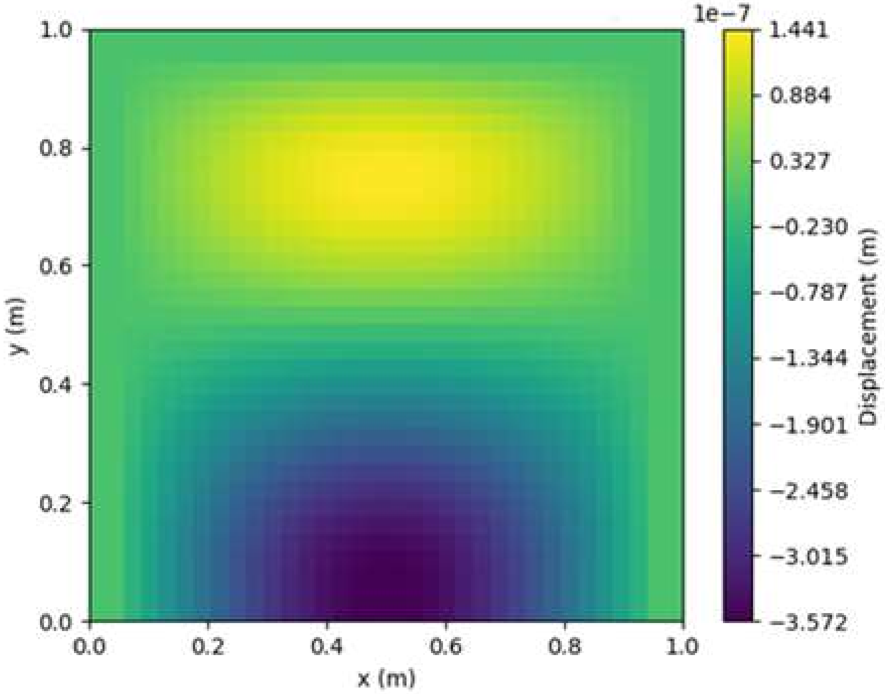

Figure 4.30 Axial displacement in y direction of upper plate (v1)

When analyzing the in-plane x-displacements (u1) and y-displacements (v1) for the upper glass layer in Figure 4.29 and Figure 4.30, it is apparent that their spatial distributions are oriented orthogonally within the plane. The u1 displacements, representing in-plane motion along the x-axis, show a dominant variation along the x-direction, while the v-displacements, corresponding to in-plane motion along the y-axis, are primarily distributed parallel to the y-direction. Additionally, the deformation behavior at the edges aligns with theoretical expectations: clamped boundary conditions enforce zero in-plane displacements, whereas the simply supported edges allow for non-zero in-plane displacements.

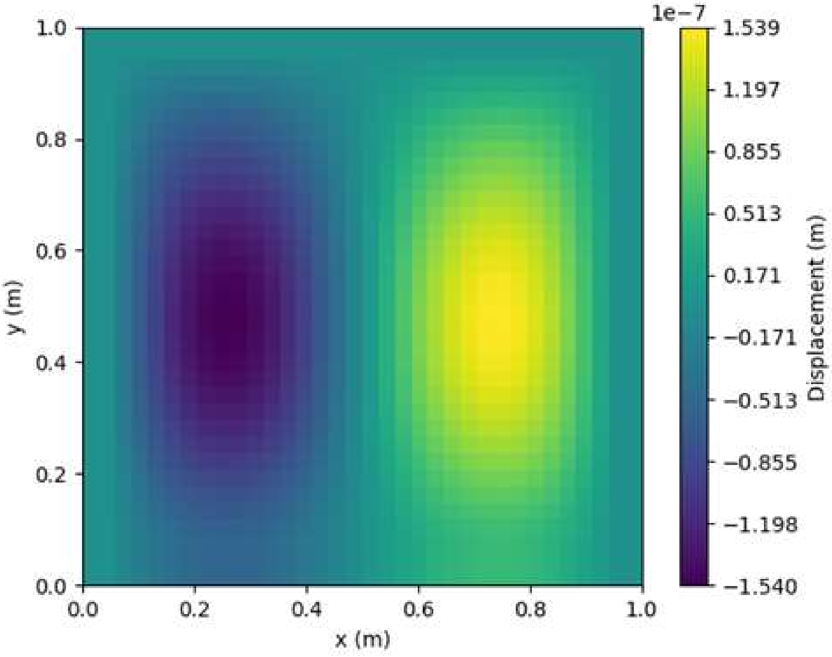

Figure 4.31 Axial displacement in x direction of lower plate (u2)

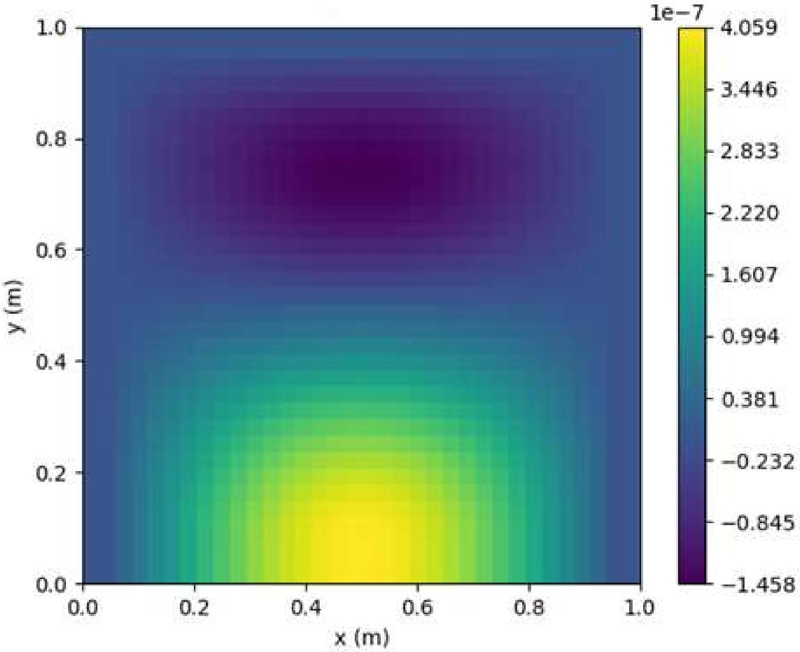

Figure 4.32 Axial displacement in y direction of lower plate (v2)

The x-displacements (u2) and y-displacements (v2) observed in the lower glass layer exhibit a spatial distribution pattern similar to that of the upper glass layer. Specifically, the u2 displacement variations are predominantly aligned along the x-direction, while the v2 displacements are primarily distributed along the y-direction.

Similar to Case 3, the in-plane displacement distributions of the upper and lower glass layers exhibit a high degree of symmetry with respect to z axis. At a corresponding point on the 2D plane, the in-plane displacements of the two layers exhibit similar magnitudes but opposite directions, indicating mirrored deformation behavior across the laminate.

For all in-plane displacement components—including u1, v1 (upper layer) and u2, v2 (lower layer)—their magnitudes are negligible when compared to the transverse (out-of-plane) displacements observed under the same loading conditions.

This aligns with established findings in prior studies [19] [24], where transverse deformations consistently dominate the structural response of similar laminated glass systems. The minimal in-plane displacements again can be attributed to the high in-plane stiffness of the glass layers, which restricts deformation along the x- and y-axes, while the comparatively lower out-of-plane stiffness allows for more pronounced deflections in the z-direction. Furthermore, the clamped boundary conditions, which typically constrain in-plane motion at the edges, further suppress the u and v displacements. This reinforces the expected deformation pattern, where transverse displacements dominate the overall mechanical response in this case.

4.4.1 Comparison with Theoretical Limits (Monolithic/Layered)

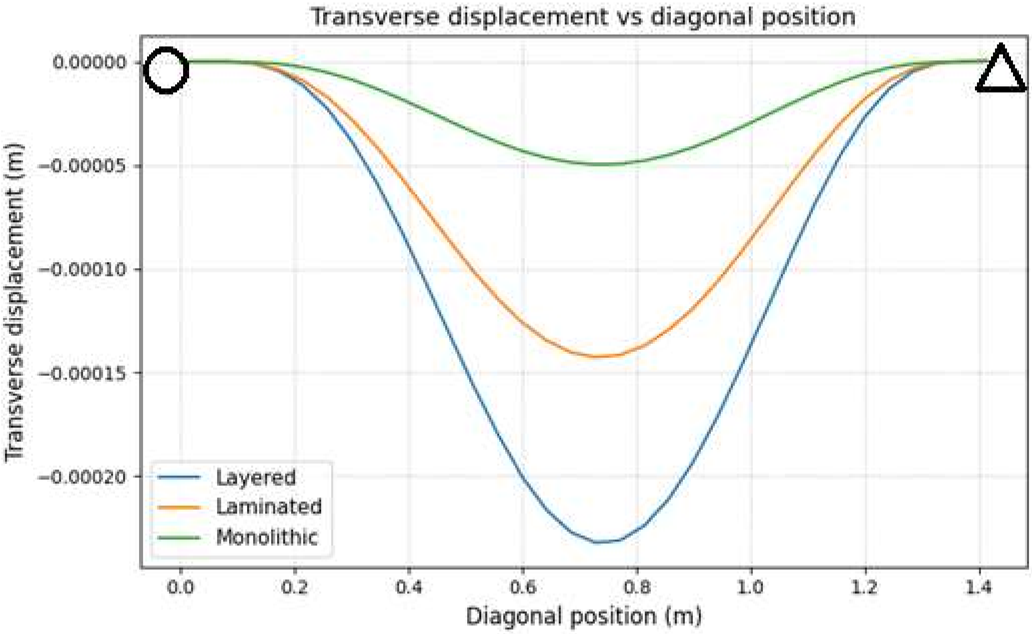

Figure 4.33 Comparison of transverse displacements along diagonal line with theoretical limits

The first theoretical limit corresponds to monolithic glass, defined as a single-layer glass plate of full thickness without any interlayer adhesive. The second theoretical limit represents layered glass, which consists of multiple glass layers identical to those in laminated glass but with zero shear stiffness in the interlayer. In this layered limit, the glass layers are free to slide relative to one another without shear resistance. Laminated glass, in theory, exhibits behavior between these two extremes. Its specific response—whether closer to the monolithic or layered limit—depends on the shear stiffness of the polymer interlayer material.

In the present analysis and corresponding Case 3 (Figure 4.33), again the deformation of laminated glass falls in between these two theoretical limits. The circle and triangle symbols in Figure 4.33 show the same points in Figure 4.27. While all cases (monolithic, layered, and laminated) exhibit qualitatively similar transverse displacement shapes, the magnitudes differ significantly due to their distinct stiffness characteristics. These results align with theoretical expectations: laminated glass, by virtue of its finite interlayer shear stiffness, demonstrates greater rigidity than the layered limit but remains less stiff than the monolithic case, as the polymer interlayer cannot match the shear stiffness.

4.4.2 Stress Results

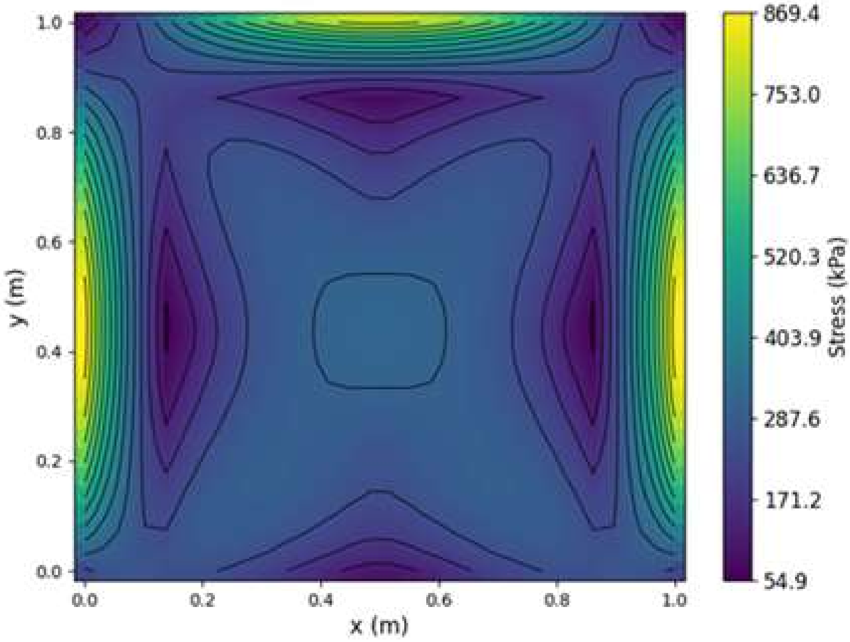

Figure 4.34 First principal stress (σ1) in upper layer

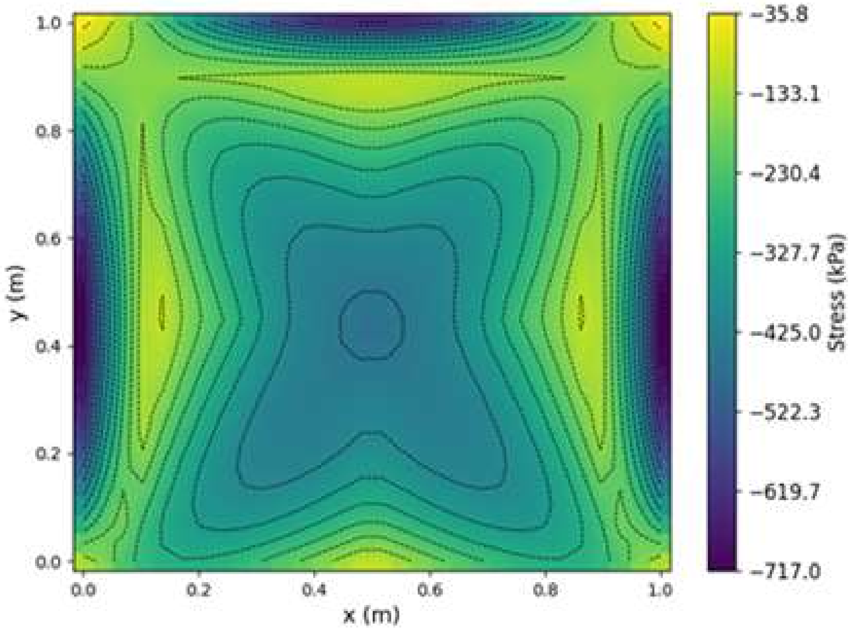

Figure 4.35 Second principal stress (σ2) in upper layer

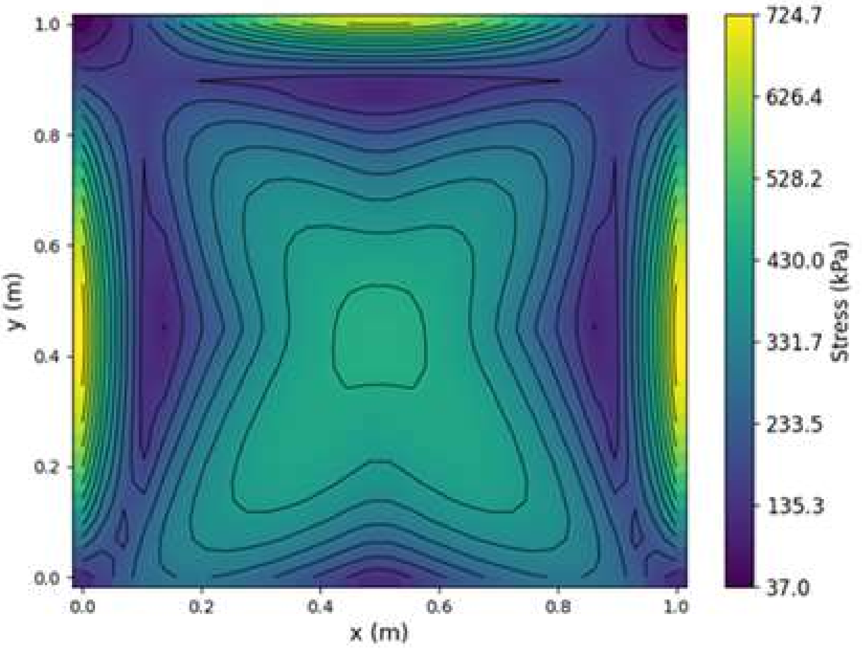

Figure 4.36 First principal stress (σ1) in lower layer

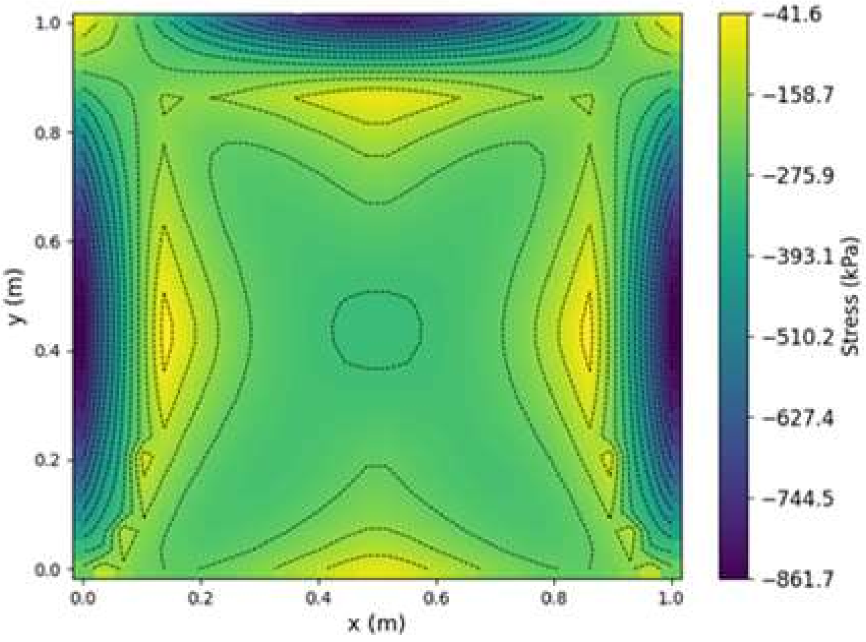

Figure 4.37 Second principal stress (σ2) in lower layer

Figure 4.34, Figure 4.35, Figure 4.36 and Figure 4.37 illustrate the first and second principal stresses for Case 3, shown separately for the upper and lower glass layers. In both layers, the principal stresses reach their maximum values near the clamped edges. This aligns with theoretical expectations, as clamped edges impose stricter displacement constraints, leading to higher local stiffness compared to simply supported edges. The points of minimum absolute principal stresses typically occur slightly inward from the clamped boundaries, in close proximity to the regions of maximum absolute stress. For Case 3, the sign of a given principal stress remains consistent throughout each individual layer, indicating no sign reversal within the layer.

The principal stress distributions between the upper and lower layers are not perfectly symmetric. This asymmetry arises because the principal stresses are influenced by the combined effect of membrane and bending stresses. If bending were the sole contributor, the stress distributions would be symmetric with respect to the interlayer plane. These results show similarities with Case 2.

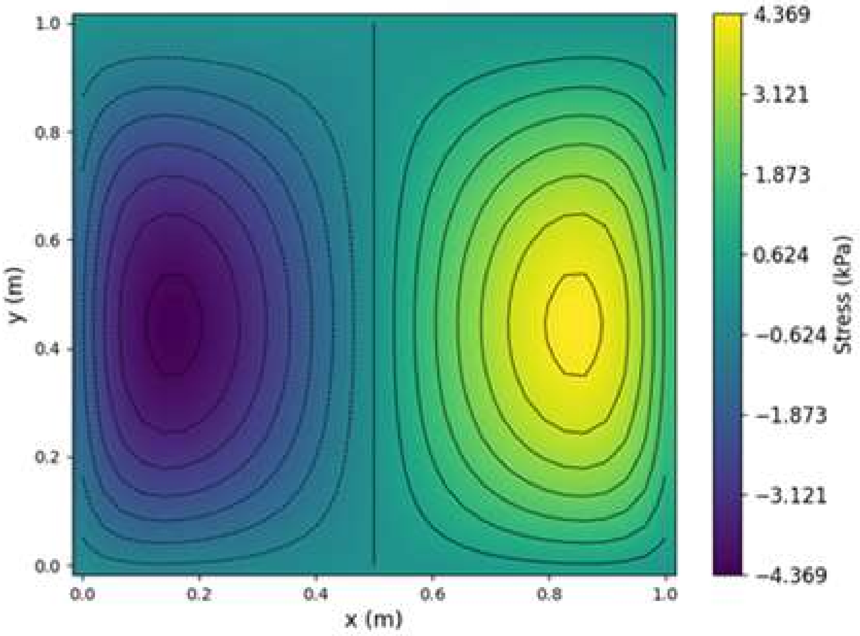

Figure 4.38 Distribution of transverse shear stress τ_{xz} in the interlayer

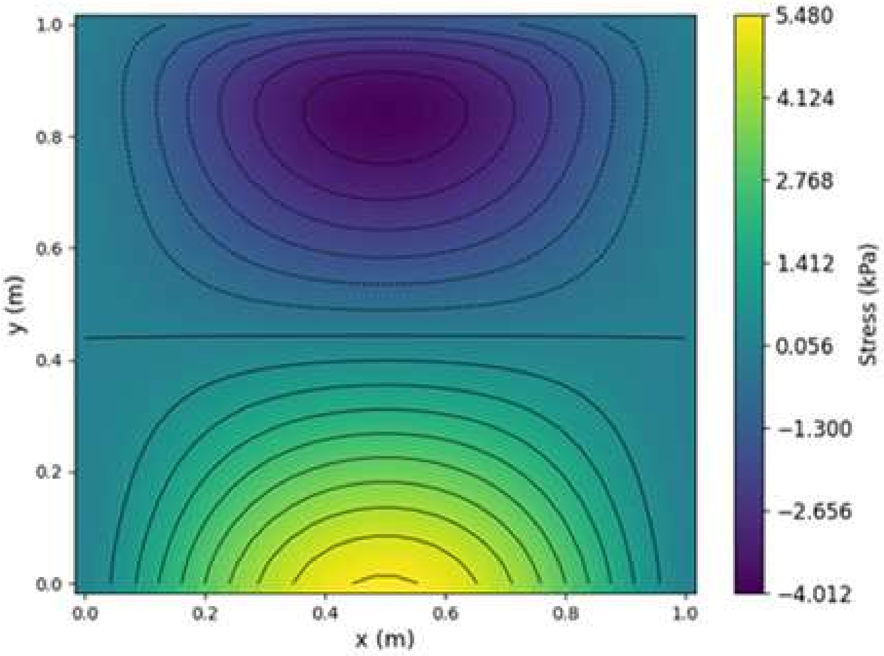

Figure 4.39 Distribution of transverse shear stress τ_{yz} in the interlayer

The transverse shear stress distributions within the interlayer are presented in Figure 4.38 and Figure 4.39. Similar to Case 2, the shear stress on the xz-plane (τ_{xz}) primarily varies along the x-direction, whereas the shear stress on the yz-plane (τ_{yz}) exhibits stronger variation along the y-direction compared to the x-direction. Unlike the principal stresses in the glass layers—which are highest near the clamped edges in Case 3—the interlayer shear stresses are more pronounced near the simply supported edges. Notably, for both τ_{xz} and τ_{yz}, the shear stress values drop to zero at the mid-plane of the interlayer when viewed in the out-of-plane (z) direction.

4.4.3 Convergence of transverse displacement for interlayer thickness

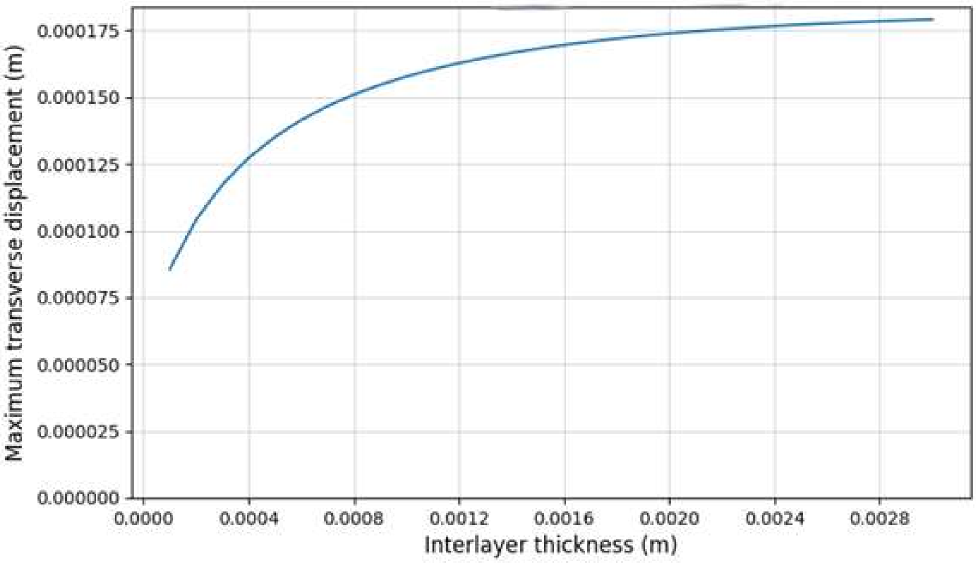

Figure 4.40 Case-3 interlayer thickness versus maximum transverse displacement

In Figure 4.40, increasing the glass layer thickness has a direct positive effect on the overall stiffness of the laminated plate, which aligns with the physical nature of the problem. However, increasing the interlayer adhesive thickness while keeping other parameters constant reduces stiffness and increases the transverse displacement of the plate. To explore this phenomenon, the interlayer thickness is varied over a wide range. Similar to Case 2, the results show that as the interlayer thickness increases, the maximum transverse displacement also increases, eventually converging after a certain point. The converged “maximum transverse displacement” value (around 0.175 mm) is lower for Case 3, compared to Case 2.

4.5 Case 4: Unsymmetrical Clamped - S.S. - S.S. - S.S. Edges

In this configuration, the square plate is constrained by a combination of boundary conditions where three edges are simply supported while the remaining upper edge is clamped. To elaborate further, in Figure 4.41, simply supported boundary conditions—applied to the bottom, left and right edges— only restrict transverse displacement. In contrast, the top edge of the plate is assigned clamped boundary conditions, which enforce complete fixity along this boundary.

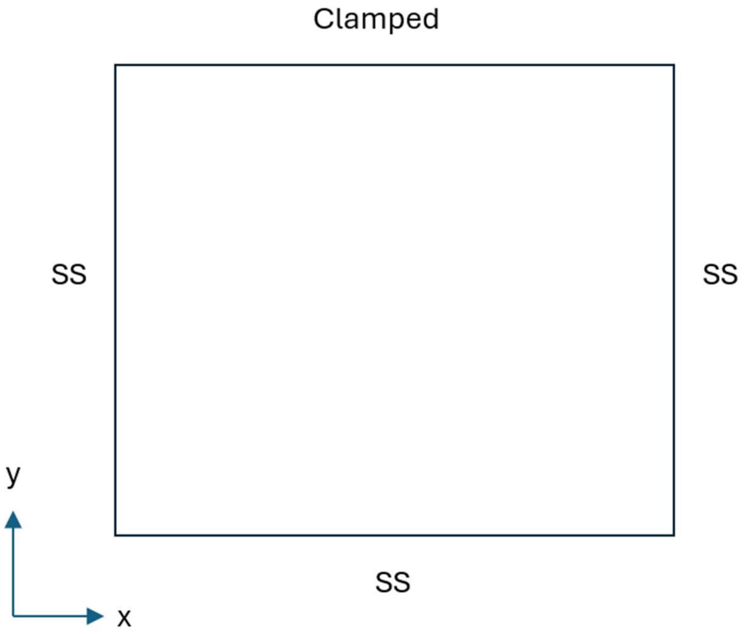

Figure 4.41 Case 4 boundary conditions for the plate

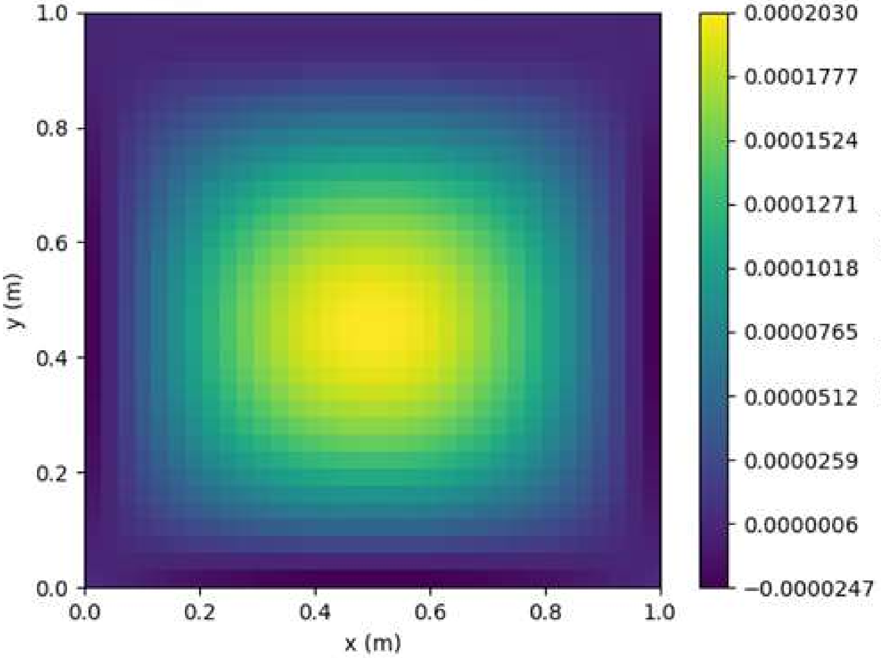

Figure 4.42 Transverse displacement of the plate

Like in Case 1 and Case 2, the transverse displacements are the dominant displacements for transverse pressure loading. Thus again, those displacements are compared with the equivalent FEM model results. In the FEM model below, the boundary conditions and displacement extraction path are similarly specified. Also, the deformation shapes can be observed.

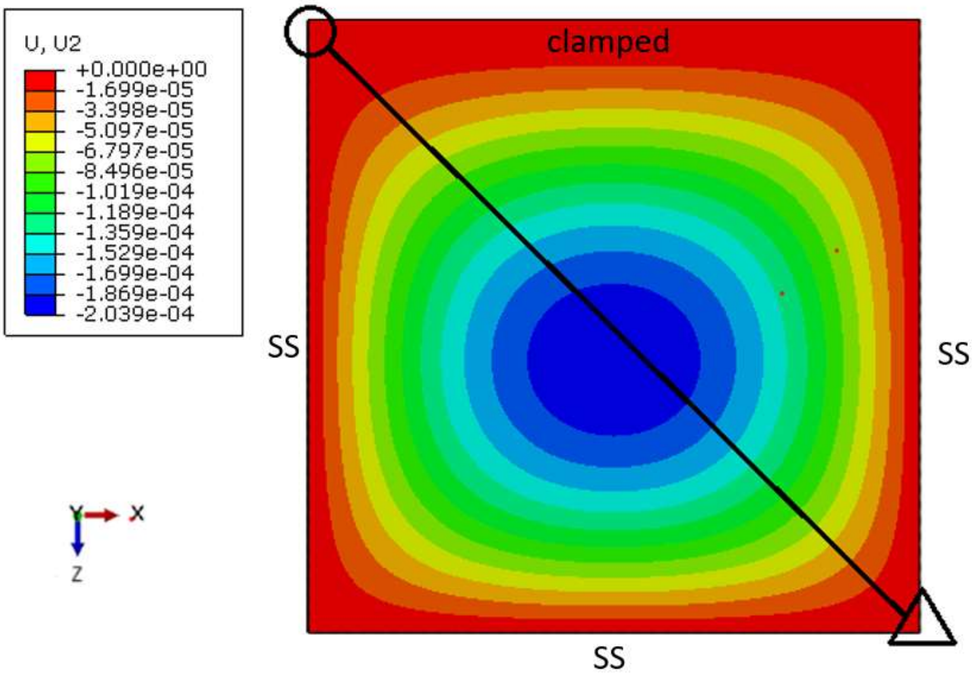

Figure 4.43 Transverse displacement results of FEM analysis

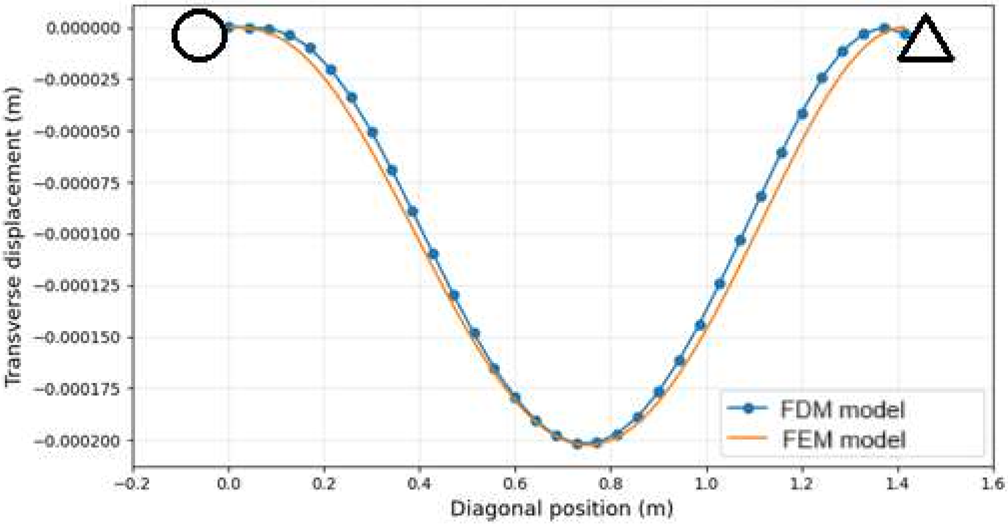

Figure 4.44 Case-4 Transverse displacements from mathematical model and FEM analysis

In Figure 4.44, the FEM displacements are extracted along the diagonal in Figure 4.43, starting at the clamped- S.S. edge (marked with a circle) and ending at the S.S.- S.S. edge (marked with a triangle). And the Finite Difference Method (FDM) model displacements are extracted along top-left and bottom-right corners of Figure 4.42, starting at top-left corner. The circle and triangle symbols show the same points in Figure 4.43.

Similar to the previous cases, the computational results obtained from both the Finite Difference Method (FDM) and Finite Element Method (FEM) models again demonstrate strong agreement, with nearly indistinguishable deformation profiles and closely matching quantitative values. Specifically, the spatial distribution of displacements, as well as the magnitude of local strain concentrations, exhibit a high degree of correlation between the two numerical approaches.

A key observation is the systematic shift of the maximum transverse displacement's lowest points away from the clamped edge region compared to the symmetrical solution, which has a maximum displacement point in the middle of the plate. Similar with previous cases, this trend arises due to the inherent mechanical contrast between boundary conditions: simply supported supports, which allow rotational freedom, exhibit significantly greater deformation than clamped edges, which fully restrain both rotations and translations. Consequently, deformation localizes preferentially near the less constrained simply supported edges similar with Case 2 and Case 3 —again as in plate mechanics literature [14]. Again, the consistency between FDM and FEM predictions not only reinforces confidence in the FDM implementation but also aligns with first-principles expectations for thin-plate deformation under mixed boundary conditions.

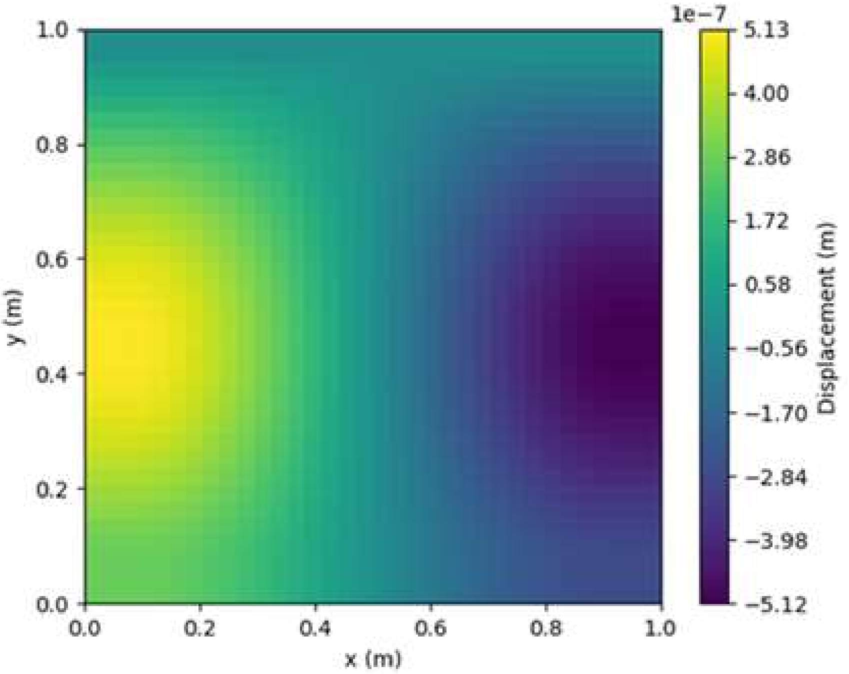

Figure 4.45 Axial displacement in x direction of upper plate (u1)

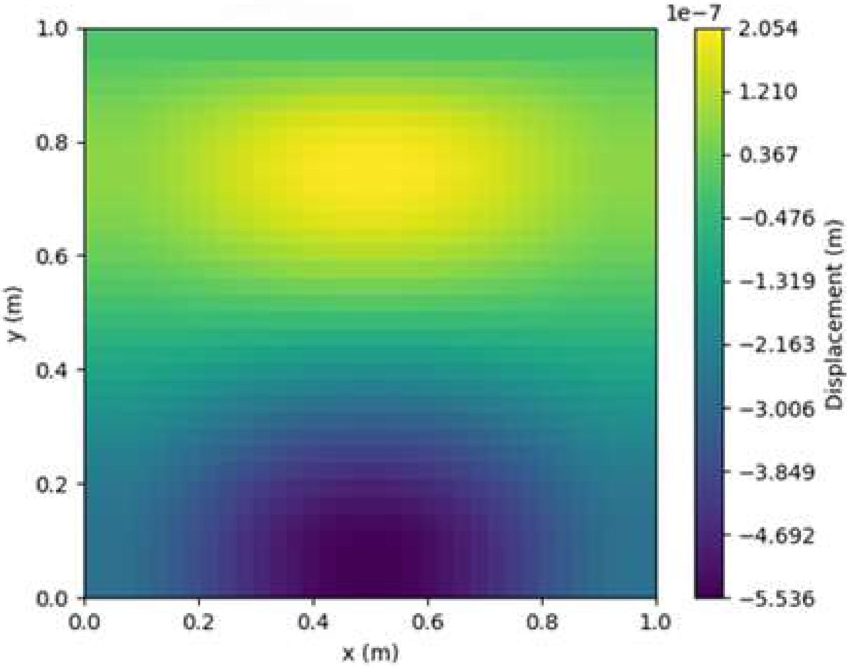

Figure 4.46 Axial displacement in x direction of upper plate (v1)

Similar to Case 2 and Case 3; when analyzing the in-plane x-displacements (u1) and y-displacements (v1) for the upper glass layer in

Figure 4.45 and Figure 4.46, it is apparent that their spatial distributions are oriented orthogonally within the plane. The u-displacements, representing in-plane motion along the x-axis, show a dominant variation parallel to the x-direction, while the v-displacements, corresponding to in-plane motion along the y-axis, are primarily distributed parallel along the y-direction. Additionally, the deformation behavior at the edges aligns with theoretical expectations: clamped boundary conditions enforce zero in-plane displacements, whereas the simply supported edges allow for non-zero in-plane displacements.

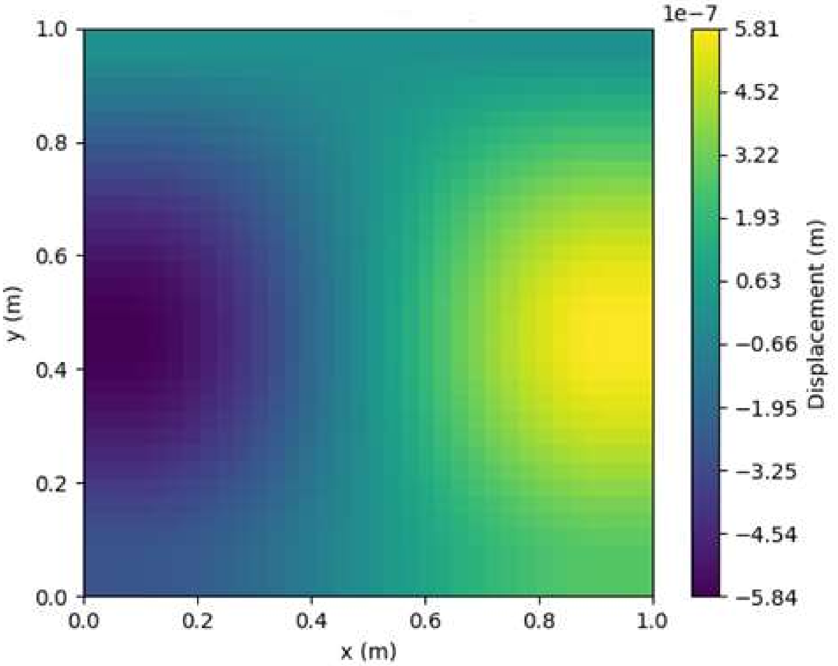

Figure 4.47 Axial displacement in x direction of lower plate (u2)

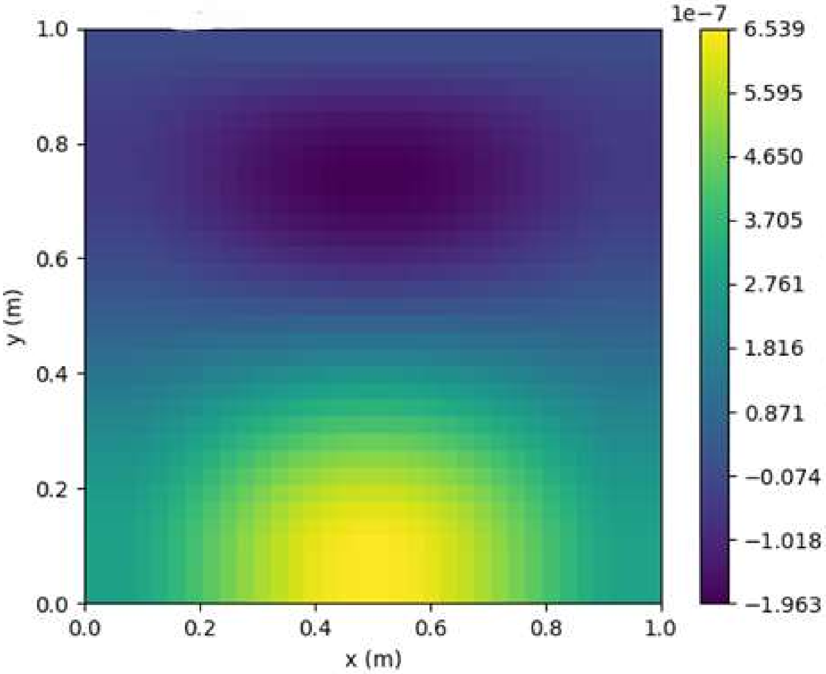

Figure 4.48 Axial displacement in y direction of upper plate (u2)

Similar to Case 2 and Case 3, the x-displacements (u2) and y-displacements (v2) observed in the lower glass layer exhibit a spatial distribution pattern similar to that of the upper glass layer. Specifically, the u2 displacements are predominantly varying along the x-direction, while the v2 displacements are primarily distributed along the y-direction.

The in-plane displacement distributions of the upper and lower glass layers exhibit a high degree of symmetry with respect to z axis (interlayer plane). At a corresponding point on the 2D plane, the in-plane displacements of the two layers exhibit similar magnitudes but opposite directions, indicating mirrored deformation behavior across the laminate.

Similar to Case 2 and Case 3, for all in-plane displacement components—including u1, v1 (upper layer) and u2, v2 (lower layer)—their magnitudes are negligible when compared to the transverse (out-of-plane) displacements observed under the same loading conditions. This aligns with established findings in prior studies [20], where transverse deformations consistently dominate the structural response of similar laminated glass systems. The minimal in-plane displacements can be attributed to the high in-plane stiffness of the glass layers, which restricts deformation along the x- and y-axes, while the comparatively lower out-of-plane stiffness allows for more pronounced deflections in the z-direction. Furthermore, the boundary conditions, which typically constrain in-plane motion at the edges, further suppress u and v displacements, reinforcing the expected deformation hierarchy where transverse displacements govern the overall mechanical behavior.

4.5.1 Comparison with Theoretical Limits (Monolithic/Layered)

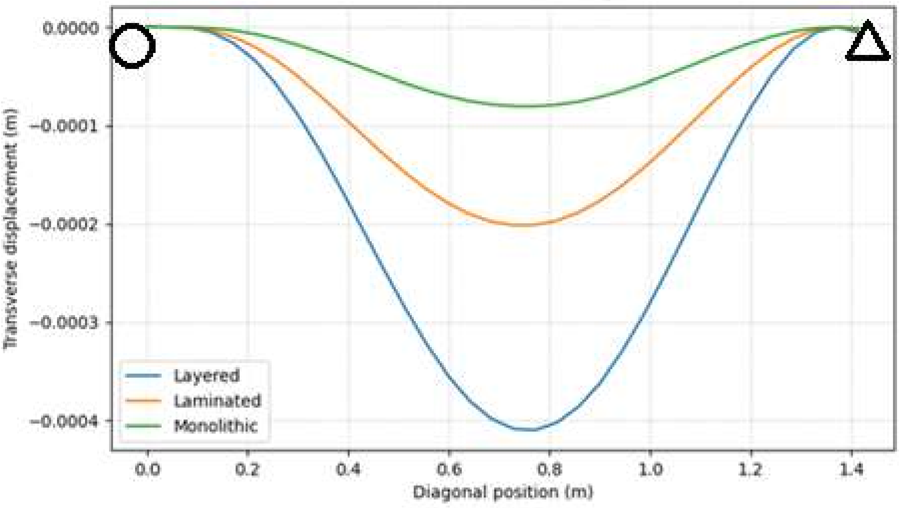

Figure 4.49 Comparison of transverse displacements along diagonal line with theoretical limits

Similar to Case 2 and Case 3, the first theoretical limit corresponds to monolithic glass, the second theoretical limit represents layered glass. In this layered limit, the glass layers are free to slide relative to one another without shear resistance. Laminated glass, in theory, exhibits behavior intermediate between these two extremes. Its specific response—whether closer to the monolithic or layered limit—depends on the shear stiffness of the polymer interlayer material.

In the present analysis and corresponding Case 4 (Figure 4.49), again the deformation of laminated glass falls between these two theoretical limits. The circle and triangle symbols in Figure 4.49 show the same points in Figure 4.43. While all cases (monolithic, layered, and laminated) exhibit qualitatively similar transverse displacement shapes, the magnitudes differ significantly due to their distinct stiffness characteristics. Similar to Case 2 and Case 3, these results align with theoretical expectations: laminated glass, by virtue of its finite interlayer shear stiffness, demonstrates greater rigidity than the layered limit but remains less stiff than the monolithic case, as the polymer interlayer cannot match the shear stiffness.

4.5.2 Stress Results

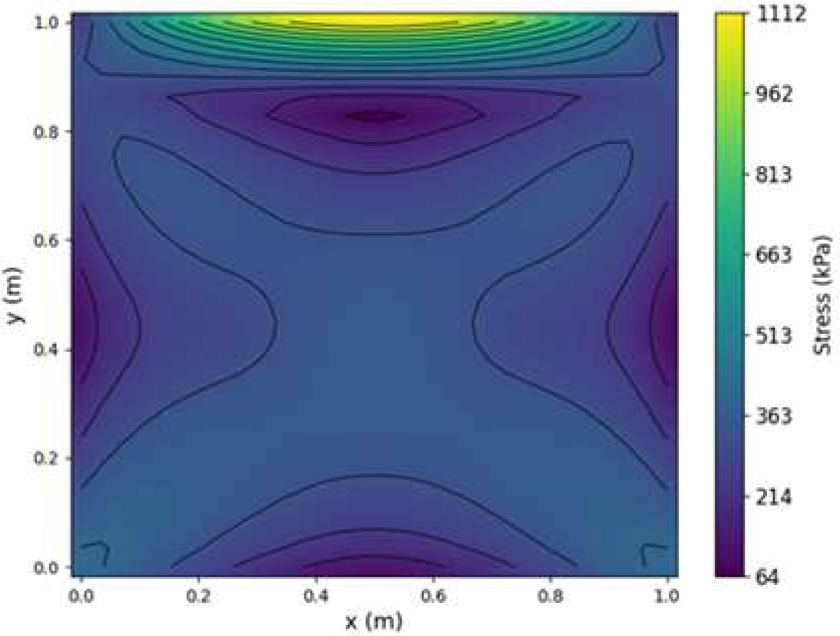

Figure 4.50 First principal stress (σ1) in upper layer

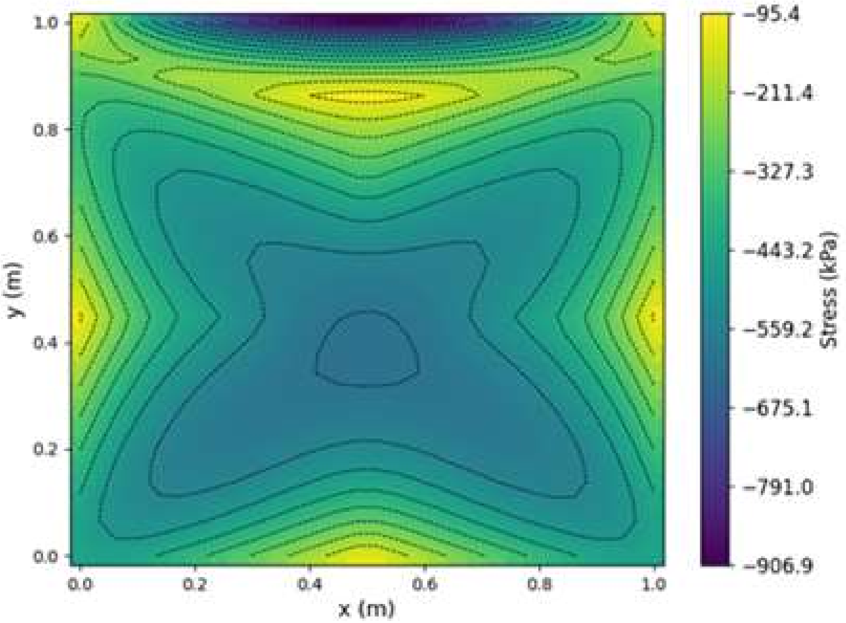

Figure 4.51 Second principal stress (σ2) in upper layer

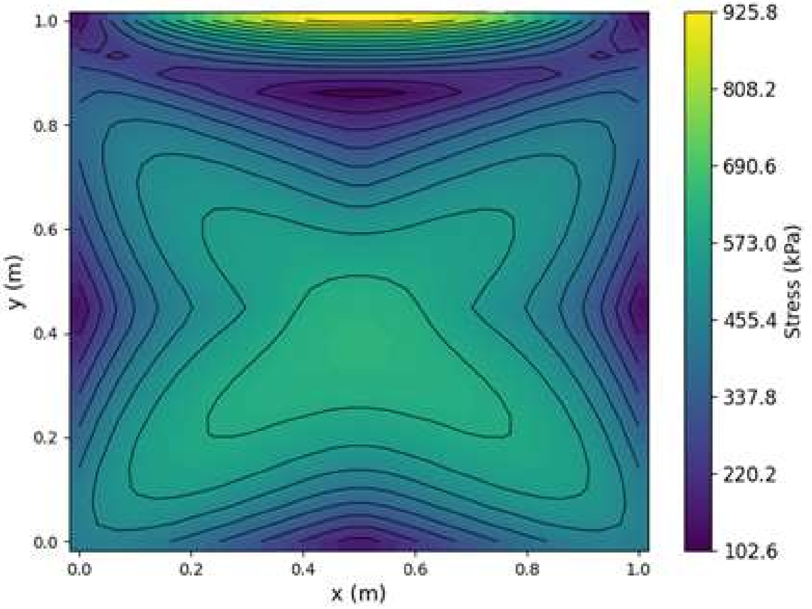

Figure 4.52 First principal stress (σ1) in lower layer

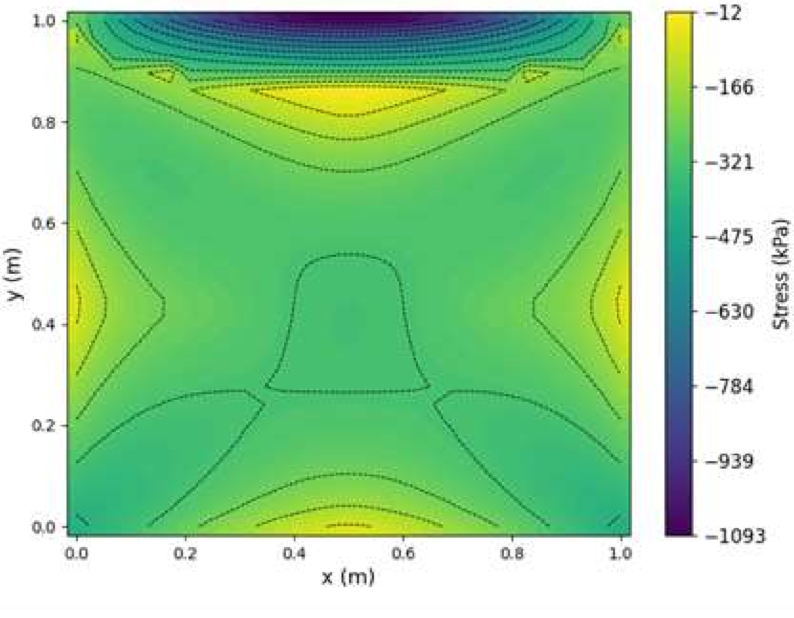

Figure 4.53 Second principal stress (σ2) in lower layer

Figure 4.50, Figure 4.51, Figure 4.52, and Figure 4.53 illustrate the first and second principal stresses for Case 4, shown separately for the upper and lower glass layers. In both layers, the principal stresses reach their maximum values near the clamped edges. This aligns with theoretical expectations, as clamped edges impose stricter displacement constraints, leading to higher local stiffness compared to simply supported edges. The points of minimum absolute principal stresses typically occur slightly inward from the clamped boundaries, in close proximity to the regions of maximum absolute stress. For Case 4, the sign of the given principal stress remains consistent throughout each individual layer, indicating no sign reversal within the layer.

The principal stress distributions between the upper and lower layers are not perfectly symmetric. This asymmetry arises because the principal stresses are influenced by the combined effect of membrane and bending stresses. If bending were the sole contributor, the stress distributions would be symmetric with respect to the interlayer plane. Those results show similarities with Case 2 and Case 3.

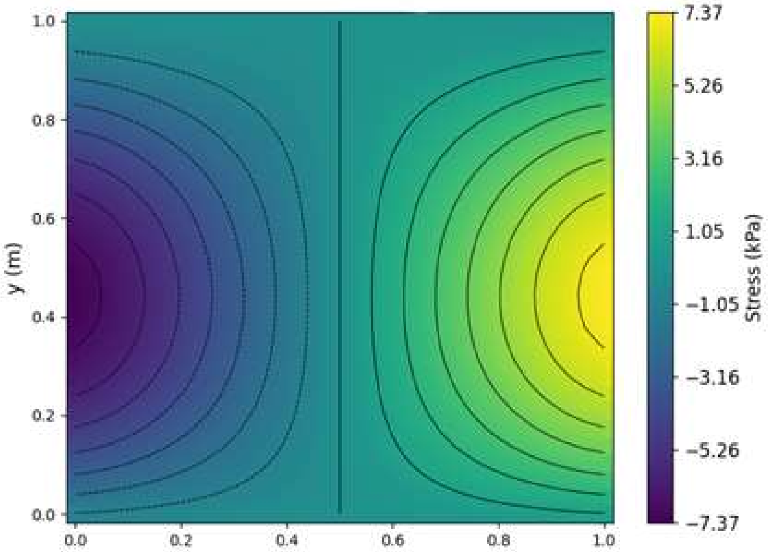

Figure 4.54 Distribution of transverse shear stress τ_{xz} in the interlayer

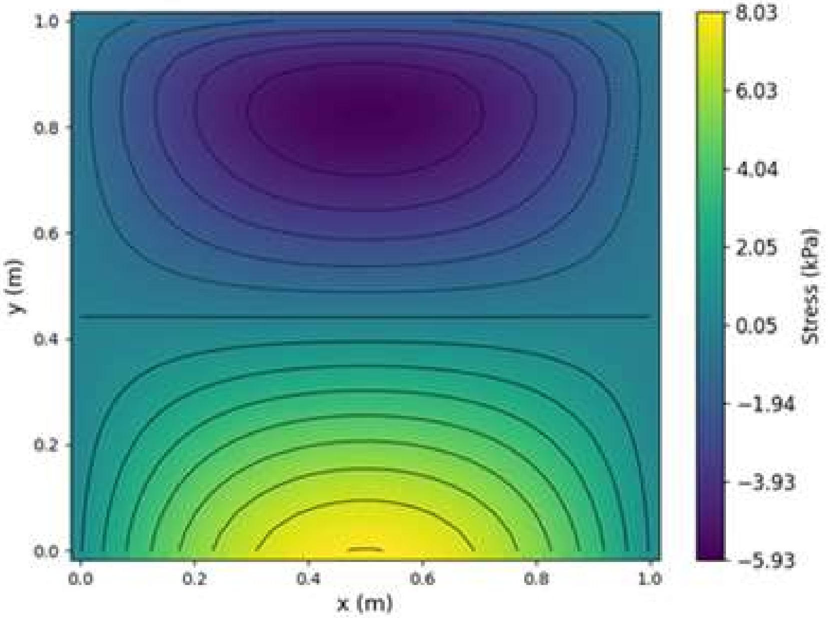

Figure 4.55 Distribution of transverse shear stress τ_{yz} in the interlayer

The transverse shear stress distributions within the interlayer are presented in Figure 4.54 and Figure 4.55. Similar to Case 2, the shear stress on the xz-plane (τ_{xz}) primarily varies along the x-direction, whereas the shear stress on the yz-plane (τ_{yz}) exhibits stronger variation along the y-direction. Unlike the principal stresses in the glass layers—which are highest near the clamped edges in Case 4—the interlayer shear stresses are more pronounced near the simply supported edges again. Notably, for both τ_{xz} and τ_{yz} , the shear stress values drop to zero at the mid-plane of the interlayer when viewed in the out-of-plane (z) direction.

4.5.3 Convergence of transverse displacement for interlayer thickness

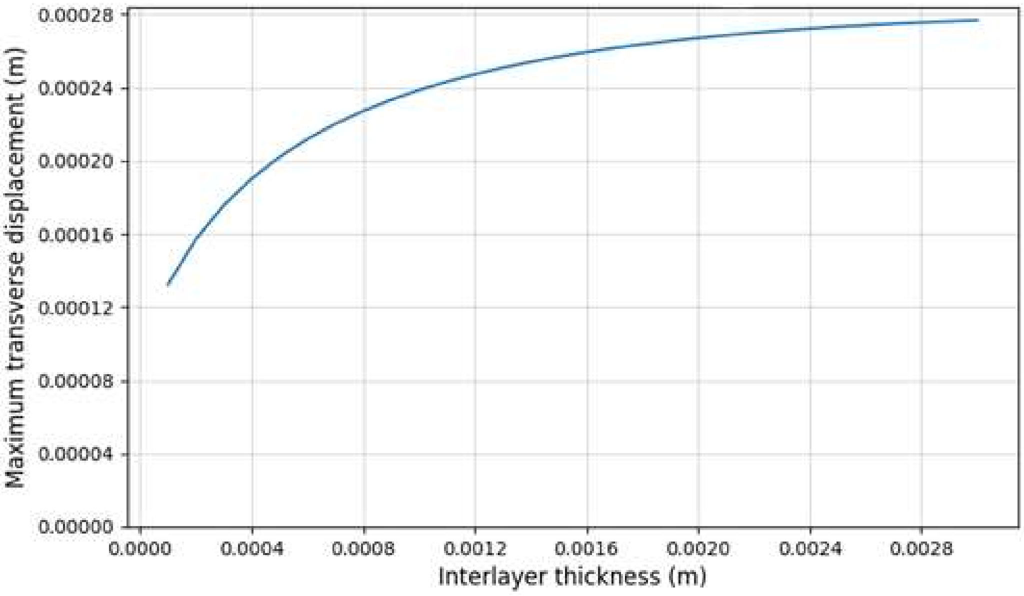

Figure 4.56 Case-4 interlayer thickness versus maximum transverse displacement

Again in Figure 4.56, increasing the glass layer thickness has a direct positive effect on the overall stiffness of the laminated plate, which aligns with the physical nature of the problem. However, increasing the interlayer adhesive thickness while keeping other parameters constant reduces stiffness and increases the transverse displacement of the plate. To explore this phenomenon, the interlayer thickness is varied over a wide range. Similar to Case 1 and Case 2, the results show that as the interlayer thickness increases, the maximum transverse displacement also increases, eventually converging after a certain point. The converged “maximum transverse displacement” value (around 0.28 mm) is higher for Case 4, compared to Case 2 and Case 3.

4.6 Transverse Displacements Comparison

In this section, the transverse displacement distributions of all six cases along the diagonal are compared by plotting them on the same graph (Figure 4.57). A uniform pressure load of 0.2 kPa is applied for all the solutions presented here. The circle and triangle symbols correspond to the same reference points as in the previous cases. For fully clamped or fully simply supported (SS) boundary conditions, however, the choice of these points is not significant.

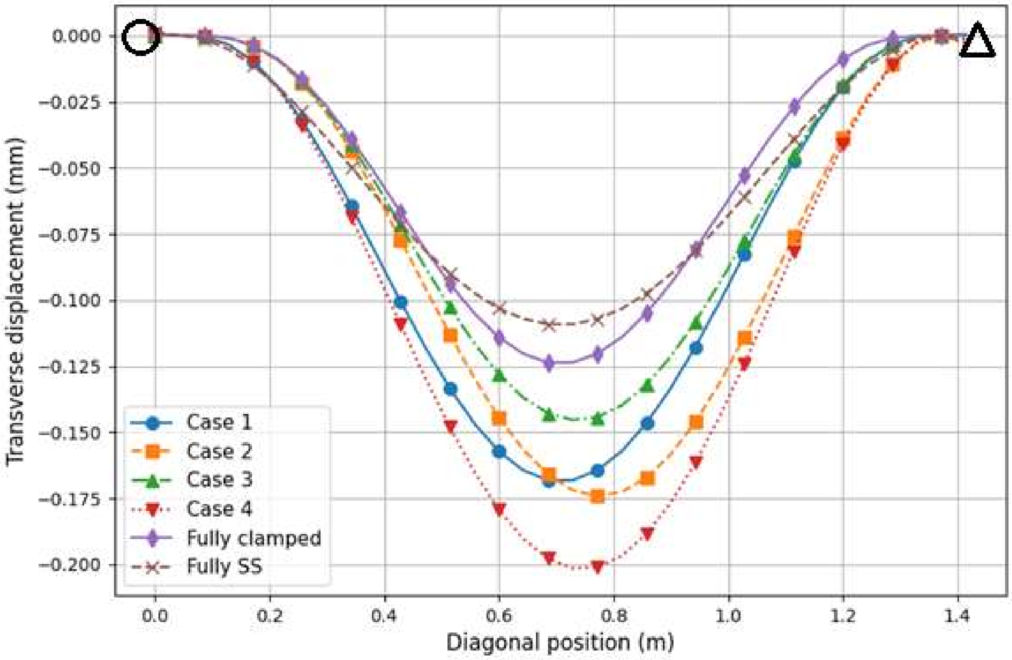

Figure 4.57 Six cases transverse displacement comparison along diagonals

Figure 4.57 shows that the maximum transverse displacement occurs in Case 4 (Three edges simply supported, one edge clamped). Moreover, the fully simply supported (SS) case exhibits the lowest transverse displacement at the mid-span, while the fully clamped case shows the lowest displacement near the edges.

4.7 Critical Stresses

Table 4.1 presents the most critical principal stress values observed for each loading case, highlighting the stress severity across different boundary conditions.

Table 4.1 Maximum and minimum principal stresses for each case

Cases	Maximum first principal stress	Minimum second principal stress
Case 1	1888 kPa	-1877 kPa
Case 2	957 kPa	-945 kPa
Case 3	869 kPa	-861 kPa
Case 4	1115 kPa	-1095 kPa
Fully clamped	888 kPa	-887 kPa
Fully S.S.	865 kPa	-848 kPa

Among all cases, Case 1 produces the largest absolute values of both maximum and minimum principal stresses. For the main cases of interest in this study (the unsymmetrical cases: 2, 3, and 4), Case 4 exhibits the most critical stress state, with both principal stresses reaching their peak magnitudes. This is expected, as the single clamped edge in Case 4 must compensate for the flexibility introduced by the three simply supported edges, resulting in pronounced stress concentrations near the clamped boundary. In contrast, Case 3 shows the lowest stress levels, as three clamped edges effectively restrain the displacements associated with the single simply supported edge.

For the benchmark cases Case 1, fully clamped and fully S.S., Case 1 gives the highest absolute principal stresses, which are also the highest stresses among all six cases. Case 1 was for symmetrical mixed boundary conditions (clamped-S.S.-clamped-S.S. in order).

Table 4.2 summarizes the absolute maximum values of the transverse shear stresses, τ_{xz} and τ_{yz}, across all loading cases. The absolute values are reported because the sign indicates only the direction of the shear stress, not its magnitude or criticality.

Table 4.2 Absolute maximum transverse shear stress values for each case

Cases	τ_{xz} absolute maximum value	τ_{yz} absolute maximum value
Case 1	22.9 kPa	19.8 kPa
Case 2	6.76 kPa	6.76 kPa
Case 3	4.37 kPa	5.48 kPa
Case 4	7.39 kPa	8.04 kPa
Fully clamped	2.45 kPa	2.45 kPa
Fully S.S.	6.94 kPa	6.94 kPa

In Table 4.2, among the unsymmetrical cases, the maximum absolute interlayer shear stresses are again the highest for Case 4 and the lowest for Case 3. This trend is similar to that of the extreme principal stress values, which is expected: in Case 4, the single clamped edge restricts displacements, while the other three edges are simply supported. As a result, most of the reaction load is concentrated along the clamped edge.

Similarly, for the benchmark cases (Case 1, fully clamped, and fully simply supported), Case 1 produces the highest absolute shear stresses, which are also the largest shear stresses among all six cases. Case 1 corresponds to symmetrical mixed boundary conditions (clamped–S.S.–clamped–S.S. in order).

4.8 Computational Performance

A local personal computer (PC) is used to perform both FEM and FDM analysis runs. The specifications of the computer are provided on Table 4.3.

Table 4.3 Computational environment specifications

OS Name	Microsoft Windows 11 Pro
Processor	12th Gen Intel(R) Core (TM) i5-12450H, 2000 Mhz, 8 Core(s), 12 Logical Processor(s)
System Type	x64-based PC
Installed Physical Memory (RAM)	16.0 GB
Available Virtual Memory	27.8 GB

Table 4.4 Run-time comparison of the developed FDM model and FEM analysis

Cases	Model run time (seconds)	FEM run time (seconds)
Case 2	24.7	2821.4
Case 3	9.5	2487.3
Case 4	10.2	3741.0

The primary advantage of the model lies in its computational efficiency. As shown in Table 4.4, the FDM model is over 100 times faster than the FEM model, completing the analysis in only about 1% of the time required. In addition, the setup process is greatly simplified, as the FDM model requires only parameter inputs without further preprocessing; all configurations are automatically handled within the code.

Table 4.5 Memory requirements for the developed model and FEM model

	Required memory	Required memory in FEM model
Similar values for all cases	141 MB	2.17 GB (Minimum) 15.9 GB (increased up to analysis estimates locally)

The memory efficiency improvements of the FDM approach are equally noteworthy. Beyond computational speed advantages, the model demonstrates superior performance in terms of RAM requirements. For a representative case in Table 4.5 —Case 3, which involves three edges clamped and single simply supported edge—the memory savings are particularly significant.

The comparative analysis reveals striking differences in resource allocation: while the conventional FEM implementation demands 2.17 GB of working memory, our FDM-based solution accomplishes the same simulation task using only 141 MB of RAM allocation. This translates to the FDM model requiring just 6.5% of the memory resources needed by the FEM approach, representing nearly a 94% reduction in memory footprint.

4.9 Nonlinear Effect in the Solution

Given the incorporation of nonlinear strain formulations in the model, the system's response is expected to exhibit progressively non-linear behavior with increasing load magnitude. This characteristic nonlinearity manifests most clearly in the relationship between applied pressure and maximum displacement. To systematically demonstrate this effect, a series of numerical solutions were computed and analyzed for Case 3 (as defined in Section 4.2), spanning a range of pressure loads from 0.2 kPa to 8 kPa.

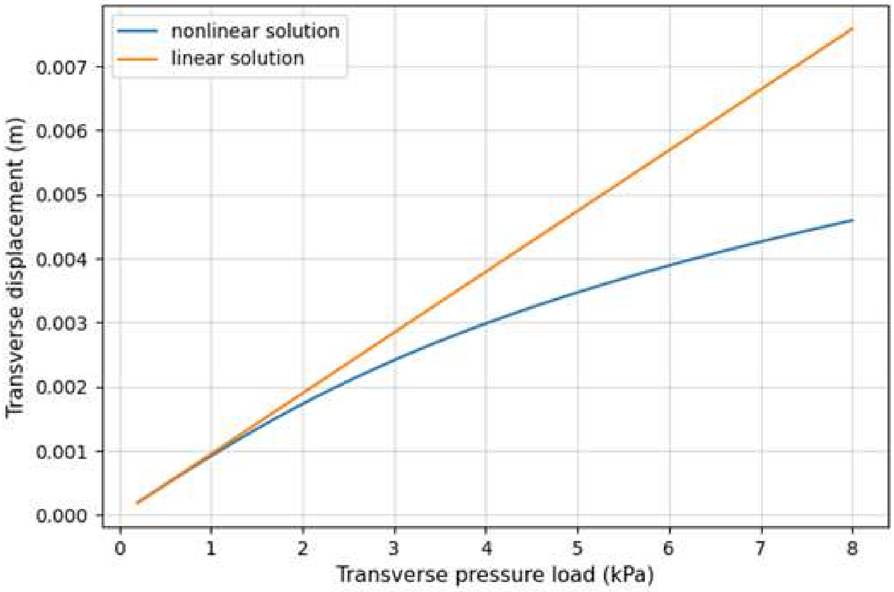

Figure 4.58 Maximum transverse displacements: Nonlinear model solution and linear solution

For comparative purposes, a linear solution is calculated by removing all the nonlinear terms in the transverse and in-plane displacement equations, specifically from the right-hand side parts of Equations (3.23), (3.24), (3.25), (3.26) and (3.27).

The linearized model establishes a reference baseline to systemically evaluate the nonlinear effects inherent in the full FDM model.

The results, presented in Figure 4.58, reveal several important observations:

1. The divergence between linear and nonlinear solutions becomes increasingly pronounced at higher loading levels.
2. The maximum discrepancy reaches approximately 30% at the upper limit of the loading range (8 kPa).
3. The deviation follows a characteristic pattern where nonlinear effects accumulate progressively rather than appearing abruptly.

This 30% difference at operational-scale loading conditions demonstrates the critical importance of incorporating nonlinear strain formulations when modeling such systems. The conventional linear approach would significantly underpredict displacements by neglecting these cumulative nonlinear effects, potentially leading to unconservative designs in engineering applications. The results quantitatively validate that our nonlinear FDM implementation successfully captures these essential mechanical behaviors that linearized models cannot represent.

4.10 Optimum number of divisions and mesh convergence

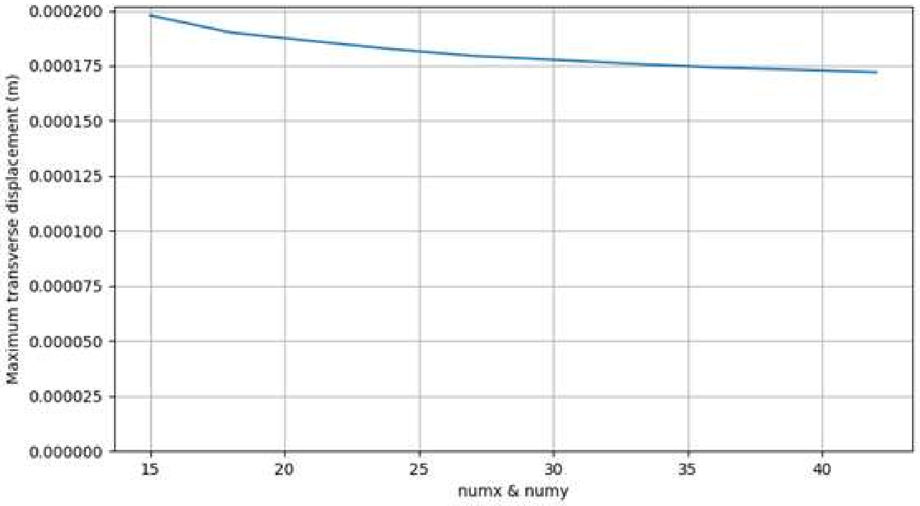

Figure 4.59 Convergence of the solution with varying edge divisions (numx and numy)

As it is seen in Figure 4.59, the number of divisions (mesh density) are denoted as "numx" for the number of divisions in x-direction and "numy" for the number of divisions in y-direction.

Those number of divisions was evaluated over a range of 15 to 40 intervals. In the figure above, the convergence of the number of mesh divisions along both x and y can be seen. X and Y mesh divisions (numx and numy) are taken as a single parameter, and solutions are taken for each value. Maximum transverse displacement values for those numbers of divisions are plotted to see if the solution has converged. As it is increased above 30 divisions, the solution seems to converge and not change by much. Similar convergence behaviors are obtained for other cases as well. That is why the optimal number of divisions for our model is taken as "30" in both x and y directions.

For even better accuracy, a mesh density of 40 can be used. This does not make analysis much slower; the runs will still be much faster compared to FEM analysis, but the error compared to FEM will get much smaller. The error values change for each boundary condition so users can try to increase the grid points if they are not satisfied with the results. Nevertheless, it is not expected to increase the grid points above 40.

CHAPTER 5

CONCLUSION

5.1 Conclusive Remarks

This thesis presents a nonlinear numerical model for analyzing laminated glass plates under complex boundary conditions using the Finite Difference Method (FDM). The model incorporates geometric nonlinearity, multilayer behavior, and mixed support conditions, enabling accurate predictions of displacements and stress distributions. A significant aspect of this study is its capability to simulate realistic engineering conditions without relying on symmetry assumptions, which are commonly used to simplify the analysis domain in previous works.

The formulation of the model draws upon a combination of energy and variational methods, following the foundational work of Aşık et al. [10] [11] [20] [24] [35]. The primary technical contributions include the incorporation of mixed boundary conditions and the extension of the solution framework to handle unsymmetrical edge configurations, thereby offering a more generalized solution compared to previous studies. The model was tested on three representative boundary condition scenarios:

- Case 2: Two adjacent edges are clamped, and the remaining two are simply supported.
- Case 3: Three edges are clamped, and one edge is simply supported.
- Case 4: Three edges are simply supported, and one edge is clamped.

These cases represent practical configurations found in real structures and allow for the evaluation of the model under a wide range of stiffness variations along the plate boundaries.

While earlier models by Vallabhan, Aşık, and Dural mainly addressed symmetric boundary conditions, the present work extends the formulation to accommodate realistic engineering applications where support conditions vary significantly across the structure. This enables the full-plate domain to be modeled, allowing for more comprehensive investigation of edge effects and stress localizations.

The proposed model has been successfully verified against finite element simulations performed in Abaqus. The comparison demonstrates strong agreement between FDM and FEM in terms of both transverse displacements and in-plane stress distributions. Moreover, the FDM implementation shows advantages in terms of memory usage and computational efficiency, especially in structured geometries. These outcomes not only validate the mathematical formulation but also emphasize the practicality of the model in structural design, optimization, and safety assessment of laminated glass systems.

- Unlike the Fortran-based implementations commonly found in previous literature [36] [37], the proposed model is developed using the Python programming language. This transition is expected to enhance the model’s accessibility and usability in future engineering applications, given Python's wider adoption and greater ease of use compared to Fortran.
- The model is observed to be sensitive to mesh density, which is expected given the inherent characteristics of the Finite Difference Method. Converged results are obtained using a 30×30 mesh for a 1 m × 1 m laminated glass plate, as described in Section 3.3. For rectangular plates with unequal edge lengths, the optimal number of mesh divisions may vary along each axis. Therefore, separate mesh sensitivity studies are recommended for each distinct geometry to ensure accuracy.
- For all three cases, the results show good agreement with those obtained from the Finite Element Method (FEM) model. The comparison reveals a strong correlation, showing discrepancies of less than 6% in transverse displacement values and highly similar displacement shapes. These findings support the validity of the proposed model for future applications.

- In all three cases, the boundary conditions consisted of mixed clamped and simply supported edges, result in unsymmetrical configurations. As intuitively expected, the points of maximum displacement consistently shift toward the simply supported edges in each case.
- The effect of nonlinearity is clearly observed, with differences in maximum displacements reaching up to 30% as the applied load was progressively increased (see Section 4.9). This result highlights the significant influence of nonlinear behavior on the structural response under increasing load levels.
- The principal stresses of both glass layers and the transverse shear stresses within the interlayer are calculated. Among the three boundary condition cases, Case 4 consistently exhibits the most critical stress levels. It showed the highest first principal stresses in the glass layers, the greatest transverse shear stresses in the interlayer, and the lowest (most critical in compression) second principal stress values. This outcome is logical, as in Case 4, the flexibility allowed by three simply supported edges is constrained by a single clamped edge, leading to significant stress concentrations.
- Numerical experiments are conducted to investigate the effect of interlayer adhesive thickness. As the interlayer thickness increases, the maximum transverse displacement also increases up to a certain point, beyond which the maximum transverse displacement results converge (see Section 4.3.3).
- Compared to the equivalent FEM model developed in this study, the FDM model significantly reduces computing time.
- Additionally, this model demonstrates a significant reduction in memory usage compared to the benchmark FEM model (Section 4.8).
- The results from all three cases remain within the established theoretical bounds for both monolithic and layered glass (Figure 4.17, Figure 4.33 and Figure 4.49).

In conclusion, this study introduces a novel finite difference-based model for analyzing laminated glass plates, incorporating nonlinear formulations to address mixed and unsymmetrical boundary conditions. The proposed approach demonstrates substantial advantages over conventional FEM methods, including faster computation, streamlined setup, and reduced memory demands.

These characteristics make the model especially valuable for engineers who need efficient and accurate analysis of laminated glass structures under real-world constraints. It eliminates the computational overhead of full 3D solid models while preserving fidelity near clamped or mixed supports — a critical requirement in aerospace glazing, building glass structures, and layered photovoltaic panels.

5.2 Potential Applications

The model developed in this thesis has a wide range of potential applications, including laminated architectural glass, automobile glass, train windows, aircraft canopies, solar panel covers, LCD displays, and many others. The primary requirement for applicability is the presence of two stiff layers bonded by a significantly more compliant adhesive layer. Notably, the model's assumptions are not restricted to any specific material type.

This model extends previous work on laminated glass plates [10] [11] [20] [24] [35] , by generalizing the formulation to accommodate a broad range of boundary condition configurations, including unsymmetrical and mixed boundary conditions along the plate edges.

Due to its significantly reduced computational time and low memory requirements, the model presents considerable advantages for implementation in embedded systems used in aircraft, UAVs, automobiles, trains, and similar platforms. These features make it particularly suitable for real-time structural health monitoring and for supporting critical operational decisions, enabling faster response times while operating on cost-effective and less complex hardware.

5.3 Possible Improvements

In this study, static analysis is performed to determine the displacement, strain, and stress distributions of laterally loaded laminated glass plates. However, the current model can be extended to include time-dependent behavior, enabling dynamic and modal analyses of such structures. These extensions could be validated through vibrational testing or finite element method (FEM) simulations.

Furthermore, a shell formulation can be derived based on the present plate model. Such a shell model would expand the applicability of the method to curved geometries, making it particularly suitable for analyzing laminated aircraft canopies, curved train windows, and similar components. Previous work by Dural [37] has investigated laminated glass shells, providing a foundation for further exploration in this direction.

Additionally, extending the model to cover various geometries, such as laminated glass beams, and adapting the formulation accordingly would enable the analysis and validation of beam-type laminated glass components. In such studies, a transition from plate-like to beam-like behavior is expected as the slenderness ratio exceeds a certain threshold.

While FEM-based validation is carried out in this thesis for specific configurations, further experimental investigations could provide additional verification for a broader range of applications and enhance the model's credibility in practical engineering scenarios.

Using the proposed FDM-based model, delamination analysis of laminated glass plates can be performed under any combination of mixed boundary conditions—

whether symmetrical or unsymmetrical—similar to the approach taken by Dural [26] [27]. This capability allows the model to account for potential manufacturing defects, such as interlayer separation, which are critical in evaluating the structural integrity and durability of laminated glass components.

In addition, future developments may include incorporating temperature-dependent viscoelastic properties, multi-layered systems, or coupling with optimization algorithms for structural health monitoring and design refinement.

These findings not only validate the model's robustness but also position it as a promising tool for future research in optimization, delamination detection, and advanced material integration in structural glass systems.

REFERENCES

[1] (2025, August 5). Laminated Glass. Glass Academy. Glass Academy. http://glass-academy.com/laminated-glass/

[2] Hals, M. (2025, August 5). Can laminated glass be tempered? - Hals International Inc. Hals International Inc. https://halsinternational.com/can-laminated-glass-be-tempered/

[3] Glass Doors and Solutions in Muscat. (2025, March 8). Sqtsolution. https://sqtsolutions.com/glass-processing/

[4] Dural, E. (2020). Finite element analysis of laminated glass plates subjected to impact loading. Uluslararası Mühendislik Araştırma ve Geliştirme Dergisi (International Engineering Research and Development Journal), 251–264. https://doi.org/10.29137/umagd.620761

[5] Giovanni, B. (2005, May 1). International Air Transport Association. Annual Report 2005.

[6] Campbell, I. (2001, February 16) Float Glass - Properties and Applications https://www.azom.com/properties.aspx?ArticleID=89

[7] Petrucci, M. (2017, April 14). photo of white and green mountain surrounded by green and brown trees. Unsplash. https://unsplash.com/photos/photo-of-white-and-green-mountain-surrounded-by-green-and-brown-trees-k9DHPwtRb80

[8] Resistive vs. Capacitive Touch Screen: Key Differences. (n.d.). [Capacitive Touch Screen Panel] RF Wireless World. https://www.rfwireless-world.com/terminology/components/resistive-vs-capacitive-touch-screen

[9] “Evafilm”–Sunensys(2020,March13). https://sunensys.com/2020/03/13/eva-film/

[10] Vallabhan, C. V. G., Das, Y. C., Magdi, M., Aşık, M., and Bailey, J. R. (1993). Analysis of laminated glass units. Journal of Structural Engineering,

119(5), 1572–1585. https://doi.org/10.1061/(asce)0733-9445(1993)119:5(1572)

[11] Vallabhan, C. V. G., Aşik, M., and Kandil, K. (1997). Analysis of structural glazing systems. Computers and Structures, 65(2), 231–239. https://doi.org/10.1016/s0045-7949(96)00284-2

[12] Fung, Y.C. (1965) Foundations of Solid Mechanics. Prentice-Hall, Englewood.

[13] Szilard, R. (1974) Theory and Analysis of Plates, Classical and Numerical Methods, Prentice-Hall, Englewood Cliffs, New Jersey.

[14] Timoshenko, S., and Woinowsky-Krieger, S. (1959). Theory of plates and shells (2nd ed.). McGraw-Hill.

[15] Chia, C.Y. (1980). *Nonlinear analysis of Plates*. McGraw-Hill International Book Co.

[16] Reddy, J.N. (2007) Theory and Analysis of Elastic Plates and Shells. 2nd Edition, CRC Press, Boca Raton. https://doi.org/10.1201/9780849384165.

[17] Hooper, J.A. (1973). On the bending of architectural laminated glass. UK Building Research Establishment, CP 36/73.

[18] Vallabhan, C. V. G., and Chou, G. D. (1986). Interactive nonlinear analysis of Insulating Glass Units. *Journal of Structural Engineering*, *112*(6), 1313–1326. https://doi.org/10.1061/(asce)0733-9445(1986)112:6(1313)

[19] Vallabhan, C. V. G. (1983). Iterative analysis of Nonlinear Glass plates. Journal of Structural Engineering, 109(2), 489–502. https://doi.org/10.1061/(asce)0733-9445(1983)109:2(489)

[20] Aşık, M. Z. (2003). Laminated glass plates: revealing of nonlinear behavior. Computers and Structures, 81(28–29), 2659–2671. https://doi.org/10.1016/s0045-7949(03)00325-0

[21] Galuppi, L., and Royer-Carfagni, G. (2012). The effective thickness of laminated glass plates. Journal of Mechanics of Materials and Structures, 7(4), 375–400. https://doi.org/10.2140/jomms.2012.7.375

[22] Knight, J., Salim, H., Elemam, H., and Elbelbisi, A. (2024). Calibration of thermal viscoelastic material models for the dynamic responses of PVB and SG interlayer materials. Polymers, 16(13), 1870. https://doi.org/10.3390/polym16131870

[23] Förch, M. (2020). Time-Temperature dependency of laminated glass subjected to blast load – a numerical study. International Journal of Structural Glass and Advanced Materials Research, 4(1), 69–81. https://doi.org/10.3844/sgamrsp.2020.69.81

[24] Aşık, M. Z., and Tezcan, S. (2005). A mathematical model for the behavior of laminated glass beams. Computers and Structures, 83(21–22), 1742–1753. https://doi.org/10.1016/j.compstruc.2005.02.020

[25] Dural, E., and Vural, S. (2023). Influence of Boundary Conditions on the Behavior of Laminated Glass Curved Beam with Delamination Effect: An Experimental and Numerical Investigation. Heliyon. https://doi.org/10.2139/ssrn.4609027

[26] Dural, E., and Oyar, F. (2022). Effect of delamination size, location and boundary conditions on the behavior of a laminated glass plate. Structures, 47, 121–133. https://doi.org/10.1016/j.istruc.2022.11.034

[27] Dural, E. (2025). An overview of the effect of various interlayer materials and boundary conditions on delaminated glass plates. Advances in Science and Technology – Research Journal, 19(6), 70–83. https://doi.org/10.12913/22998624/202811

[28] Dural, E. (2024). Delamination resistance of laminated glass plates having ethyl vinyl acetate, polyvinyl butyral and Sentryglas Plus interlayers. In V. Gayoso Martínez et al. (Eds.), Mathematical Methods for Engineering Applications (pp. 281–292). Springer. https://doi.org/10.1007/978-3-031-49218-1_20

[29] Dural, E. (2020). Finite element analysis of laminated glass plates subjected to impact loading. Uluslararası Mühendislik Araştırma ve Geliştirme Dergisi, 251–264. https://doi.org/10.29137/umagd.620761

[30] Dural, E. (2021). Effect of temperature on Charpy impact response of laminated glass structures. Physics and Mechanics of Materials, 82(3), 438–454. https://doi.org/10.18149/mpm.4732021_6

[31] Ventsel, E., Krauthammer, T., and Carrera, E. (2002). Thin Plates and Shells: Theory, analysis, and applications. Applied Mechanics Reviews, 55(4), B72–B73. https://doi.org/10.1115/1.1483356

[32] Birman, V. (2011). Plate structures. In Solid mechanics and its applications. https://doi.org/10.1007/978-94-007-1715-2

[33] Langhaar, H. L. (1962). Energy methods in Applied Mechanics. John Wiley and Sons Inc. http://ci.nii.ac.jp/ncid/BA2083782X

[34] Schneider, G. E., and Zedan, M. (1981). A Modified Strongly Implicit Procedure for the Numerical Solution of Field Problems. Numerical Heat Transfer, 4(1), 1–19. https://doi.org/10.1080/01495728108961775

[35] Aşık, M., and Vallabhan, C. V. G. (1997). On the convergence of nonlinear plate solutions. Computers and Structures, 65(2), 225–229. https://doi.org/10.1016/s0045-7949(96)00283-0

[36] Mohareb, M. E. (1990). A mathematical model for the nonlinear analysis of laminated glass plates subjected to lateral press. https://ttu-ir.tdl.org/ttu-ir/bitstream/2346/21015/1/31295005927032.pdf

[37] Dural, E. (2011). Analysis of Laminated Glass Arches and Cylindrical Shells [Middle East Technical University]. https://etd.lib.metu.edu.tr/upload/12612907/index.pdf

APPENDICES

A. Sample Glass Material Properties

Table 5.1 Material properties of float glass [1]

Property	Minimum Value (S.I.)	Maximum Value (S.I.)	Units (S.I.)
Atomic Volume (average)	0.009	0.0095	m_3/kmol
Density	1.9	3.99	Mg/m_3
Energy Content	20	25	MJ/kg
Bulk Modulus	26.1	51.5	GPa
Compressive Strength	212	387	MPa
Ductility	0.00042	0.00048	
Elastic Limit	21.2	38.7	MPa
Endurance Limit	20	36.7	MPa
Fracture Toughness	0.54	0.71	MPa.$m_{1/2}$
Hardness	700	5000	MPa

Loss Coefficient	1.00E-05	0.0001	
Modulus of Rupture	27.5	50	MPa
Poisson's Ratio	0.18	0.25	
Shear Modulus	19.6	34.2	GPa
Tensile Strength	21.2	38.7	MPa
Young's Modulus	47.7	83.6	GPa
Glass Temperature	653	947	K
Maximum Service Temperature	474	727	K
Minimum Service Temperature	0	0	K
Specific Heat	700	910	J/kg.K
Thermal Conductivity	0.75	1.45	W/m.K
Thermal Expansion	1	12	10_{-6}/K
Breakdown Potential	12	14	MV/m
Dielectric Constant	4	15	

Resistivity	1.00E+21	1.00E+25	10^{-8} ohm.m